The Fiber Multi-Object Spectrograph for the Okayama 188cm Telescope

~ Instrument and Observation ~

Kiso observatory, Institute of Astronomy,
School of Science, The University of Tokyo

Hiroyuki Mito

1/January/2000

THIS THESIS IS DEDICATED

TO MY PARENTS.

ABSTRACT

A fiber multi-object spectrograph is an astronomical instrument for simultaneous spectral observations of many stars and galaxies on the focal plane. It enables an astronomer to improve the efficiency of his observations dramatically. In this paper, the improvement of the Okayama Fiber Multi-Object Spectrograph and the observations of the open clusters using this instrument will be presented as a partial fulfillment of the doctral dissertation. The development of the Okayama Fiber Multi-Object Spectrograph started in 1991. The instrument has a wide field of view of 1 degree with thirty optical fiber probes. The diameter of the fiber core is 113 μm which corresponds to 2.5 arcsec at the focal plane. The resolution of the spectrograph is $\lambda/\Delta\lambda = 100 \sim 150$. The observational goal of this instrument is the spectroscopic studies of clusters of galaxies, pre-main-sequence stars in a star forming region, and open clusters which extend over about ten arcminutes or somewhat more in the sky.

In 1993, the author joined the development group in the National Astronomical Observatory of Japan, just after basic functions and operation of the instrument had been completed and the astronomical spectra had been taken in the test observations. However, there was some doubt if the spectra were actually taken at the exact positions, because the signals were much weaker than the expected ones and the observed objects were the emission line stars in the H II region with rather strong and extended continuum and emission lines. Appar-

ently, an accurate control system was needed to perform scientific observations with this instrument. In the first part of this paper, the improvement of the total system will be described.

The instrument is consisted of (1) a fiber positioner, (2) a spectrograph, (3) optical fibers which connect a fiber positioner and a spectrograph, and (4) a computer for controlling the instrument and acquiring the data. The author's first task in the development group was to measure the basic functions of the instrument. A close study of each components revealed three points which should be improved for the efficient observation. Most of the efforts since then was spent to fix these defects.

The first flaw was the poor positional accuracy of fiber probes on the focal plane. The laboratory experiment showed that they were located around the positions of the observed stars with positional errors of $\sigma = 148\mu m$. Since the diameter of the fiber is only $113\mu m$, this large dispersion should have been the main cause of the extremely low throughput. To solve this problem, we took the method of replacing fiber probes till it is located inside the permissible range. An entire conversion of the control system was needed to realize a fine adjustment to relocate the fiber probes. The new positioning system achieved the positional accuracy of $\sigma = 10\mu$m, small enough for the optical fibers.

The second point was concerned with the optical setup inside the instrument; (1) the image of fiber probes on the CCD surface, which was made by the viewing optics, shifted about $140\mu m$ from the image of astronomical object, (2) the focal surface of the image of astronomical objects at the viewing optics differed from that of fiber probes, and (3) the focal surface of the observational fibers differed from the right position. These defects were removed by (1) the correction of offset, (2) the attachment of correcting optics, and (3) the new fiber probes with proper optical design.

Thirdly, the old control system was replaced by the new one which simplifies to handle the instrument and allows to observe astronomical objects more stable.

In the second part of this paper, I will report the observation of open clusters using the improved Okayama Fiber Multi-Object Spectrograph. The abundance gradients of Galaxy has been the subjects of a considerable number of studies over the past decade. Carraro (1998) [1] recently showed the metallicity gradient of -0.09dex/kpc for the open clusters in the Galaxy. At the same time it was noted that the dispersion of cluster metallicities about the mean at any distance was significantly larger than the observational error (Friel and Janes 1993 [5]).

The confirmation of this inhomogeneity is important for the study of the chemical evolution of the Galaxy. We focused on the open clusters younger than 1 Gyr in order to reduce the confusion by the age-metallicity effect. The Friel's(1987) [6] method was adopted to measure the metallicities of stars. Our calibration using the $\lambda/\Delta\lambda = 100 \sim 150$ resolution spectra gave the accuracy of $\sigma = 0.26$ dex.

We observed four open clusters, NGC6709, NGC6866, IC4665, and NGC6633 in April and May 1999. Sixteen reference stars were also observed for the metallicity calibration. We have obtained the [Fe/H] of the clusters as $+0.15 \pm 0.01$ dex for NGC6709, $+0.09 \pm 0.12$ dex for IC4665, -0.36 ± 0.54 dex for NGC6866, and $+0.07 \pm 0.10$ dex for NGC6633. One cluster, NGC6633, was measured previously by Piatti et al.(1998) [16] giving its metallicity of [Fe/H] $= -0.02$ dex. Our result is slightly larger than but consistent with this. Although the small statistics of our sample prevents us from deriving any firm conclusion, our observation has added new information to the cluster metallicities.

Contents

Chapter 1

INTRODUCTION

Observers have always required a sufficient signal-to-noise ratio for their faintest objects. Therefore, a larger telescope has been built to obtain better data with a shorter exposure time. However, the fact is, when a larger telescope was built, an astronomer wanted to observe a fainter object and spent longer exposure time in obtaining the best data. The need to take many spectra at a time naturally lead to the idea of multi-objects spectrograph, one of which was a fiber multi-object spectrograph discussed here.

Recently, many telescopes with a mirror size of 8m or larger have been built in the world. The Okayama 188cm telescope is no longer a large telescope in the world standard and can not compete with the larger ones in the quality of data. However, it can compete in the quantity of data by simultaneous observations. In this respect, the Okayama Fiber Multi-Object Spectrograph should be considered as one of the future observation mode of the Okayama Astrophysical Observatory.

The team of the National Astronomical Observatory Japan started the development of the Okayama Fiber Multi-Object Spectrograph in 1990 [12]. It had two aspects; a prototype of the instrument for larger telescope as SUBARU and the scientific instrument for the Okayama 188cm telescope. The author joined

the project team in 1993 when the first test observation succeeded in obtaining an astronomical signal from emission line stars in the Orion nebula. However, the observation also revealed serious problems about the instrument. The most serious one was that the signal was extremely weak. Subsequent laboratory test confirmed that the spectrograph and the CCD camera worked properly and that the weakness of light power emitted from a fiber was the cause of the low signal. The other problem was a very complex procedures before and during the observation. In practice, this reduced the observational efficiency very much. In chapter 2, the details of the wrong points about the Okayama Fiber Multi-Object Spectrograph will be discussed. The results of the improvements will be given in chapter 3.

The Okayama Fiber Multi-Object Spectrograph has thirty fibers on the focal plate whose field of view is 1 degree. The Jobin-Yvon CP200 spectrograph is used whose dispersion is $\lambda/\Delta\lambda = 100 \sim 150$. The most suitable targets for the Okayama Fiber Multi-Object Spectrograph are, therefore, some tens of bright objects scattered within a few tens of arcminutes. As the first observation of the Okayama Fiber Multi-Object Spectrograph, we have observed open clusters to obtain their metallicities, [Fe/H]. There are many bright stars (mv= 8-11) in the cluster whose sky subtraction is less difficult than fainter objects. Moreover, following Friel's(1987) [6] method which uses metallicity indices it is possible to measure the metallicities from low dispersion spectra. In chapter 4, the observation of the open clusters will be described and its result will be discussed in chapter 5.

Chapter 2

IMPROVEMENT OF THE INSTRUMENT

2.1 Motivations

2.1.1 Outline of the Instrument

a) Focal Environment Assembly

Figure 2.1 shows the layout of the instrument. It was attached to a Newton focus of the telescope. There are fiber probes receiving the light of astronomical objects on the focal plane. Optical fibers lead the light to the spectrograph at the bottom of the telescope, whose field of view is ϕ 1 degree, 16cm in size.

Figure 2.2 shows the environment of the focal plate. Mechanical design based on *Autofib* built for the Anglo-Australian Telescope(AAT) (Parry et al. 1986 [13]). The bottom of the probes is put a permanent magnet ($SmCo_5$). The probes are carried by electromagnetic manipulator unit and placed on the focal plane of steel. The manipulator unit is mounted on the X-Y stage which is composed of the base plate, two ball screw/slides units with motors (for X and Y each), its

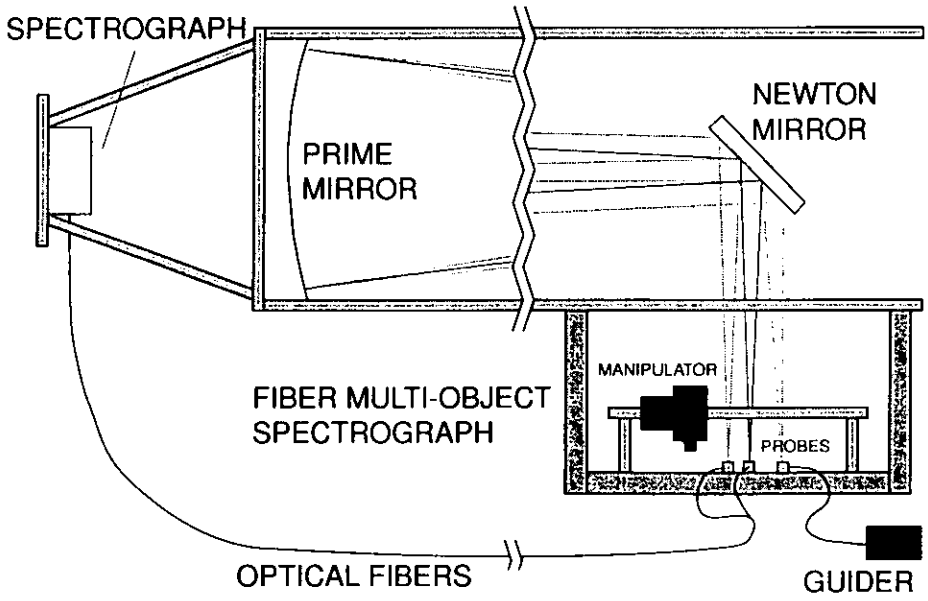

Figure 2.1: The layout of the instrument

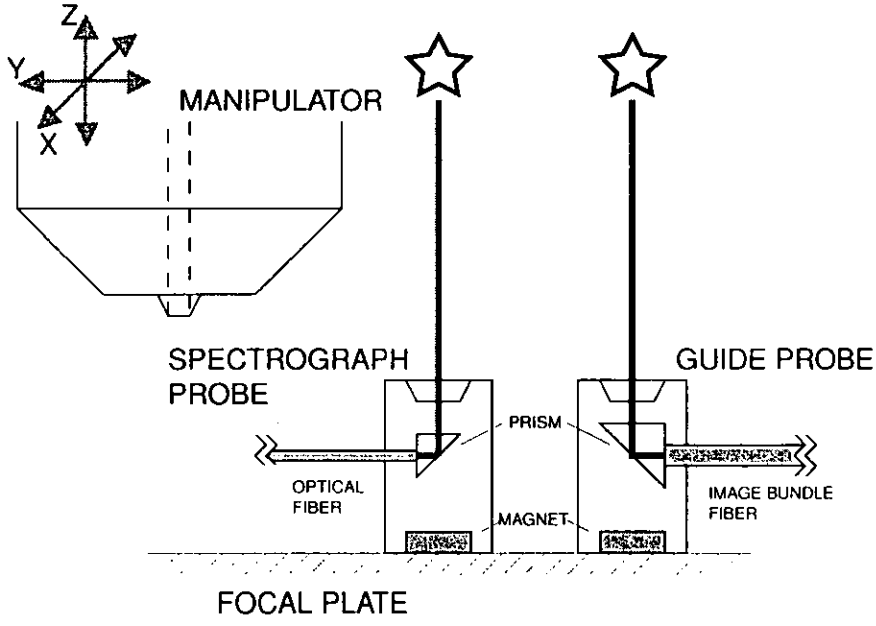

Figure 2.2: The environment of the focal plate

drivers/controllers and linear scale encoder. The manipulator unit can move in Z direction, too. The telescope is guided by watching stellar images obtained through three image bundle fibers on a focal plate. These probes are basically of the same design as single fibers for objects. Each image bundle has a 1.9mm aperture, an field of view of 43 arcsec. The image bundle feeds the light to an intensified CCD camera. Moreover, these image probes are used to determine instrument focus.

The viewing optics is located on the pickup head on the X-Y stage and can be positioned above any fiber on the field plate. The system allows a back-illuminated fiber and the astronomical object to be seen simultaneously. The optical arrangement is shown in Figure 2.3. Original design of this system is by Parry(1990) [14] for the William Herschel Telescope. We did not use a beam splitter of pellicle but optical glass, because we thought that pellicle beam splitter would vibrate and the images would not be stable. A corner cube prism was used instead of a mirror so that the image of the sky and the fiber moved together when the viewing optics were moved. Thus it was possible to check that a fiber was correctly placed on the object irrespective of the position of the viewing head so long as they were in the field of view.

Another viewing optics, the medium-field camera, is added to the instrument. This optics is composed of a non-cooled CCD camera and a folding mirror, and is mounted on the linear slide which moves to see the center of the field of view in use. The field of view of the camera is 3 arcmin $\times$ 2.3 arcmin. After mounting the instrument on the telescope, this camera is used to calibrate the telescope position indicated on the console to the center of the field of view of the instrument.

All the components of instrument, except the CCD camera detecting spectra, were operated by two personal computers: one operated the viewing optics, the other did the rest of task and took charge of the user interface. The software of

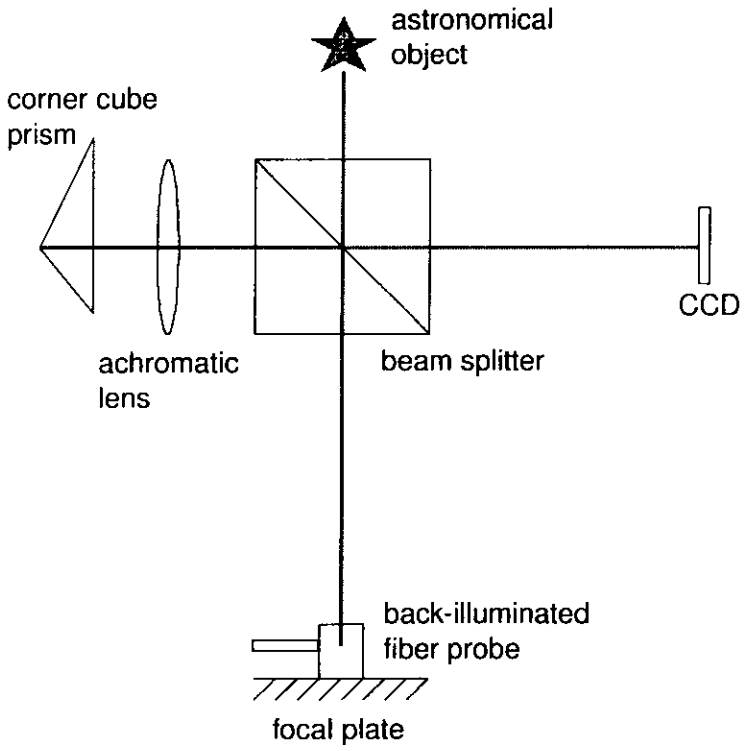

Figure 2.3: The layout of the viewing optics

the former was developed and that of the latter was a ready-made. The operating system of the both personal computers was MS-DOS. The commands to operate the instrument were input by command-line.

b) Spectrograph

The Cassegrain (f/18) spectrograph of Okayama Astrophysical Observatory was used in the first observation. Since the F ratio of the Newton focus is 4.9 and the input F ratio of the spectrograph is 18, focal extender was used which convert light beam of f/4.7 to that slower than f/18. However the throughput of the spectrograph was low. The main cause of the light loss was thought to be a structure of the spectrograph whose optics from the slit to the collimator lens is

the inverse Newtonian configuration, and the light beam on the primary axis is cut off by Newtonian mirror mounted on the axis. Since it is generally known that the output beam from an optical fiber has maximum intensity in the center part, this structure of the spectrograph was thought to be fatal. Therefore, in 1993 the spectrograph was exchanged for CP200 which was produced by Jobin Yvon. Figure 2.4 shows the schema of the spectrograph. This spectrograph includes concave grating and does not obstruct the central portion of the incident rays. Moreover, since the concave grating by itself replaces the collimating optics, the number of optical surface is kept to a minimum, resulting the high reflection efficiencies.

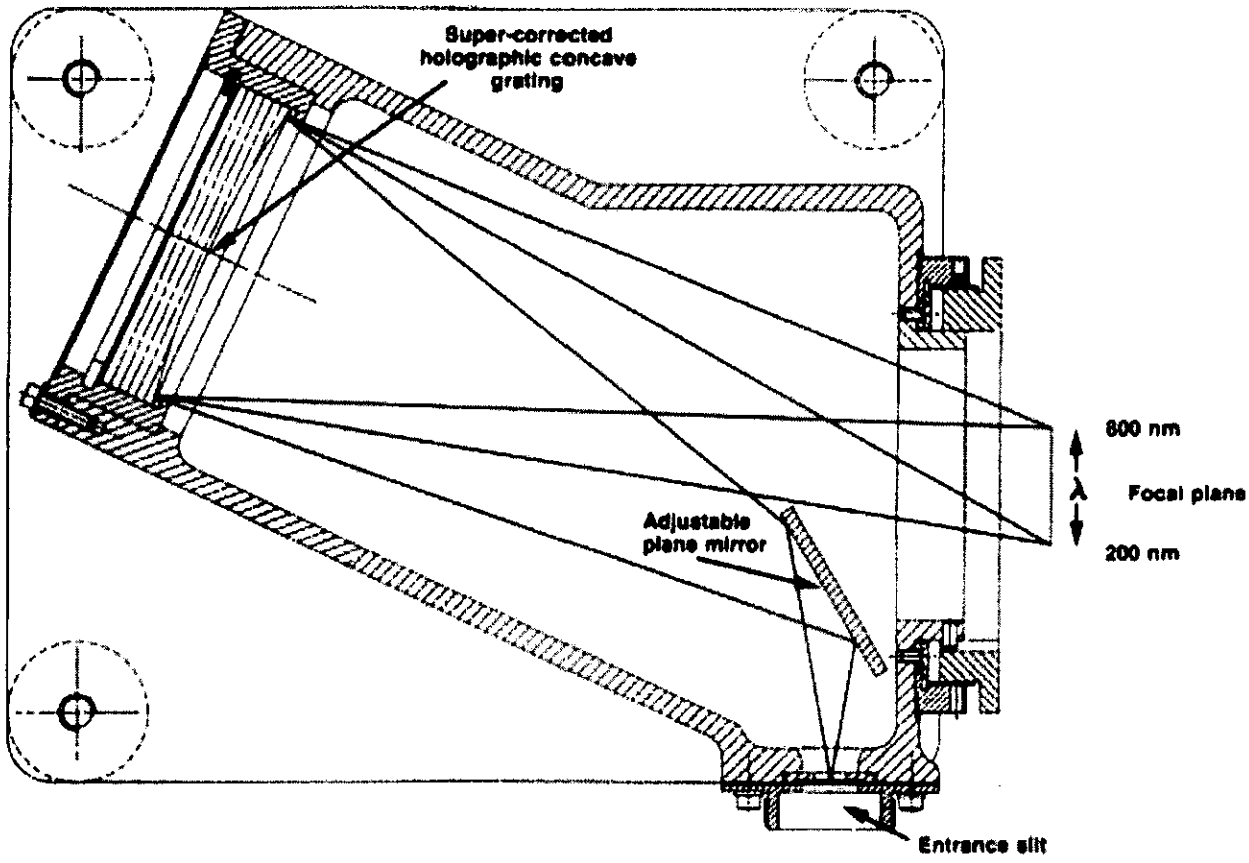

Figure 2.4: The schema of the spectrograph Jobin-Yvon CP200

specifications	
field of view:	1 degree
number of fibers:	30
observational efficiency:	5 fields/night 150 objects/night
resolution of spectrograph:	R= 100 $\sim$ 150 JobinYvon CP200
throughput:	mv= 10, S/N 100, 0.6 minutes These values are comparable to that of Okayama Cassegrain spectrograph.
diameter of fiber core:	ϕ 2.5 arcsec 113 μm
CCD:	1024 $\times$ 1048 Texas Instrument TC215
range of spectra:	400nm

Table 2.1: specifications of the instrument

c) Specifications

Table 2.1 shows specifications of the instrument. We aimed to observe clusters of galaxies, open clusters, globular clusters, and young stellar objects in a star forming region. Moreover, it was important purpose to get professional knowledge for fiber multi-object spectrograph through development of the instrument.

d) Particular Problems of a Fiber Multi-Object Spectrograph

A fiber multi-object spectrograph has particular problems, such as image scrambling, focal-ratio degradation (FRD), and sky subtraction. Image scrambling is the phenomenon that the radial distribution of emerging light at the output end of a fiber is changed by the position of the stellar image at the input end. This is remarkable in case the f-ratio of light at the input end is fast. FRD is the phenomenon that the f-ratio of light at the output end becomes faster than that of the input end. FRD is a serious problem for the slow input beams (>F/6). This makes design of spectrograph difficult. It is difficult to subtract sky components precisely from object. This is because throughput character of fiber is different each other. In case of Okayama Fiber Multi-Object Spectrograph, the FRD is not remarkable, due to a rather fast f-ratio of F/4.9 at the Newton focus. Moreover, as low dispersion spectrograph is used the image scrambling is not a problem. Also, the difficulty of sky subtraction was soften by observing bright objects (mv= 10-12).

	1994	**goal**
basic functions and operations	OK	
positional accuracy	$\sim 170\mu$m	15μm
throughput	30 min., S/N 3 about galaxy($V_T = 11$)	0.6 min., S/N 100 about star(mv= 10)
fiber placement speed /field /30 fibers	4 hours	1.5 hours
adjustment of fiber position	only design	
number of observed stars /a night ($\sim$ 8 hours)	60	150

Table 2.2: the status in 1994

2.1.2 Instrumental Status in 1994

Table 2.2 shows the status of the instrument in 1994. Basic mechanical functions and operations, such as the manipulator is picking up a fiber probe at the home position and putting it to the destination, were achieved by that time. The positional accuracy of 15 μm was required for the fiber probes to match the size of the fiber core 113 μm. Although we measured the positional accuracy by the experiment later, the actual achievment was approximately 170 μm. We shall return to this point later.

We observed clusters of galaxies, Pegasus I, Hercules, and a few field stars with new spectrograph CP200 in August 1994 and aimed to obtain emission lines in the spectra. In fact, we had suspected whether the manipulator arranged fibers precisely. Therefore we observed diffused objects. However, the light power from

fibers was still low, although we hoped that the new spectrograph increased it.

Figure 2.5 shows the flow diagram of fiber probe arrangement. The manipulator arranges one fiber probe through this sequence, which is repeated as many times as the number of probes that should be done.

Constitution of the instrument appears in Figure 2.6. The detector of the viewing optics was the commercial CCD camera, ST4(SBIG), and a ready-made software was used to operate the CCD camera. As a result, all the parts of instrument except CCD camera detecting spectra were operated by two personal computers: one operated the viewing optics, the other did the rest of task and took charge of user interface. Since the two computers were separated each other, in the case of correcting probe position, we had feed back manually the positional information from the viewing optics into positioner.

The CCD camera was operated by personal computer via RS232C whose communication speed was 9600 bps. It spent about $30 \sim 40$ seconds in measuring an object or a fiber probe position except for time to integrate photons from them and to measure position manually. There were two exposures by the viewing optics in the sequence of a fiber probe arrangement. However, in case that object image was not confirmed on a monitor, more and longer exposures were required. As the result, we spent about four hours in arranging thirty fiber probes, although we did not correct the fiber probe positions. In other words, we could observe only sixty objects per night ($\sim$ 8 hours) by the instrument.

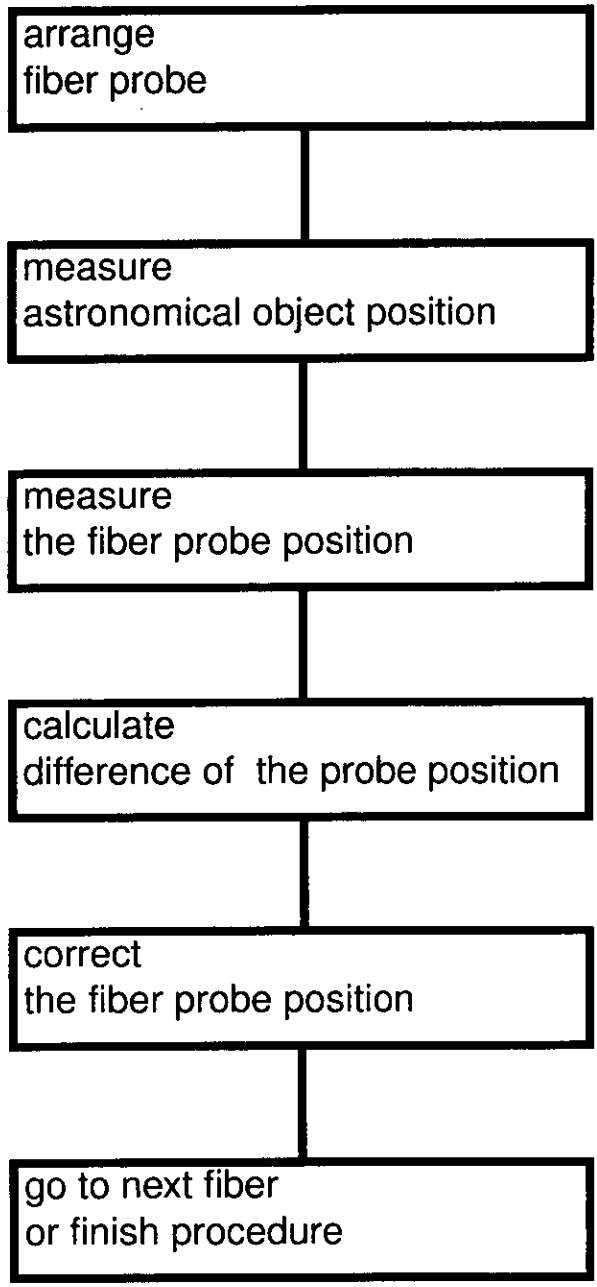

Figure 2.5: flow diagram of fiber arrangement procedure in 1994

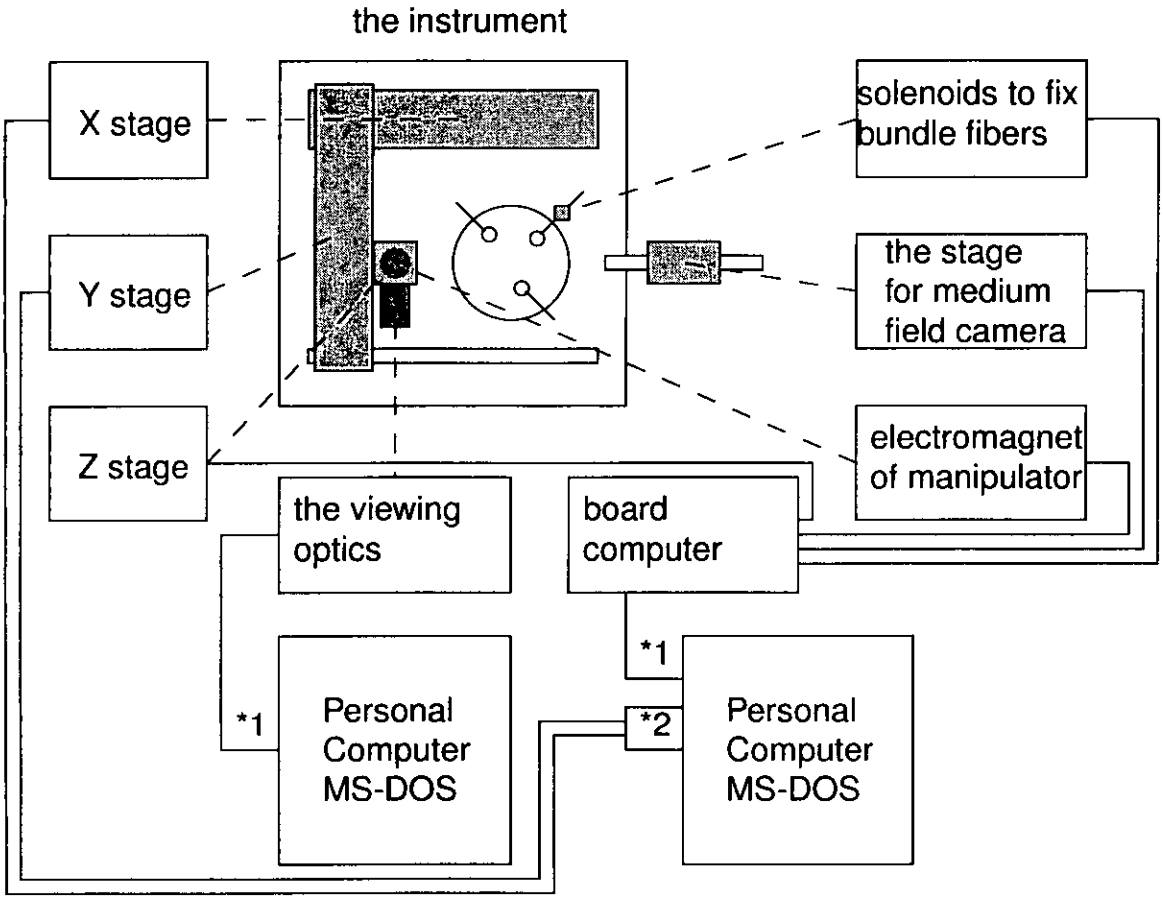

Figure 2.6: operating system of the instrument in 1994 (*1 RS232C, *2 stage controller board)

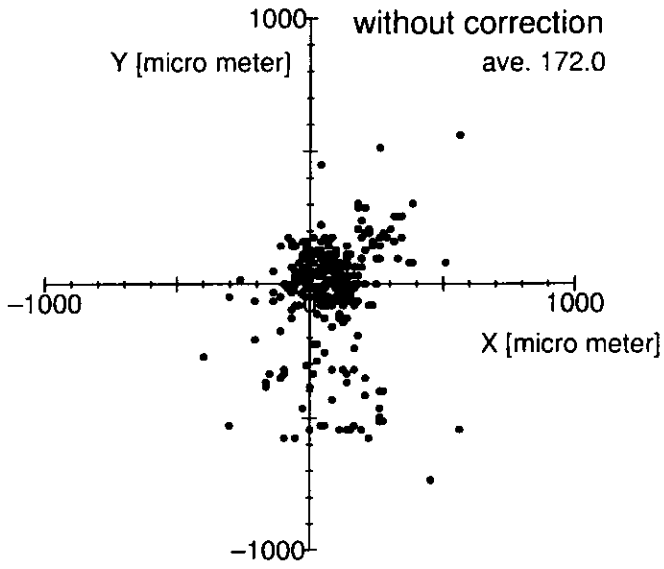

Figure 2.7: fiber probe positions by the previous method (Central circle shows the diameter of fiber core 113 μm.)

2.2 Improvement after 1994

2.2.1 Allocation of Fiber Probes

a) Context

Previously, we observed the diffuse objects, such as galaxies, as we have mentioned before, because we noticed that the positioning errors of the probes was not sufficient. However, we still obtained a poor signal-to-noise ratio.

Figure 2.7 shows the result of experiment investigating positioning errors of the probes. We estimated that the average error was 172.0μm. The two phenomena caused the error, when the manipulator left the probe. One is shown at Figure 2.8. When the probe is set out of the radial direction, it was twisted by the tortion of the fiber. As the tortion is released after the manipulator leaves, the position of the probe changes. The other is shown at Figure 2.9. When the ma-

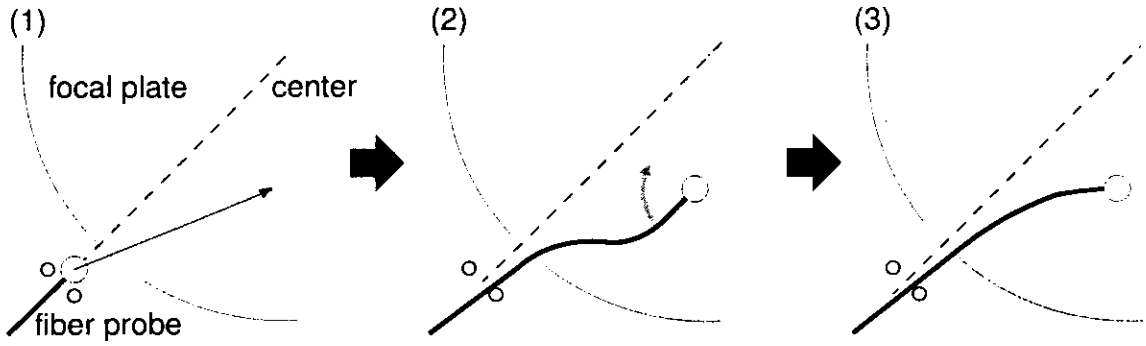

Figure 2.8: releasing tension of the fiber probe

nipulator leaves the probe, the electromagnet is turned off, however, magnetism does not vanish instantly. As the result, the probe is lifted slightly and changes the position.

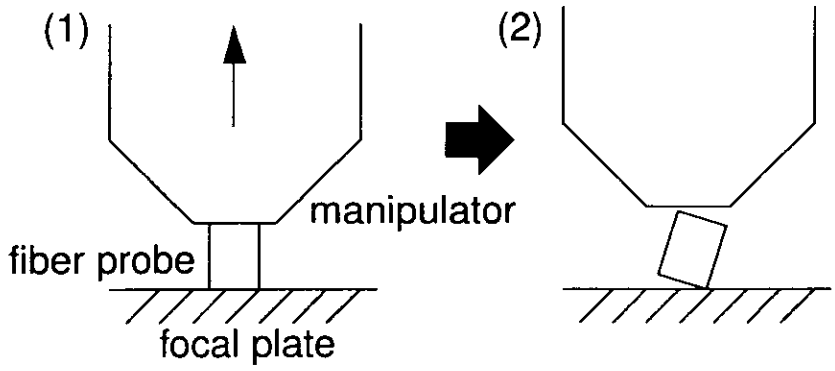

Figure 2.9: residual magnetization of the manipulator

b) Improvement

We improved the instrument so as to reduce the positioning error. We changed the method for arrangement of the probes. Figure 2.10 shows the flow diagram for this method. The viewing optics measure the position of the probe, after the manipulator leaves the one. If the positional error of the probe is unacceptable, the manipulator repeat the same procedure. This process will be iterated till the error is sufficiently small.

Moreover, we reconstructed the system of instrument to process the repositioning of the probes automatically. Figure 2.11 shows the new system. Previously, the computer operating the viewing optics was isolated from the total system. Therefore, it was impossible to feed back automatically the positional informations of the viewing optics to the computer operating the manipulator. However, in the case of new system, as single computer operates all parts of the instrument including the viewing optics, the repositioning of the probes is processed automatically.

Figure 2.12 shows the result of the repositioning of the probes. The positioning error was drastically reduced from $172.0\mu m$ to $20.7\mu m$ on the average.

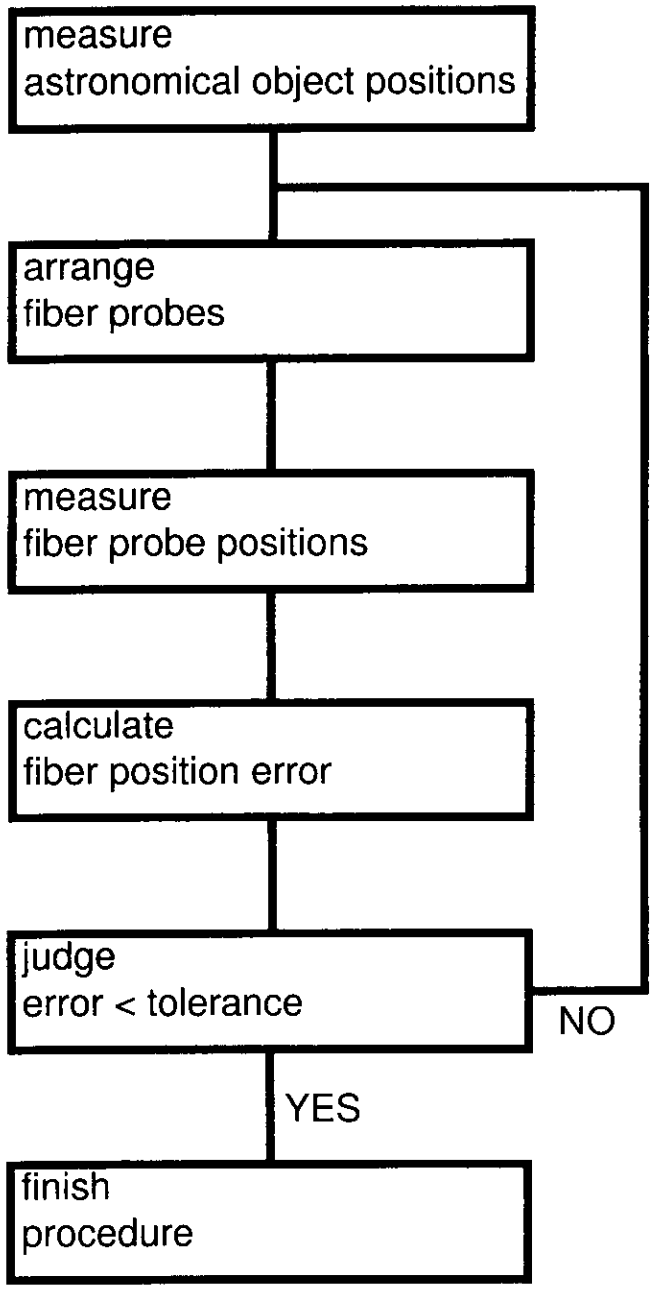

Figure 2.10: flow diagram showing fiber arrangement procedure

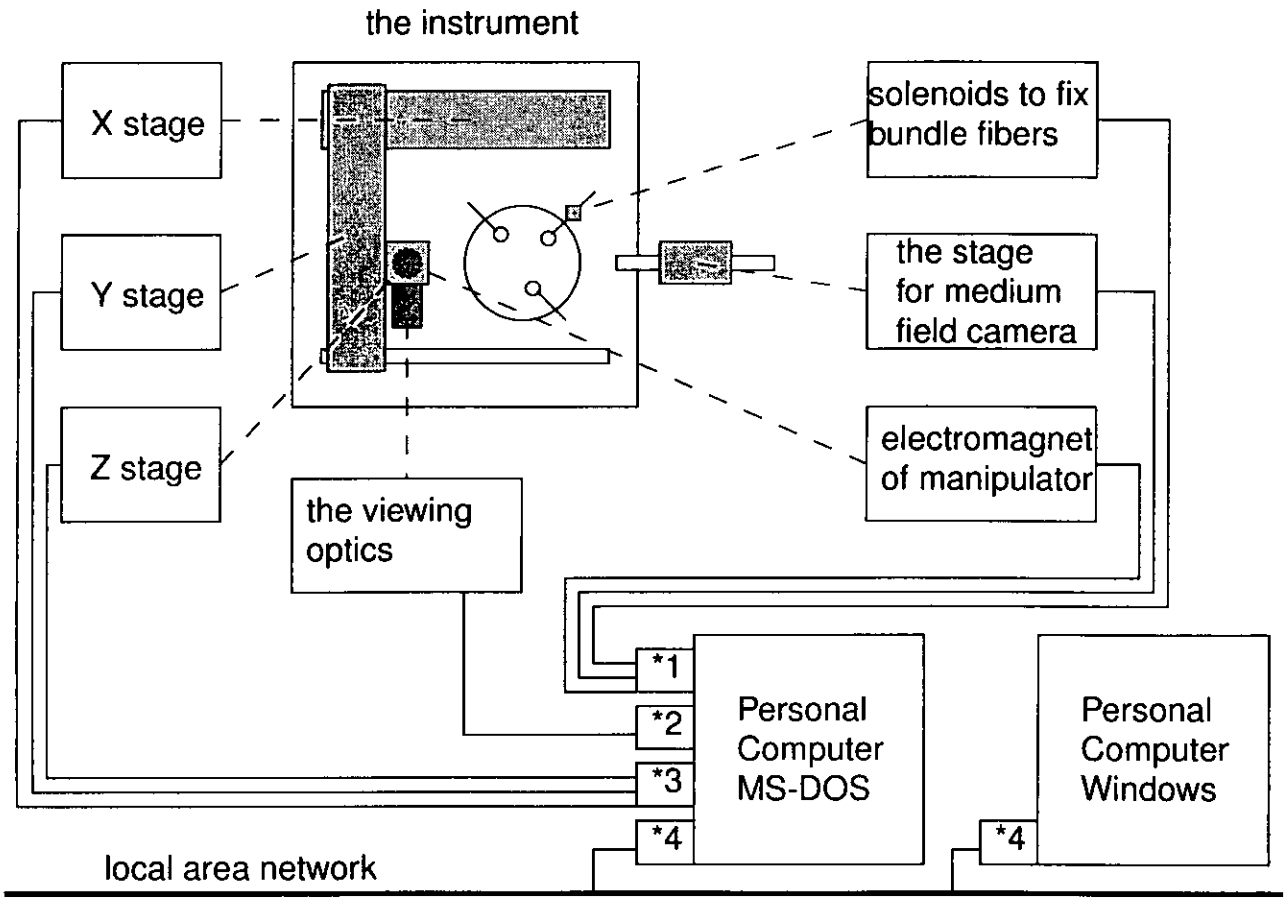

Figure 2.11: new operating system of the instrument (*1 parallel I/O board, *2 RS232C board, *3 stage controller board, *4 Ethernet adapter)

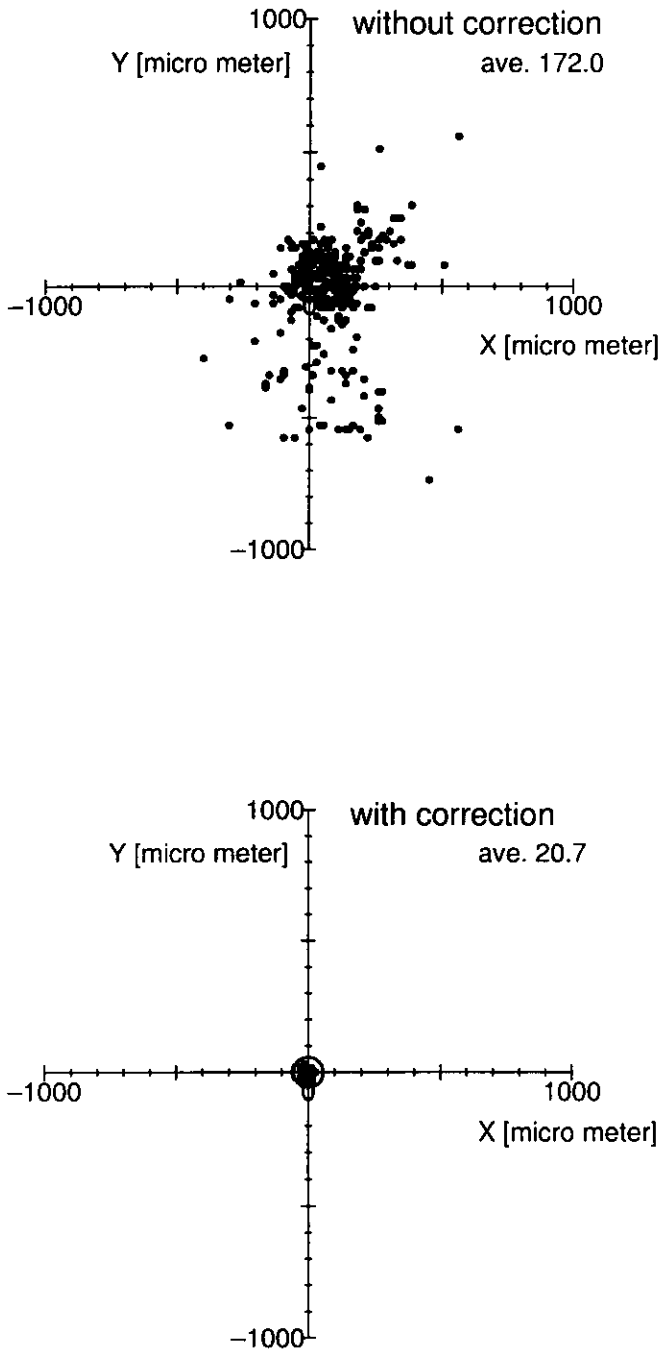

Figure 2.12: fiber probe positions by new method

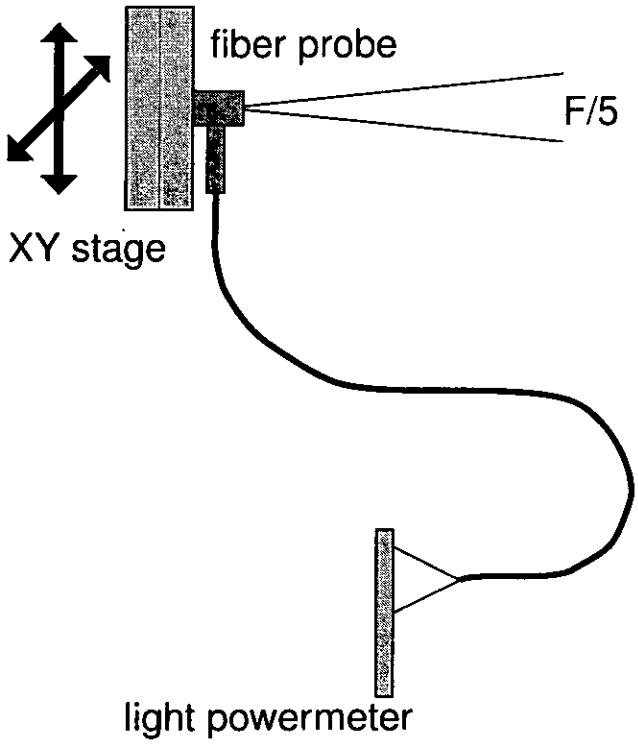

Figure 2.13: schema of the experiment to estimate increment of the throughput

We estimated the increment of throughput by the laboratory experiment. Figure 2.13 shows the schema of the experiment. We projected the converging light with a focal ratio of F/5 and spot size of $100\mu m$ onto the fiber probe fixed on the X-Y stage. We measured the power of light emerging out of the opposite end of the fiber as we moved it on the X-Y stage. Figure 2.14 shows the result. We see from the figure that the throughput increased from 3% for the previous error to 97% for the present error of that for the exact position.

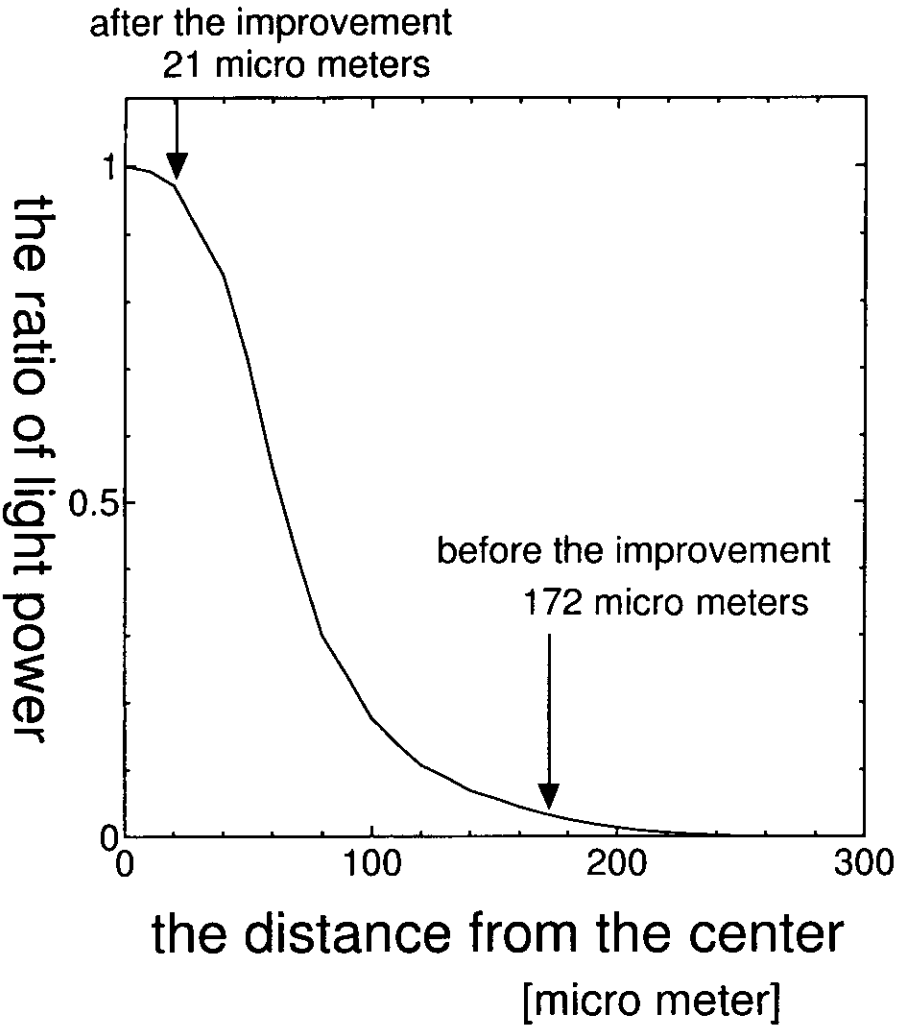

Figure 2.14: We estimated the increment of the light power by the positioning correction. It increased from 3% to 97% relative to maximum value at the exact position.

2.2.2 Optics

a) Adjustment of Focusing Position of the Viewing Optics

Figure 2.15 shows that astronomical object is focused on the fiber probe. The viewing optics is inserted into the path of the light. Figure 2.16 shows the previous design of the viewing optics. It focused the object on different surface from fiber probes. The light from a star ("A" point in the figure) reflects on the beam splitter (B) and is focused on the surface (C). While, the light from the probe (a) reflects on the beam splitter (b), is collimated by the lens (c), reflects on the corner cube prism (d), is converged by the lens (e), passes through the beam splitter (f), and is focused on the surface (g). We see from the figure that the distane of a-b equals to that of f-g, however, the distane of B-C is longer than that of f-g.

Figure 2.17 shows that corrected viewing optics makes the both imaging positions uniform. The central parts of the light from telescope is vignetted by the Newton sub mirror. Since the mirror was attached slantingly, the focal ratio of vignetted light is calculated F/15.3 $\sim$ F/21.6. *i.e.* the light of slower focal ratio than F/21.6 does not incident into the beam splitter. While, the focal ratio of the light from probe is F/25.6, which is determined by diameter of hole of pick-up head. In this circumstances, cylindrical bar optics are attached to the beam splitter to extend the only focal length of the light from probes.

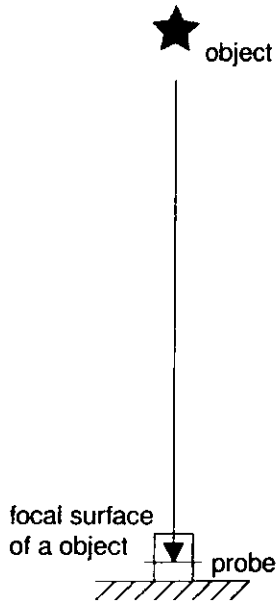

Figure 2.15: An astronomical object is focused on the fiber probe.

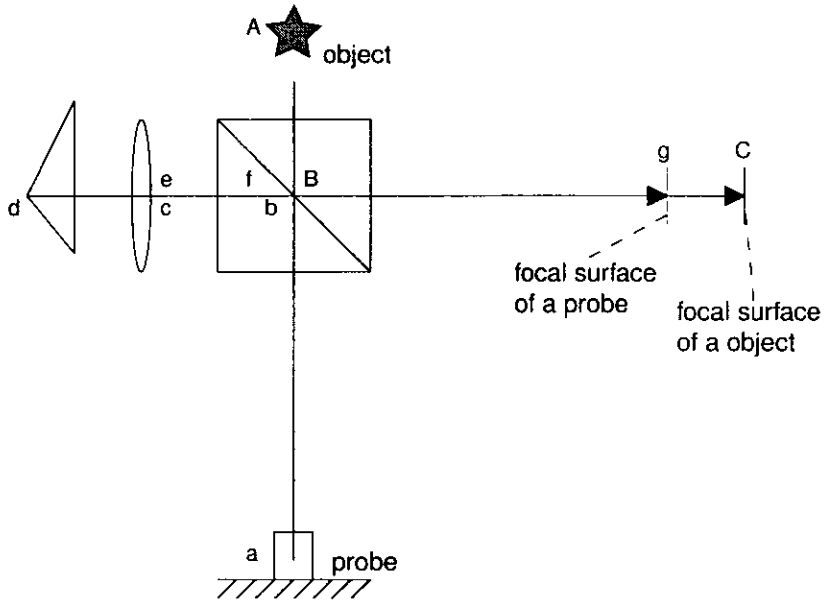

Figure 2.16: Previously, the astronomical object is focused on a different surface from fiber probes by the viewing optics.

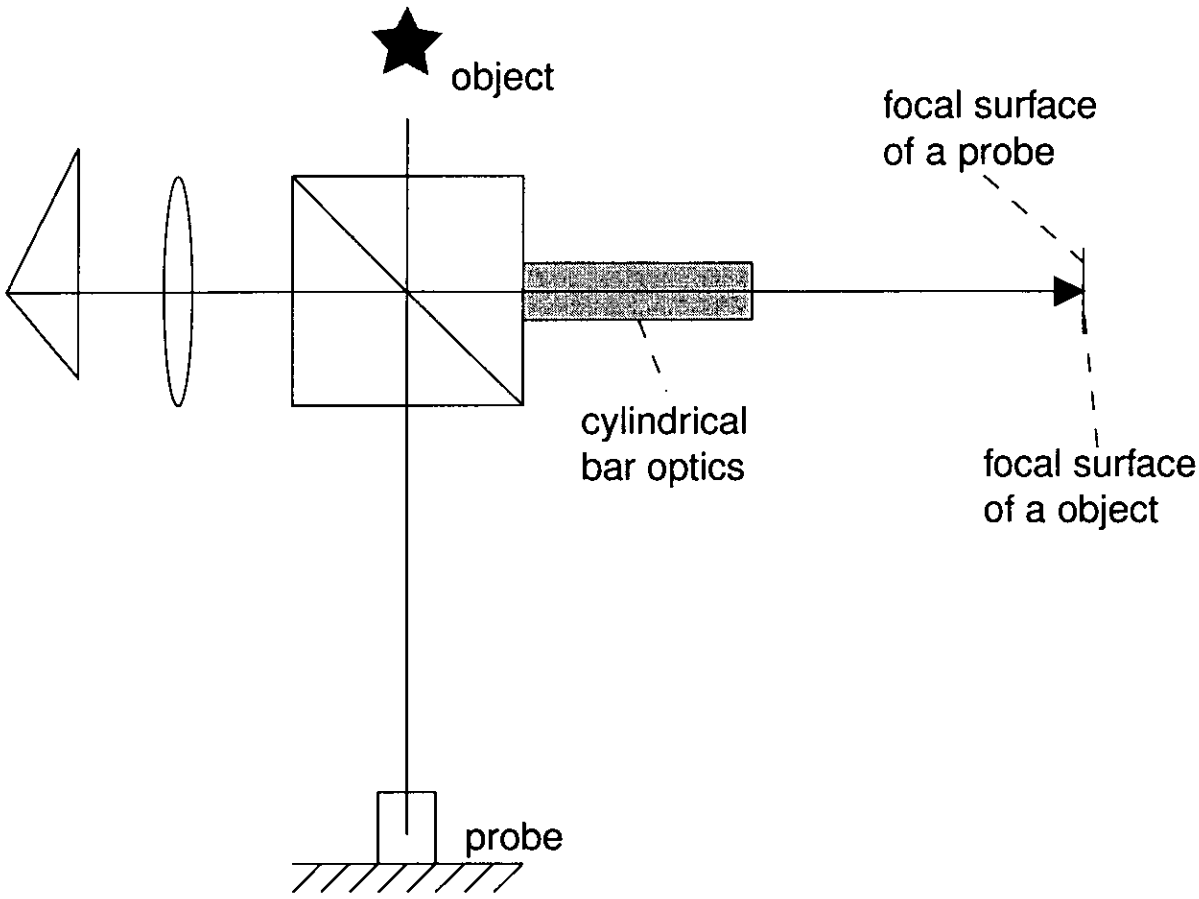

Figure 2.17: We added cylindrical bar optics to the viewing optics.

b) Positional Measurement by the Viewing Optics

The beam splitter is made of two right-angle prisms whose bonding surface is alminaized. We examined whether the beam splitter surfaces facing each other were parallel or not. If the light passes through the beam splitter after reflecting by corner cube prism and the surfaces are not parallel, the light axis from probe will be bended. Figure 2.18 shows schema of the experiment. The collimated light is shaded by the board with two holes, one passes through the beam splitter, the other goes through the air. And the both lights are focused by the lens. If the surfaces facing each other of beam splitter are not parallel, then the each light images on the different position. Figure 2.19 shows the result of this experiment. We confirmed that the difference of the two spots was approximately $100\mu m$ and the surfaces facing each other of beam splitter are not parallel. Previously, fiber probes were located on the position where the both lights from telescope and probe image on the same position on CCD, ST4. This means that the probes were located on different position from the object image.

The surface of the beam splitter should be made parallel in order to solve this problem, however this work is very difficult. Therefore, we measured the offset of the both images and arranged the fiber probe to the position where the offset is added to.

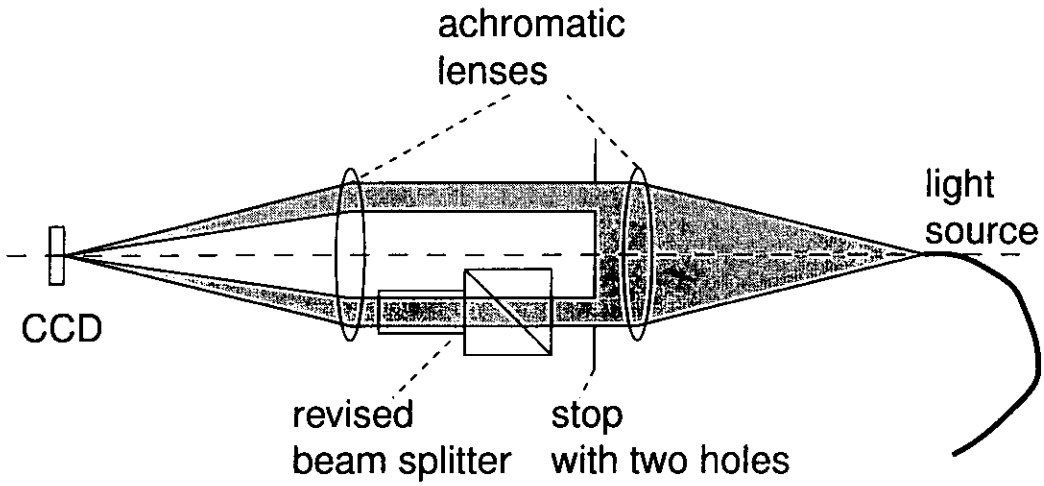

Figure 2.18: We tested if surfaces of the beam splitter involved the viewing optics were parallel.

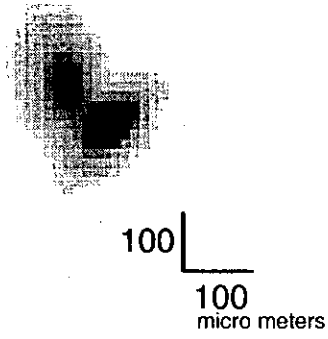

Figure 2.19: result of the parallel test

c) Adjustment of Focusing Position of the Spectral Fiber Probes

There are two kinds of fiber probes on the focal surface plate of the instrument. Thirty probes are to observe objects, three probes are to observe guide star (in this section, henceforth we will call the formers as single and the latter as bundle). Determining the single's focal position means determining instrumental focus. In determining this instrumental focus, the single cannot be used because of the character, but the bundle can be used. Therefore the focal position of the bundle must correspond with that of the single, and determining the bundle's focus position result in determining single's focus position. We researched the both probe designs in detail and knew that the focal position of the single was different from that of bundle.

Firstly, the previous probe designs were analyzed by ray-trace simulation software, "codev". To compare with practical experiment later, we simulated by using optical elements below. We used the achromatic lens with focal length of 200mm, diameter of 40 mm, and focal ratio of F/5.0. The focal ratio was approximated to that of practical telescope, F/4.9.

Figure 2.20 illustrates the schema of ray-trace simulation. Incident ray directed from left to right. A rectangle of right side means the 45° right angle prism. To simplify the simulation, we replaced the 45° right angle prism with optical flat substrates. Optical fiber is attached to the right surface of the optical flat substrates. Left surface of the optical flat substrates is put at 150 cm right side from the lens. Right surface is determined position where the incident ray converges. The result of the ray-trace simulation, length of the optical flat substrates was determined 66.55 mm. Since practical size of the prism in the bundle probes is 3.2 mm, the scale factor is estimated at 20.8.

We researched spot size of the incident light. Figure 2.21 illustrates the schema

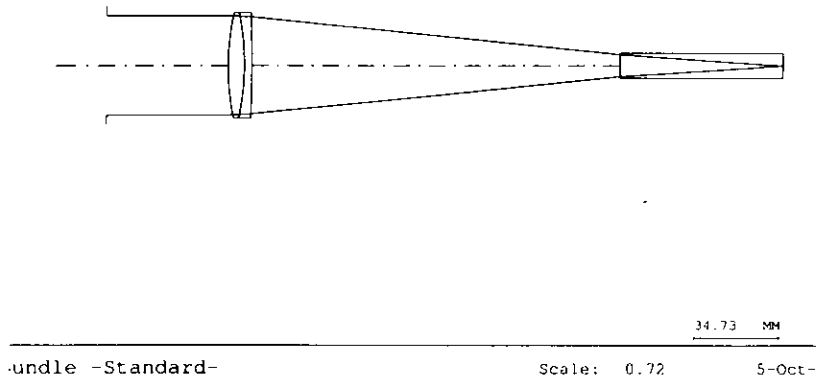

Figure 2.20: Schema of the ray-trace experiment. The rectangle of right side is optical flat substrates, which acts for the 45° right angle prism.

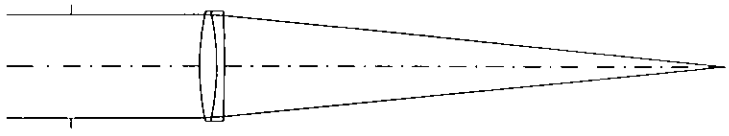

Figure 2.21: We researched spot size of the incident light.

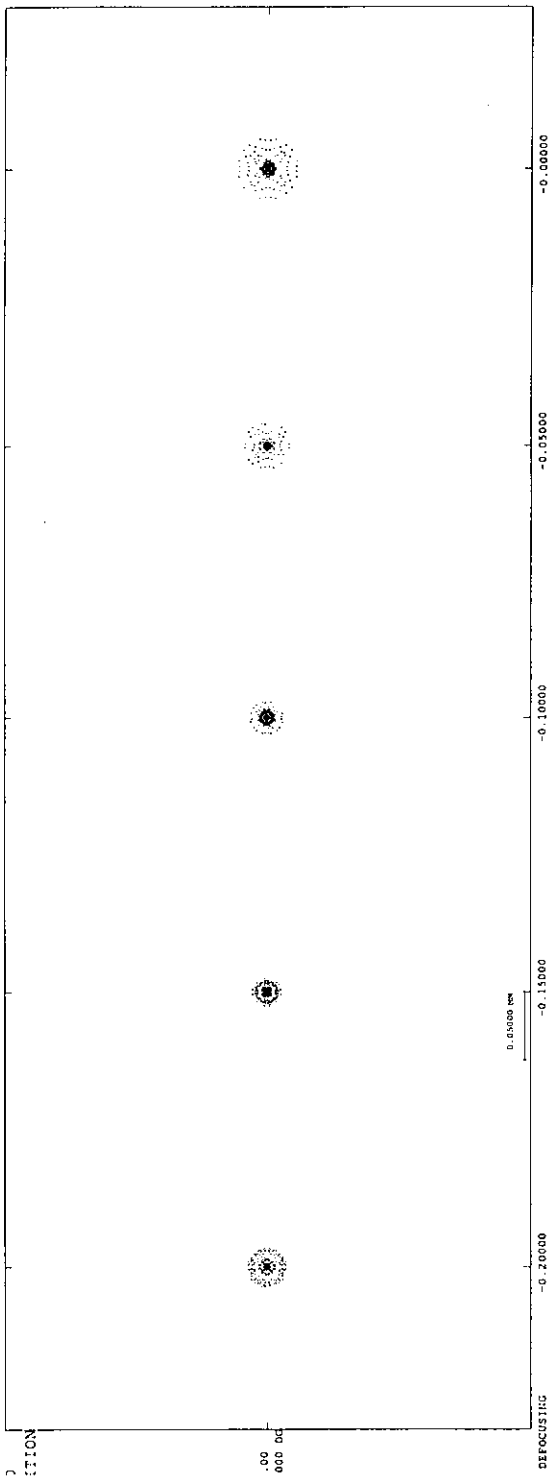

Figure 2.22: Spot diagrams of the incident light.

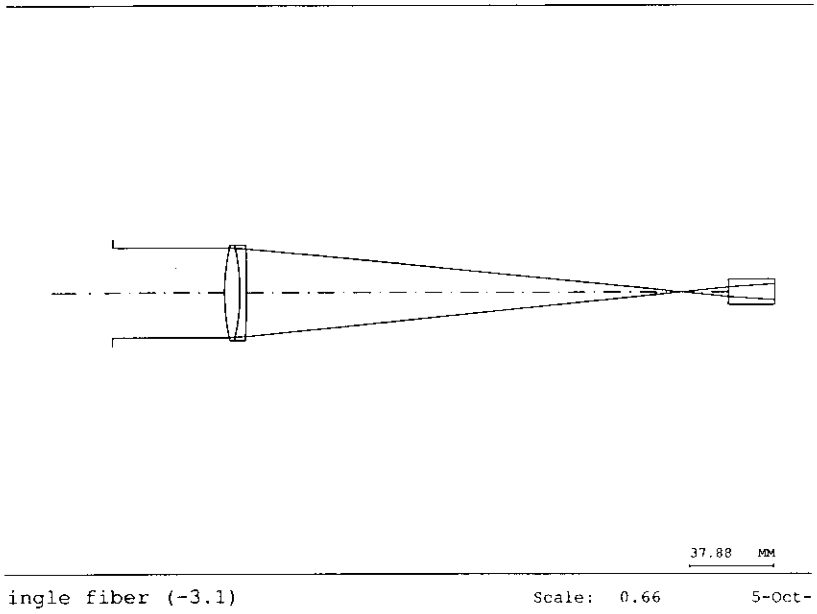

Figure 2.23: We set the prism of the single, following the design of the single probe.

for this. Figure 2.22 is spot diagrams near the focus position. We know that best focus is the second from the top, whose radius is 0.0131 mm (root-mean-square). In the practical case, this value corresponds to the diameter of 1.26 μ m, or 0.0284 arcsec at Newton focal plane of the Okayama 188 cm telescope. This is sufficiently small relative to the typical seeing size of 2.5 arcsec. Therefore, when we will change the measuring position along the light axis, the energy distribution of the image will sensitively change relative to the practical state.

We exchanged the prism of bundle in Figure 2.20 into the prism of single. Figure 2.23 shows this condition. In the practical case, the last surface of the prism (optical flat substrates in the figure) of single is laid at backward position with 3.1 mm relative to the last surface of the prism of bundle. Following this design, we set the prism of the single at the corresponding position. As the figure

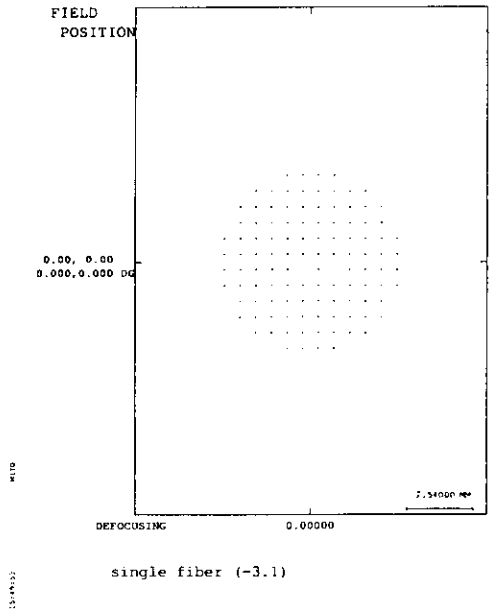

Figure 2.24: spot diagram of previous single

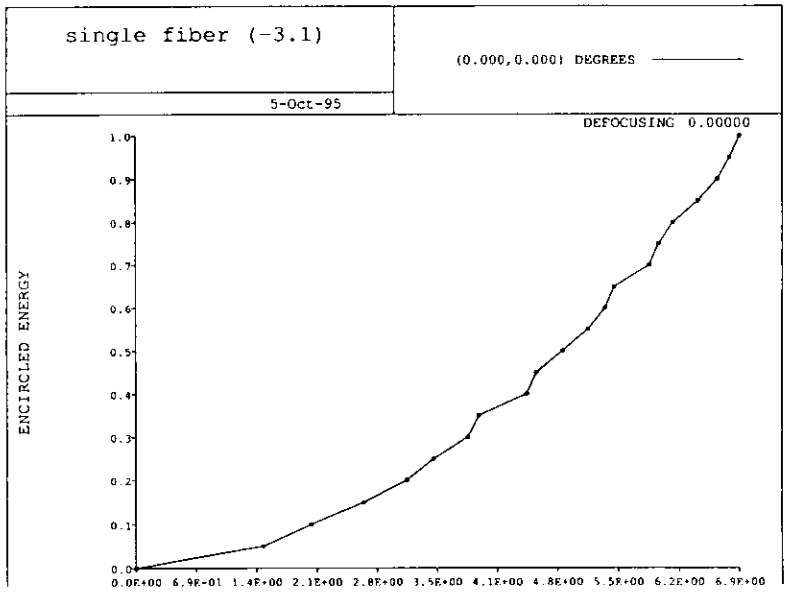

Figure 2.25: energy distribution of previous singles probe

indicates, the focus is obviously out. Figure 2.24 shows the spot diagram of this experiment. We know that the single catches the light of about 13% relative to total light from Figure 2.25.

Secondly, we performed practical experiment. Figure 2.26 illustrates the schema of the experiments. The above figure shows that incident light directs to single and bundle probes. A rectangle at the most right side is a translation stage with a steel plate. The probes is attached to the steel plate. We can flexibly change the position of the probes by moving the translation stage. It is possible for the steel plate to move slightly to teo the other directions. Light source is an optical fiber with 80 μm diameter core and 125 μm diameter clad. Spot image of incident light is shown in the Figure 2.27. The size of the spot at best focus is three or four pixels on CCD (ST4). This size corresponds with about 60 μm or 1.3 arcsec at Newton focus surface of the Okayama 188 cm telescope. This is sufficiently small relative to typical seeing size of the telescope, 2.5 arcsec. Therefore, when we will change the measuring position along the light axis, the energy distribution of the image will sensitively change relative to the practical state. The below figure shows the state of detector side.

We attached the bundle to the steel plate of the translation stage. Figure 2.28 indicates the images of the probes on a detector, when we change the position of the probes by moving the translation stage. The unit of the position is *mm*. The above series show the images of the bundle. Since the bundle is a image bundle fiber, we can directly see the image of incident light on the other end of the bundle. Therefore we can determine focal position from peak intensity of the images on the detector. We defined the position at which the intensity of the bundle image was the strongest as the origin of the translation stage, 0.0 mm.

The below series show the images of the single. Since the single are not a image bundle fiber, we can not directly see an incident spot image on the other end of the single. Thus we estimated focusing conditions from total intensities of the images on the detector. We fixed the two axes perpendicular to the light axis on the position at which the intensity at 0.0 was the strongest. The figure

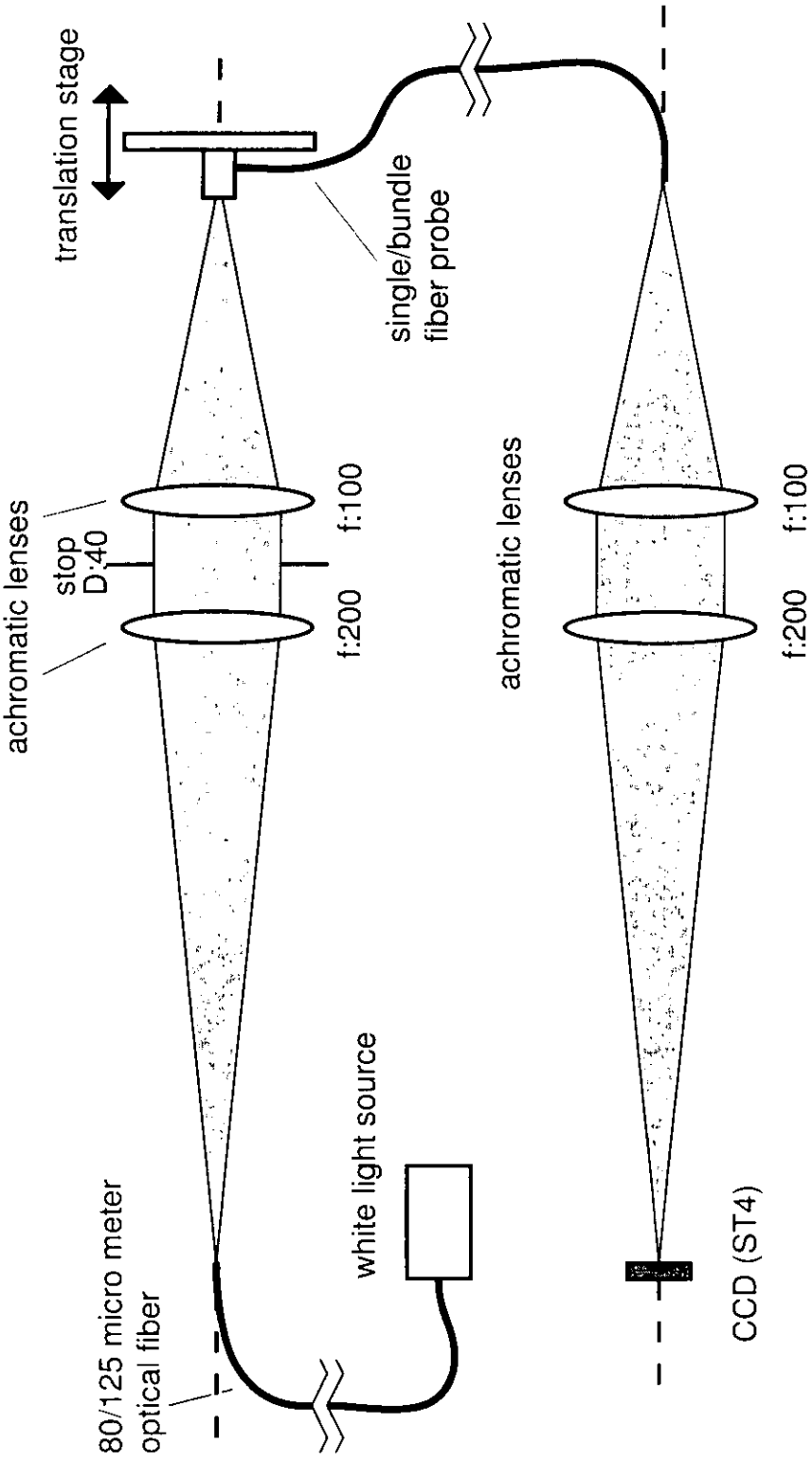

Figure 2.26: the schema of the experiment to research focus of probes

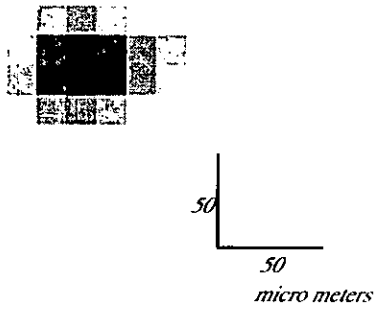

Figure 2.27: spot images of incident ray

shows that the correct focal position of the single is 1.6.

Figure 2.29 shows the result of this experiment. We defined the direction of the light axis as the horizontal axis of the graph. The left vertical axis of the graph shows the peak intensity of the bundle, and the right vertical axis shows the total intensities of single. We measured the both values by counts of the CCD, ADU. We see from the figure that the focal position of the single shifts from that of the bundle with difference of 1.6 mm. Moreover, the figure shows that the single, which exists on the focal position of the bundle, can capture only about 20 percents of total energy of the incident light.

Moreover, we researched the position at which intensity of the single image was the strongest by moving the translation stage in the directions perpendicular to the light axis. Figure 2.30 shows the image of the single at the position. We measured the total intensity of the single by moving the translation stage in the direction of the light axis. Five triangles in the Figure 2.29 show the results. We see from the figure that the focal position of the single shifts from that of

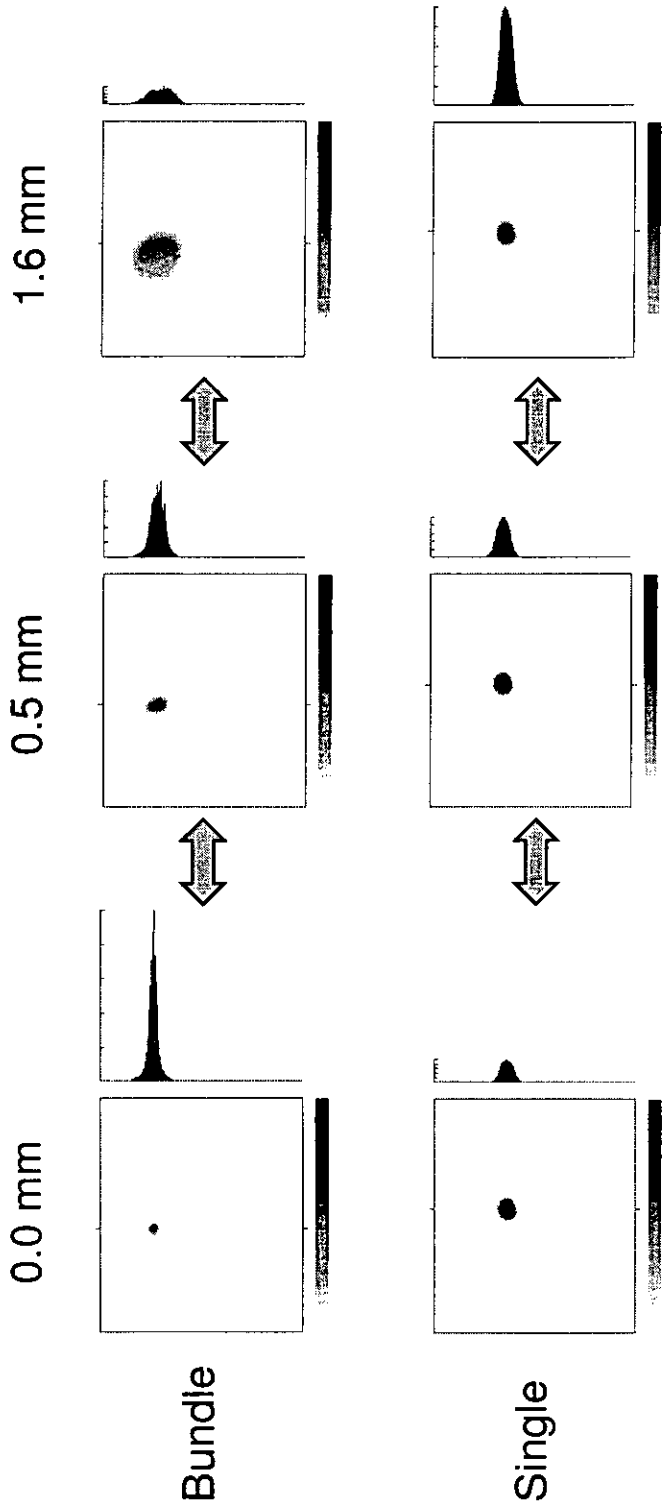

Figure 2.28: spot images of bundle and single

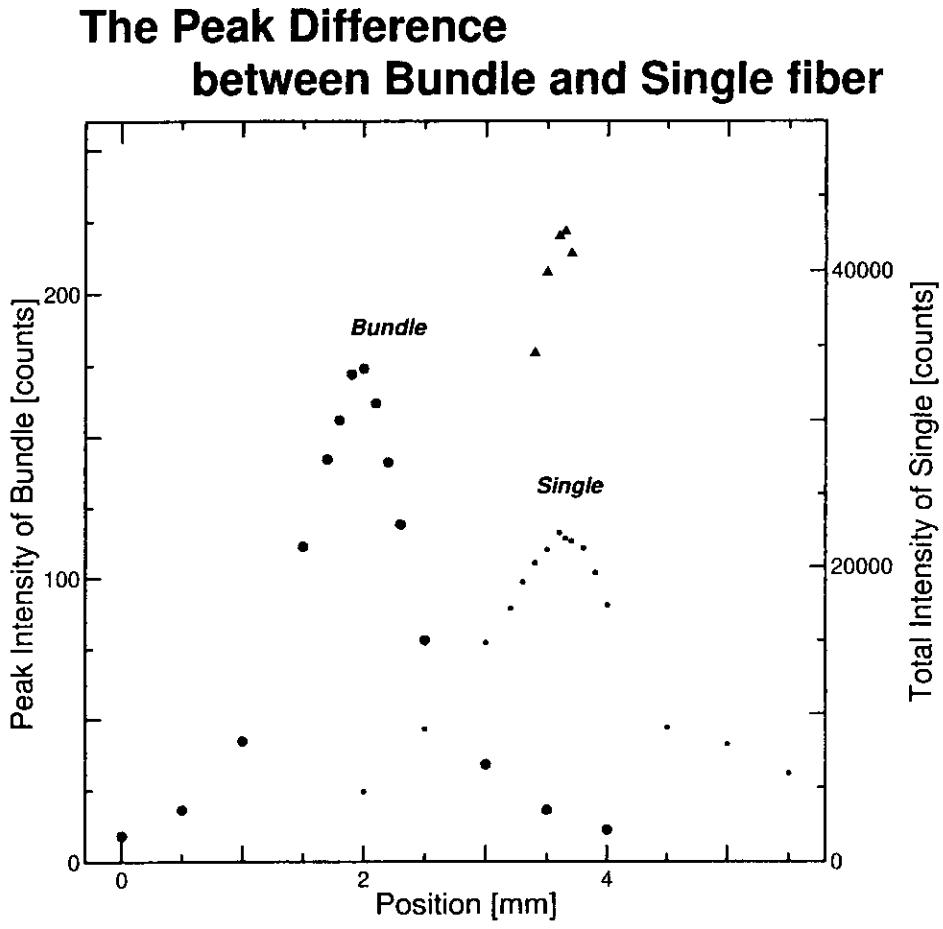

Figure 2.29: We investigated the focusing position of the bundle and the single. Five triangles show the data of the single at optimized positions.

the bundle with difference of 1.65 mm. Moreover, the figure shows that the single, which exists on the focal position of the bundle, can capture only about 10 percents of total energy of the incident light.

The result of the practical experiment agrees extremely with the result obtained by the ray-trace simulation (Table 2.3). The difference of focal positions between the bundle and the single obtained from these experiments agrees with the result calculated by geometrical optics (Table 2.4).

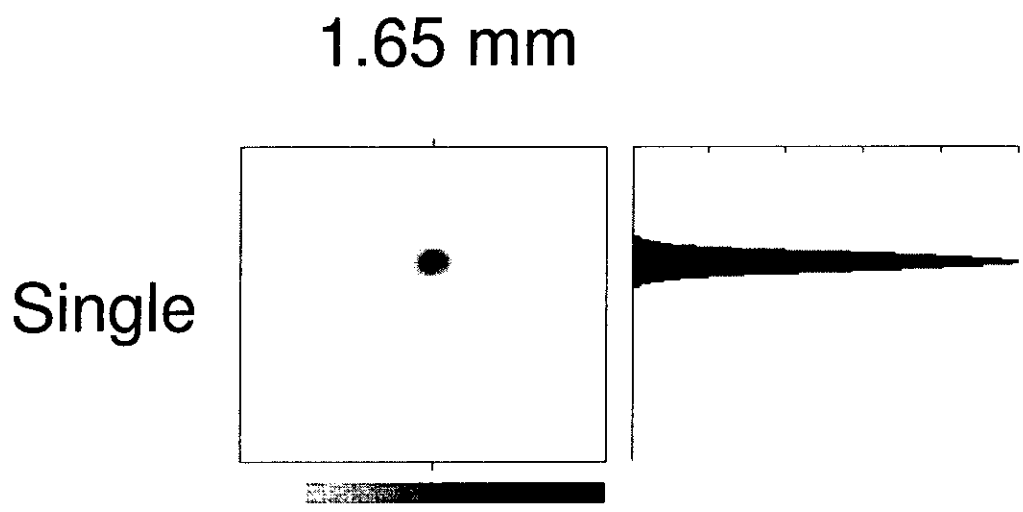

Figure 2.30: spot image at the best optimized position of the single

	Spot Size of Incident Light	Intensity Ratio relative to Max.
ray-trace simulation	$12.6\mu m$	13%
experiment	$60\mu m$	10%

Table 2.3: We see from the ray-trace simulation and the experiment that the previous single catches the light of about 10 %.

	Focus Difference
Experiment	$1.65mm$
Theory	$1.63mm$

Table 2.4: focus difference between Singles and Bundles

To solve this problem, we obtained the correct position of the prism in the single by performing ray-trace simulation. Figure 2.31 shows prism of the single which is put to the correct position determined by the simulation. The spot image at the right side of optical flat substrates is shown in figure 2.32. The figure shows that the radius of the spot is 0.0125 mm (root-mean-square). This spot size corresponds to 0.0012 mm or 0.027 arcsec at Newton focal surface of the Okayama 188cm telescope. Since the diameter of the practical fiber core, 113 μm, corresponds with 2.35 mm in the simulation, we see from Figure 2.33 that the single can sufficiently receive incident light. As the result of the simulation, we knew that the single's prism should be laid at backward position with 1.45 mm relative to the bundle's prism. This result agrees with the result calculated by geometrical optics.

Following the result, we started to make new probes. There were the thirty bundles and the three bundles on the focal plate of the instrument. Since remaking the bundles was easier than doing the singles, we made new bundles. We investigated the focusing position of the new bundles and the singles by performing the same experiment as we previously did. Figure 2.34 shows the result of the experiment. Since we changed the part of incident light, variations of intensity of the single was not sensible relative to the position. The focusing positions of the bundle A and B agreed with those of the singles, however, the bundle C did not agree with those of the singles. This means that we could not make the bundle C accurately. Therefore, we determined using only the bundle A and B.

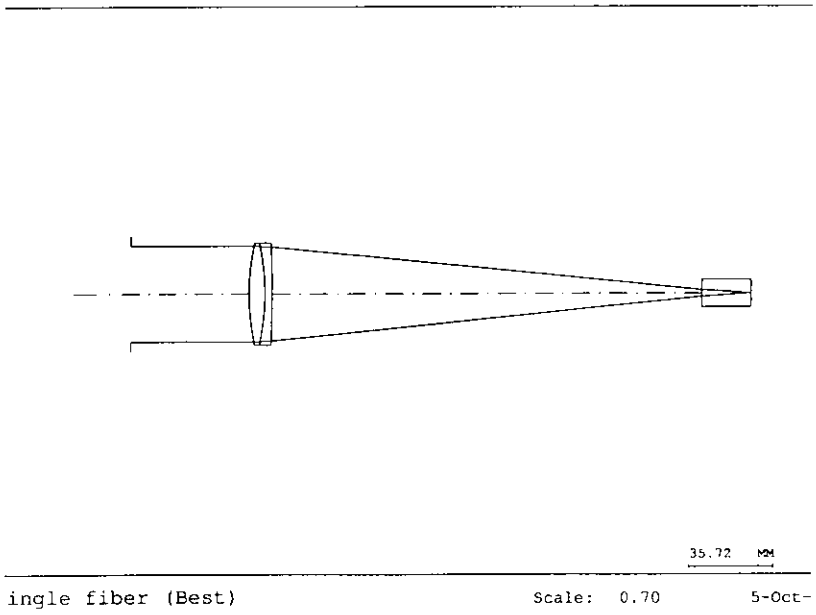

Figure 2.31: the best position of single probe

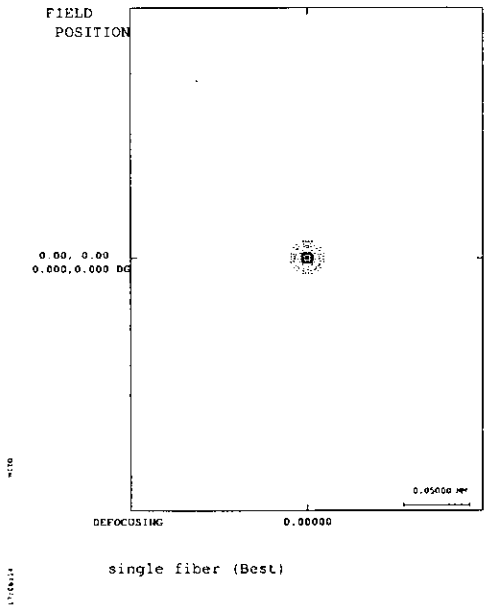

Figure 2.32: spot diagram at the best position

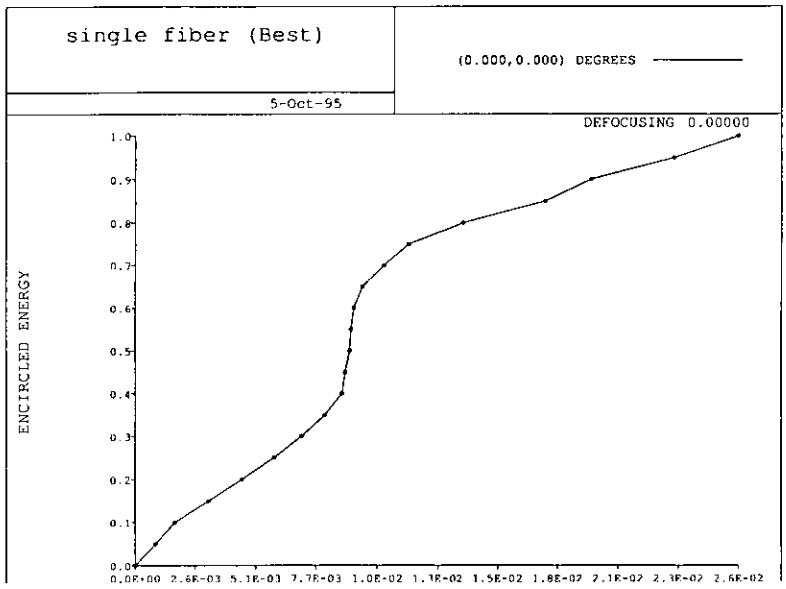

Figure 2.33: energy distribution at the best position

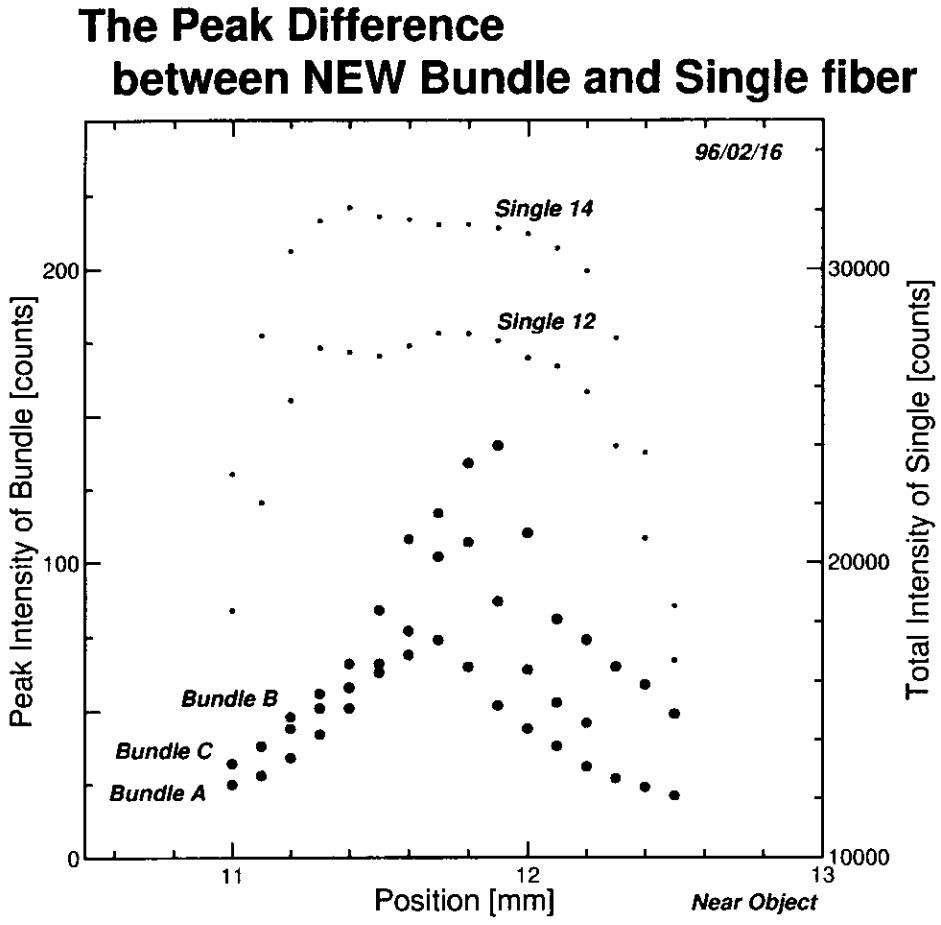

Figure 2.34: We investigated the focusing position of the new bundle probes and the singles. The focusing positions of bundle A and B agree with the singles, however, bundle C does not agree with the singles. we determined using only the bundle A and B.

Field (star numbers)	exposure time [min.]	total [min.]
SA110 (5)	$10 \times 1, 45 \times 1$	55
SA113 (12)	$30 \times 3, 10 \times 3$	120
SA92 (5)	$30 \times 2, 10 \times 1$	70

Table 2.5: observation in August 1997

2.3 Evaluative Observation in 1997

We observed to evaluate the improved instrument on 21st to 24th in August 1997. The purposes of the observation are to evaluate the light power of objects and efficiency of practical working under the observation after the improvements. We observed the stars in Equatorial Selected Area [11] $110 - 115, 92$ (α : $18.5 - 1$h) whose magnitudes were mv= $10 \sim 15$. The magnitudes of these stars were obtained precisely by photometric observations. Besides Wolf1346, Feige110, and BD+28 4211 were selected as spectro-photometric standard stars [3]. These magnitudes are mv= 11.5, 11.8, and 10.5, respectively.

We confirmed from the images of observations that the magnitude of the darkest star among the stars detected continuum spectrum was mv = 14.4 and color distribution of star was different each other.

The kinds of system of the instrument functioned normally. This observation was done by only two people in a day. Although some parts of the device such as the position measurement algorithm by the thresholding method had not been developed yet, the operation of instrument was easy enough for two people to perform.

Chapter 3

RESULTS OF THE IMPROVEMENTS

Table 3.1 shows conditions of the instrument in 1999 after the improvements. Basic mechanical functions and operations had been already achieved in 1994, as we have mentioned before.

The adjustment of fiber position was realized by the improvements including reconstruction of the system. As a result, positional accuracy of fiber probes became about 20 μm with a dramatical increase of the light throughput. This led to the possibility to observe for point source objects. In addition, we have solved some optical problems, the differences of imaging surfaces and positions of a object and a fiber probe by the viewing optics, and the difference of imaging surfaces of the spectral fiber probes and bundle fiber probes to guide the telescope. Consequently, the further increase of the throughput was expected. In the observation in April and May 1999, we obtained the spectra of S/N 100 with 1.25 minutes exposure for the star of mv= 10. This value is still lower than the one for the Okayama Cassegrain Spectrograph. However, it is important to take scientific data at this stage of development.

	1999	**goal**
basic functions and operations	OK	
positional accuracy	20μm	15μm
throughput	1.25 min., S/N 100 about star(mv= 10)	0.6 min., S/N 100 about star(mv= 10)
fiber placement speed /field /30 fibers	1.8 hours	1.5 hours
adjustment of fiber position	OK (automatic operation)	
number of observed stars /a night ($\sim$ 8 hours)	120	150

Table 3.1: the conditions in 1999

Both systems of the viewing optics and of the new instrument were unified. As a result, information of the position measured by the viewing optics were fed back into the positioner. Moreover the sequence to correct the probe position was automated. New operating software always surveys probes conditions and automatically judges what action to do next. The positioning procedure progresses automatically. If some accident happens, we can suspend and resume it anytime. Thus the operation of the instrument became easy and fast.

We developed a new algorithm to detect the positions of the probes and the objects by using the images of the observation in 1997. These images included the one of the star of mv $\approx$ 15. New algorithm could detect all positions of them.

Let us see how long will it take to observe thirty stars of mv= 10 with the instrument. It will take 20 minutes to change the field of view, to arrange bundle fiber, and to set automatic guide of the telescope. Another 90 minutes will be

needed to measure the object positions and to arrange fiber probes, and 1.25 minutes will be spent for exposure to obtain the spectra of S/N 100. Summing them up gives the total time of about 1.8 hours for one field. If observation time of one night is 8 hours, we can observe 120 objects by the instrument. We would like to emphasize that the time of 1.8 hours includes the one for adjustment of fiber positions. Previously, we spent 4 hours in arranging fiber probes without fine tuning of the positions.

Besides, we changed the method to observe by the instrument. At first, positions of all objects are measured by the viewing optics and the positions are recorded onto the file in a personal computer. Next, fiber probes are arranged to the positions recorded onto the files. In this method, only the first phase requires fine weather and probe arrangement phase does not need it. As a result, the method does never waste fine weather. This is suitable for Japanese climate that changes constantly. Practically, we confirmed that the method was effective with the observations in 1997 and 1999.

Chapter 4

OBSERVATION OF OPEN CLUSTERS

4.1 Motivations

The shape and magnitude of the Galactic radial abundance gradients in the disk provide essential constraints to models of the chemical evolution . Over the past decade a considerable number of studies have been made on the abundance gradients. The published estimates of the gradients were based primarily on the analyses of emission lines from H II regions and the absorption lines of luminous stars. A weak gradient not exceeding 0.1 dex/kpc has been observed in the sense that the outer Galaxy is more metal-poor.

There are some tracers to analyze the metallicity gradient, H II regions, B stars, planetary nebulae and so forth. B stars and H II regions, because of their short lifetimes express the present-day radial gradient. These two different tracers seemed to lead to controversial results. The gradient derived by B stars was much shallower (even flat) than the gradient traced by H II regions. However, the latest spectroscopic studies for larger and homogeneous sample of B stars indicated a

radial gradient $\Delta[O/H]/R_{gc} = -0.07$ dex/kpc (Smartt & Rollestone 1997), in agreement with the gradient deduced from H II regions, so that nowadays the former discrepancy appears to be solved.

Among these tracers, open clusters have long been used to trace the chemical structure and evolution of the disk, because they are relatively accurately dated and are observed in a wide range of distance and age. They form an excellent temporal sequence along which we can study the progress of overall enrichment in the disk. Moreover, since metallicity of a cluster is obtained by averaging metallicities of cluster members, it is possible to determine its metallicity rather accurately. A radial metallicity gradient for open clusters was first found by Janes(1979) [10]. Janes found $\Delta[Fe/H]/R_{gc} = -0.075 \pm 0.034$ dex/kpc by using fifteen old open clusters with ages older than 800 Myr. Taking advantage of the larger sample available in the Catalogue of Open Cluster Data (COCD) (Lynga 1987) [7], Janes et al(1988) [9] found a gradient of -0.14 dex/kpc for clusters with ages older than 200 Myr.

Friel & Janes (1993) [5] showed the extensive sample of old open clusters with metallicity determinations on a uniform abundance scale. With a sample supplemented by additional clusters with metallicities given in the Lynga catalog, they derived a radial abundance gradient of $\Delta[Fe/H]/R_{gc} = -0.095 \pm 0.017$ dex/kpc for thirty three clusters older than the Hyades that spanned Galactocentric distances from 7 to 16 kpc. Later, Friel (1995) showed the radial abundance gradient of $\Delta[Fe/H]/R_{gc} = -0.091 \pm 0.014$ dex/kpc by using the larger sample. At the same time it was shown that the dispersion of cluster metallicities about the mean at any distance was significant. The observed scatter about the linear fit, 0.17 dex, is significantly larger than the expected observational uncertainty. Figure 4.1 shows the metallicity gradients, $\Delta[Fe/H]/R_{gc} = -0.09$, presented by Carraro et al. (1998) [1] recently. Similarly, we see that there is a large scatter

in the relation.

The question we have to ask here is the reason for this dispersion. Figure 4.2 and 4.3 shows metallicity distribution of open clusters near the Sun. We used the data by Lynga(1987), Piatti et al.(1995), J. J. Claria et al.(1996), and A. E. Piatti et al.(1998) as the sample. It looks that the spatial scale length of the homogeneous metallicity distribution is a few hundred parsec. The dispersion of the metallicity distribution might be a result of superimposing these inhomogeneous regions round the circumference. If it is confirmed the regions with the homogeneous metallicity are on the order of a few hundred parsec, this would constraint to models of Galactic chemical evolution. We need to get more metallicity sample. Moreover, to study the present metallicity distribution, we determined to observe younger cluster near the Sun.

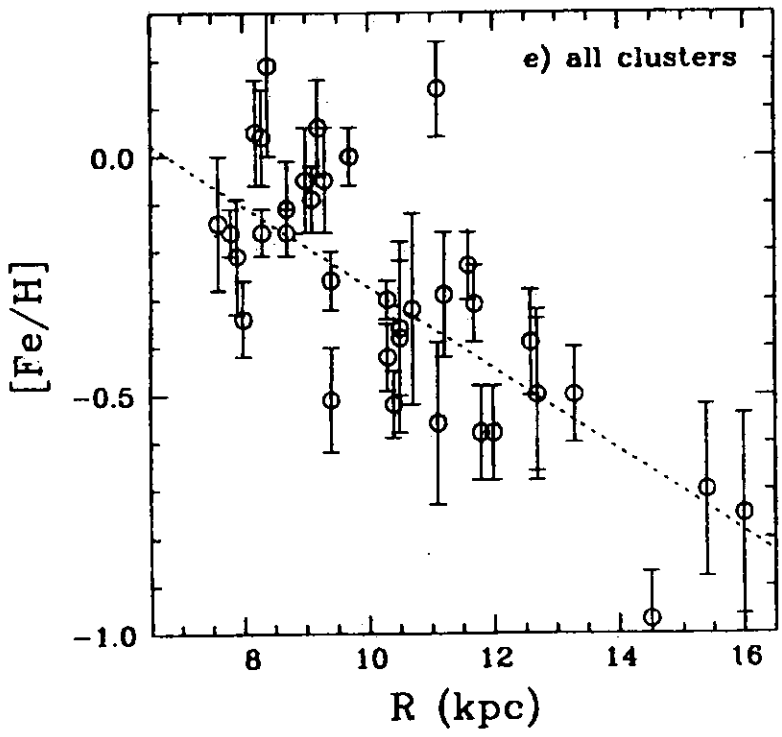

Figure 4.1: metallicity gradient of our Galaxy (Carraro et al. 1998 [1])

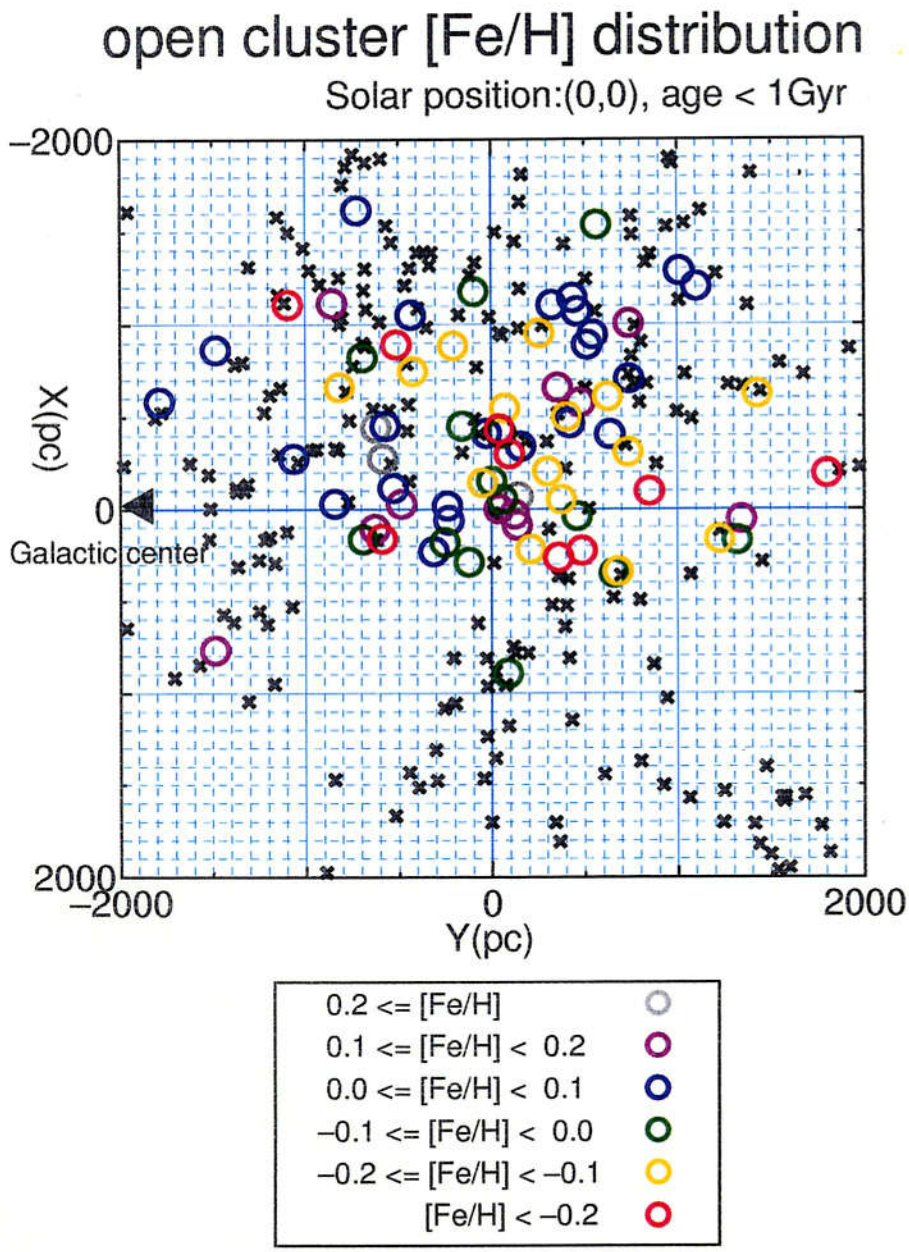

Figure 4.2: Metallicity distribution with open clusters near the Sun (face on). Crosses show the clusters unmeasured metallicity.

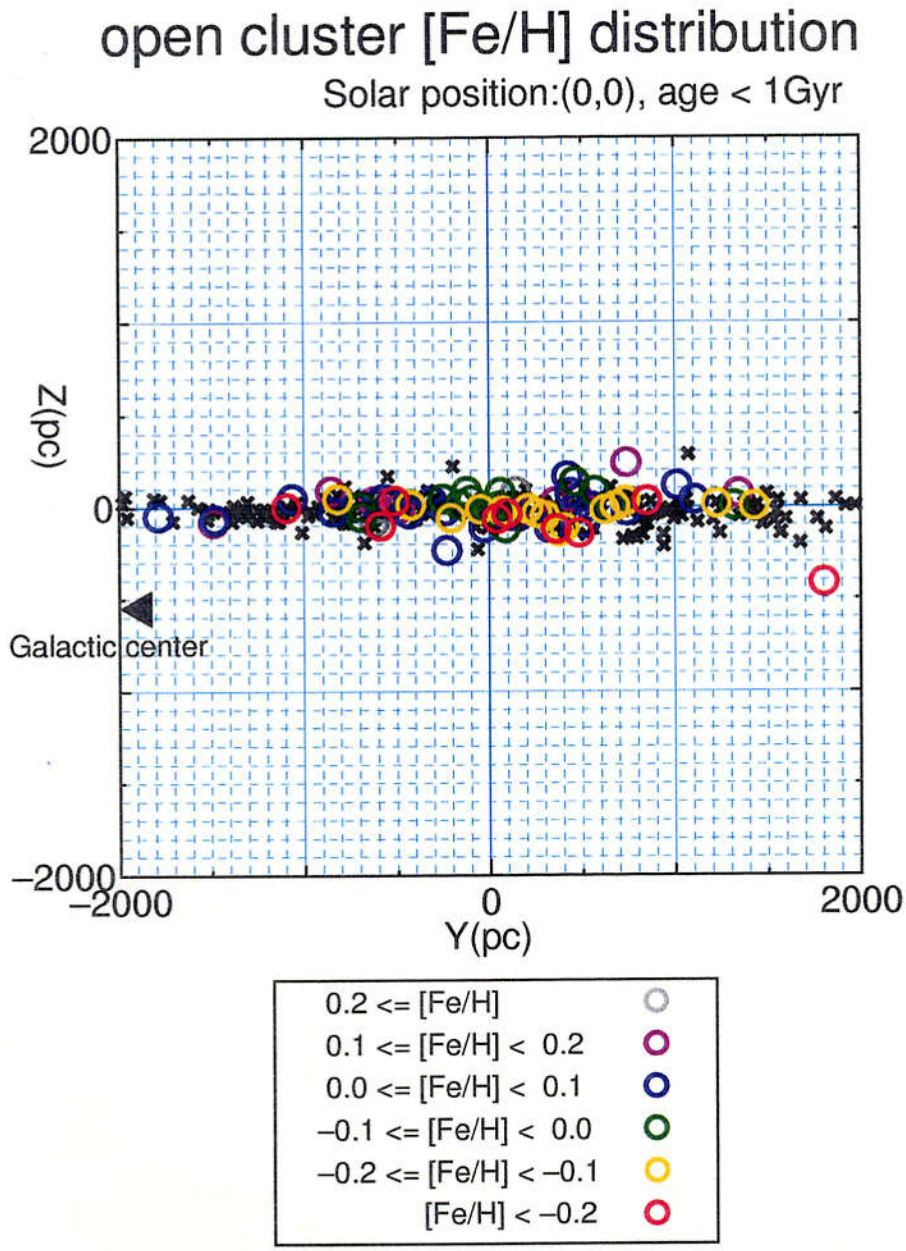

Figure 4.3: (edge on)

4.2 Observational Specifications

4.2.1 Characteristics of the Instrument and the Telescope

Field of view of Okayama Fiber Multi-Object Spectrograph is 1 degree. The number of probes which receive photons of astronomical objects are thirty. Additionally, signal-to-noise ratio of the spectra is about one hundred, observing the star with mv = 10 and 1.25 minutes exposure. These parameters show that the instrument is extreamely suitable to observe open clusters near the Sun. Therefore, we used Okayama Fiber Multi-Object Spectrograph for observing the nearby clusters.

4.2.2 Resolution of Spectrograph

Cluster metallicities have been derived by a wide variety of methods. Photometric abundance indicators in the systems of DDO, UBV, Washington or Stromgren photometry has been used extensively. Spectroscopic determinations have been far fewer, and large samples have been achieved only with moderate to a low resolution(Friel & Janes 1993 [5], Thogersen et al 1993 [18]). There have been relatively few abundance determinations from high-resolution spectroscopy because of the faintness of the clusters.

To derive cluster metallicities, we used the method presented by Friel(1987) [6]. Friel defined fifteen spectroscopic metallicity indices(Table 4.1). The indices are represented as the ratio of the average flux centered on a feature with that of two continuum bands on either side. The indices are calculated by taking the ratio of average flux in a central feature bandpass to that in continuum bandpasses. The ratio is expressed in the form of a magnitude. For example, the

Index	Central Bandpass	Continuum Bandpasses	Species Measured	Criterion
Mg	5130.00 - 5200.00	4935.00 - 4975.00	Mg b + Mg H	Liminosity
		5303.00 - 5367.00		[Fe/H]
Ca4226	4207.00 - 4245.00	4115.00 - 4165.00	Ca I	Liminosity
		4320.00 - 4370.00		
G-Band	4245.00 - 4320.00	4120.00 - 4200.00	CH, Fe I	Liminosity
		4425.00 - 4520.00		
CN 4216	4144.00 - 4177.75	4082.00 - 4118.25	$CN(B^2\Sigma^+ - X^2\Sigma^+)$	Liminosity
		4246.00 - 4284.75		[Fe/H]
CN 3883	3850.00 - 3885.00	3610.00 - 3730.00	$CN(B^2\Sigma^+ - X^2\Sigma^+)$	Liminosity
		4020.00 - 4130.00		
Mg3838	3696.00 - 3776.00	3776.00 - 3896.00	Fe I, Mg I, CN	Liminosity
Ca II H+K	3910.00 - 4000.00	3650.00 - 3780.00	Ca II	[Fe/H]
		4020.00 - 4130.00		
Fe4065	4033.50 - 4085.00	4006.00 - 4038.00	Fe I, Mn I, Sr II	[Fe/H]
		4085.00 - 4115.00		
Fe4530	4520.00 - 4571.25	4498.75 - 4520.00	Fe I, Ti I, Ti II	[Fe/H]
		4606.00 - 4636.00		
Fe4680	4636.00 - 4723.00	4606.00 - 4636.00	Fe I, Cr I, Ni I	[Fe/H]
		4736.00 - 4773.00	Mg I	
Fe4920	4900.00 - 4940.00	4796.00 - 4841.00	Fe I	[Fe/H]
		4935.00 - 4975.00		
Fe5011	4976.00 - 5051.00	4935.00 - 4975.00	Fe I, Ti I, Fe II	[Fe/H]
		5051.00 - 5096.00	Ni I	
Fe5270	5248.00 - 5286.75	5220.00 - 5250.00	Fe I, Ca I	[Fe/H]
		5288.00 - 5322.00		
Fe5335	5314.75 - 5353.50	5307.25 - 5317.25	Fe I, Cr I	[Fe/H]
		5356.00 - 5364.75		
Fe5400	5384.00 - 5430.00	5356.00 - 5365.00	Fe I	[Fe/H]
		5430.00 - 5460.00		

Table 4.1: metallicity indices defined by Friel (1987)

index that measures the Mg b and Mg H feature is defined as:

$$\mathrm{Mg} = -2.5 \log \frac{\int_{5130}^{5200} \mathrm{F}_\lambda \mathrm{d}\lambda / 70\text{Å}}{\int_{4935}^{4975} \mathrm{F}_\lambda \mathrm{d}\lambda / 40\text{Å} + \int_{5303}^{5367} \mathrm{F}_\lambda \mathrm{d}\lambda / 64\text{Å}}.$$

Friel has assumed that the spectral features are affected by only three possible parameters - the temperature, the surface gravity, and the chemical abundances of the star, and further that $(\mathrm{B}-\mathrm{V})_0$ is an adequate temperature indicator. On this assumption, we can obtained the metallicity of stars with the spectra, when we know $(\mathrm{B}-\mathrm{V})_0$ and luminosity class of the stars. Friel showed the means to measure the metallicity of giant and subgiant stars.

We used the spectrograph Jobin Yvon CP200. Resolution of the spectrograph is less than 4.5nm ($\lambda/\Delta\lambda \approx 100$). This value is less than resolution of the spectra used by Friel ($\lambda/\Delta\lambda \approx 500$). Therefore, we estimated the feasibility before the observation, whether the resolution of our spectrograph is adequate to measure metallicites. We used "A Library of Stellar Spectra" (Jacoby et al.1984 [8]) for the preliminary study. Resolution of the spectra was $\lambda/\Delta\lambda = 500$ and approximated to Friel's. We compared the indices obtained from the original spectra with the indices obtained from the spectra convoluted by Gaussian distribution.

Table 4.2 shows the stars used to estimate changes of the index versus a spectral resolution. We selected the stars whose luminosity class was giant or subgiant, $(B - V)_0$ was more than 0.5. Number of the stars was twenty-three. Figure 4.4 shows the original spectra of HD21110 by Jacoby, and the regions used to obtain the Fe4680 index. Figure 4.5 and 4.6 shows the spectra convoluted by Gaussian distribution with $\sigma = 5\mathring{A}$ and $\sigma = 10\mathring{A}$, respectively.

The index values obtained from the convoluted spectra are shown plotted against the ones which obtained from the original in figure 4.7 - 4.36.

The results did not suggest an adequate correlation in some indices, although those showed an adequate correlation in more indices. Therefore we determined to observe the stars for calibrating the indices whose indices had been measured by Friel. Moreover, this permits to keep out of the error resulting from difference of the spectra obtained by the spectrograph CP200 from the spectra of the model.

Name	Sp. Type	Luminosity Class	$(B-V)_0$
HD 9979	F8	III	.54
BD+302347	G0	III	.58
HD 15866	G0	III	.64
HD 78277	G2	IV	.64
HD 25894	G2	III	.72
HD 70178	G5	IV	.72
HD 112872	G6	III	.80
SAO 55155	G9	III	.83
HD 2506	G4	III	.89
HD 29883	G6	III	.89
BD+281885	G5	III	.91
HD 26514	G6	III	.94
HD 249240	G7	III	.95
HD 245389	G8	III	.98
SAO 55164	K0	III	1.01
HD 33506	K2	III	1.16
SAO 77849	K2	III	1.17
HD 26946	K3	III	1.32
HD 21110	K4	III	1.45
SAO 62808	M5	III	1.45
SAO 63349	M3	III	1.54
SAO 21753	K7	III	1.55
HD 110964	M4	III	1.56

Table 4.2: We used spectra of these stars to estimate changes of the index versus a spectral resolution.

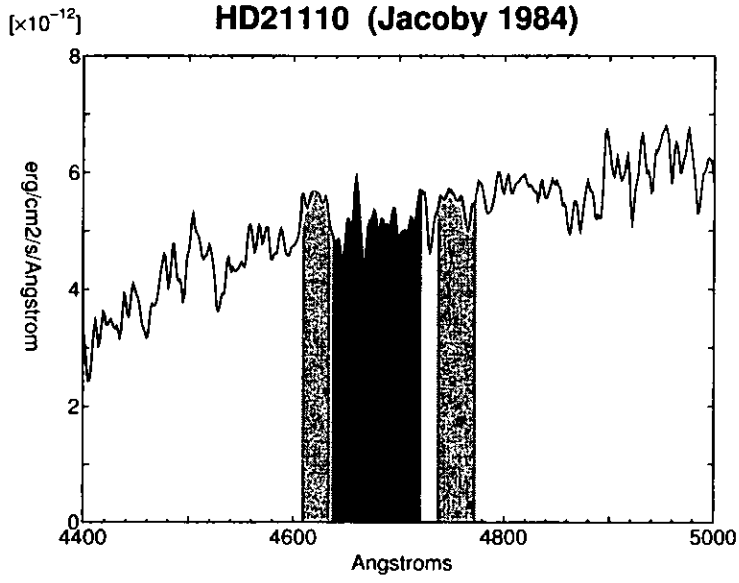

Figure 4.4: The spectrum of HD21110 presented by Jacoby (1984). Dark gray region shows central bandpasses for Fe4680 index. Two light gray regions show continuum bandpasses for that.

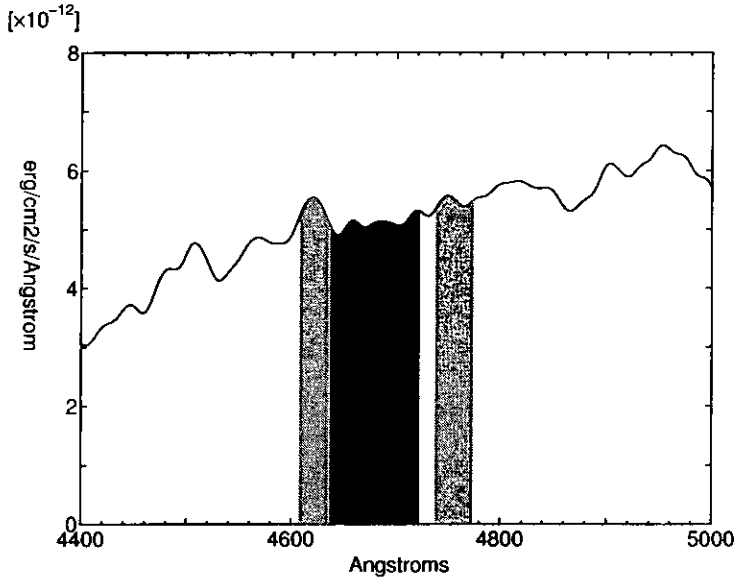

Figure 4.5: The spectrum of HD21110 convoluted by Gaussian distribution with $\sigma = 5\mathring{A}$.

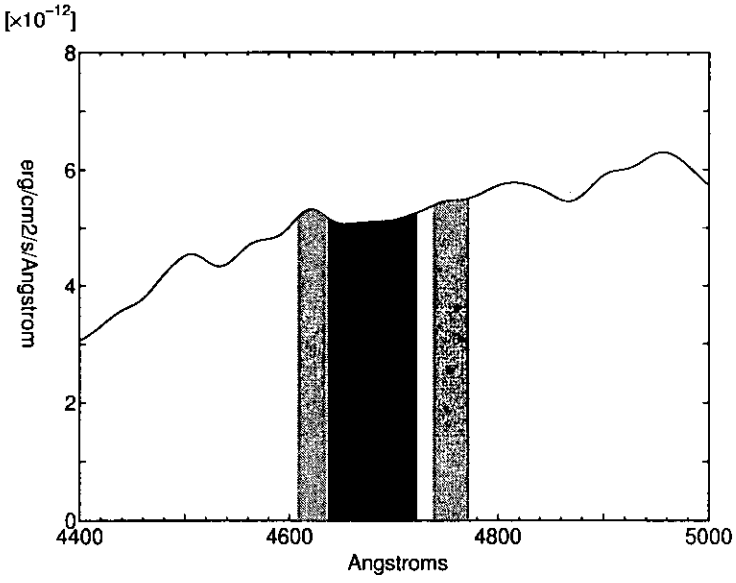

Figure 4.6: The spectrum of HD21110 convoluted by Gaussian distribution with $\sigma = 10\mathring{A}$.

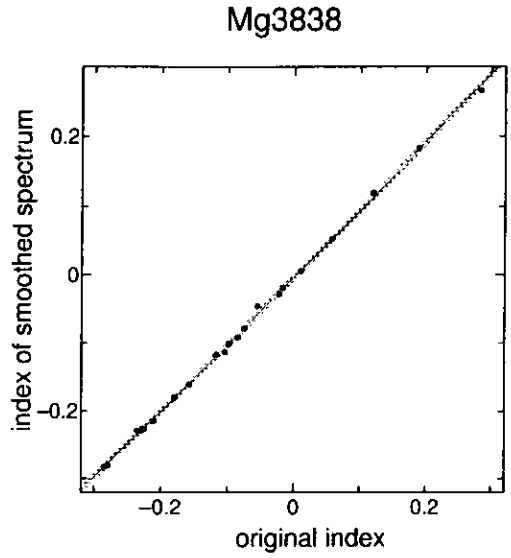

Figure 4.7: Index correlation of the spectra convoluted by $\sigma = 5\mathring{A}$ versus original.

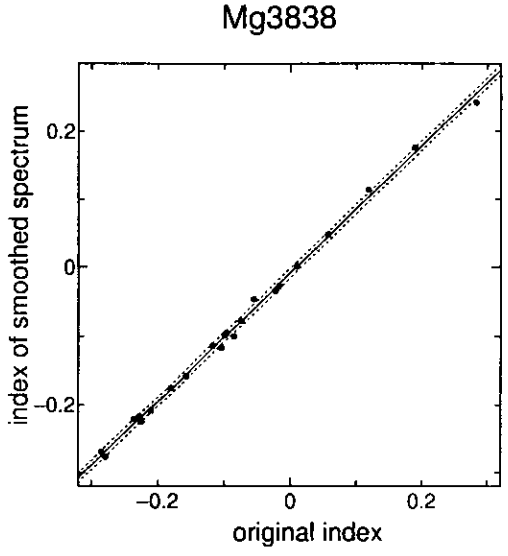

Figure 4.8: Index correlation of the spectra convoluted by $\sigma = 10\mathring{A}$ versus original.

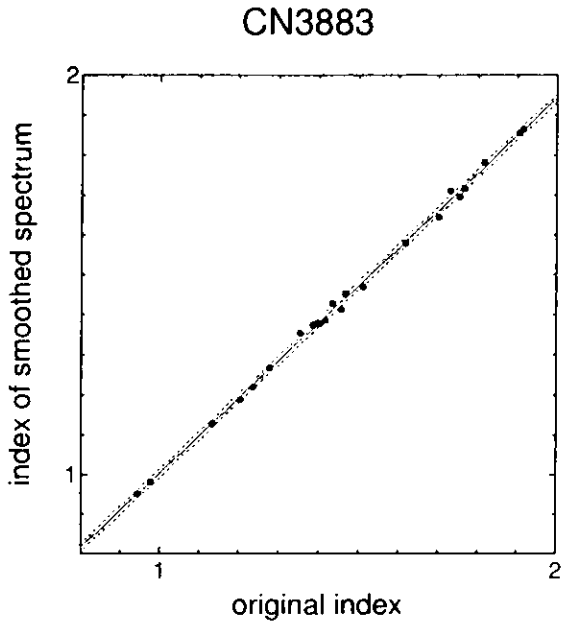

Figure 4.9: Index correlation of the spectra convoluted by $\sigma = 5\mathring{A}$ versus original.

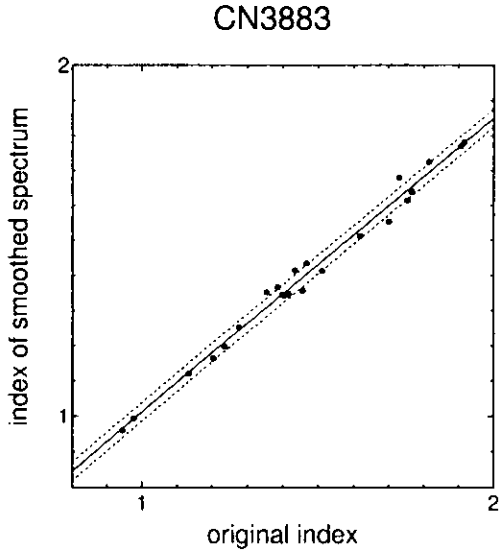

Figure 4.10: Index correlation of the spectra convoluted by $\sigma = 10\mathring{A}$ versus original.

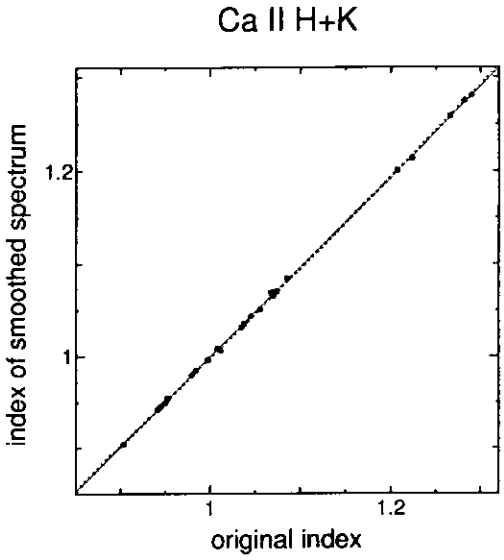

Figure 4.11: Index correlation of the spectra convoluted by $\sigma = 5\mathring{A}$ versus original.

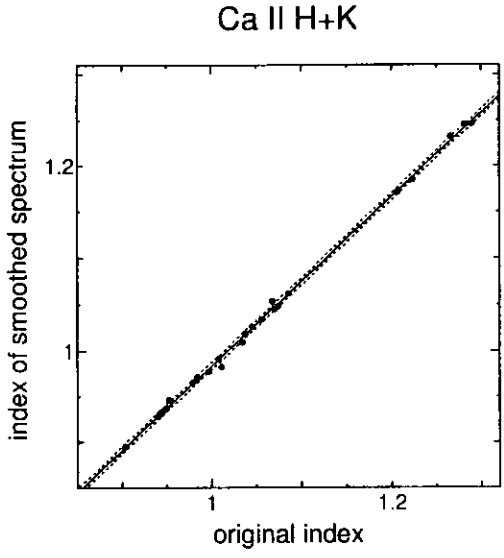

Figure 4.12: Index correlation of the spectra convoluted by $\sigma = 10\mathring{A}$ versus original.

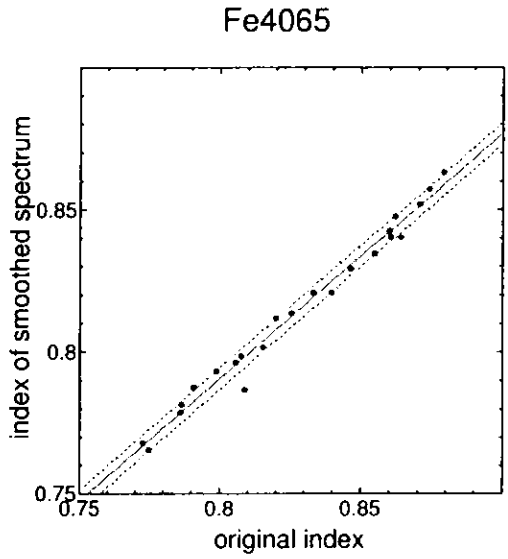

Figure 4.13: Index correlation of the spectra convoluted by $\sigma = 5\mathring{A}$ versus original.

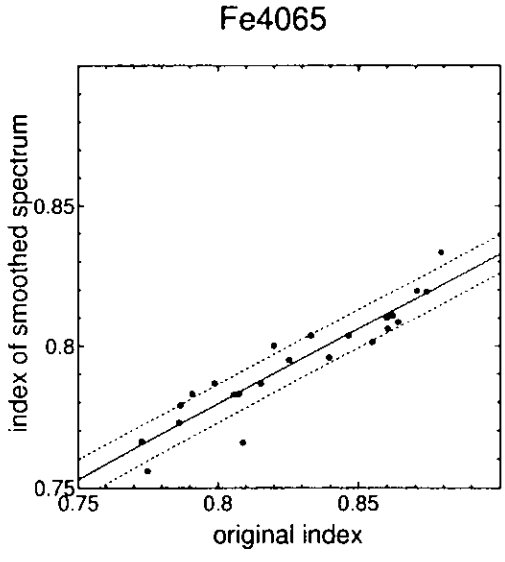

Figure 4.14: Index correlation of the spectra convoluted by $\sigma = 10\mathring{A}$ versus original.

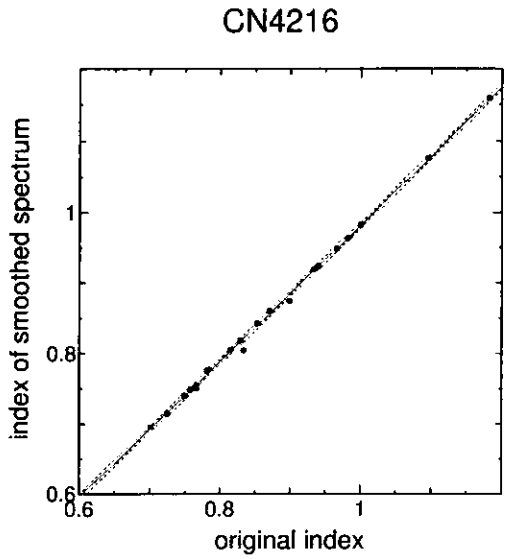

Figure 4.15: Index correlation of the spectra convoluted by $\sigma = 5\mathring{A}$ versus original.

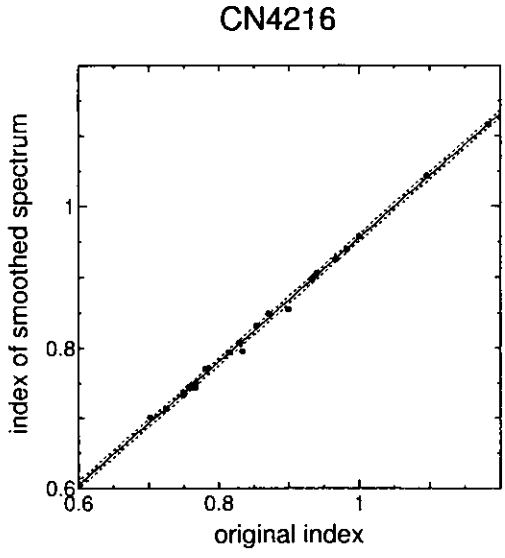

Figure 4.16: Index correlation of the spectra convoluted by $\sigma = 10\mathring{A}$ versus original.

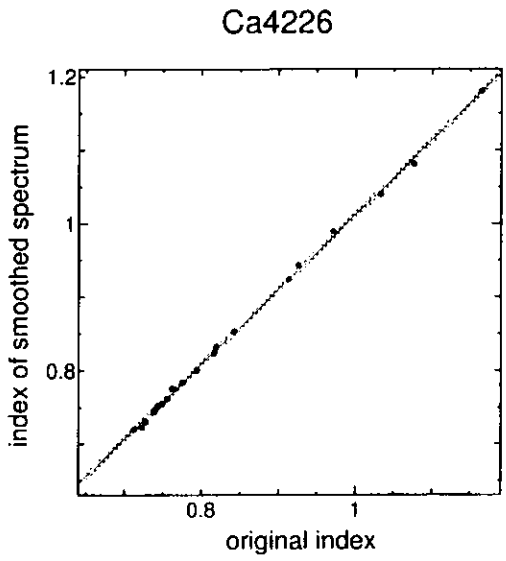

Figure 4.17: Index correlation of the spectra convoluted by $\sigma = 5\mathring{A}$ versus original.

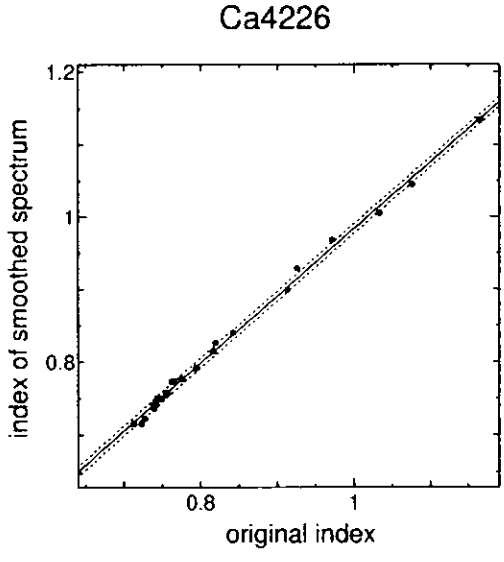

Figure 4.18: Index correlation of the spectra convoluted by $\sigma = 10\mathring{A}$ versus original.

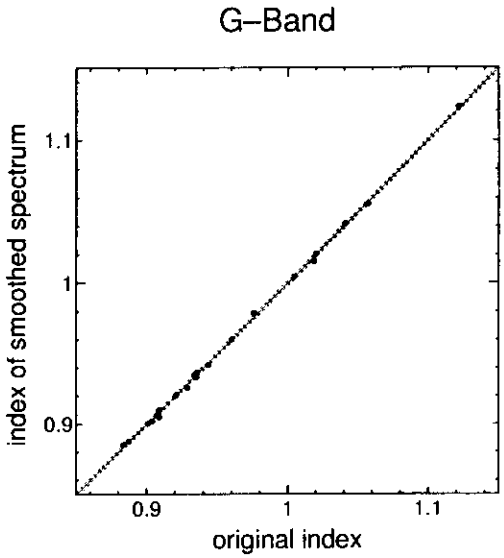

Figure 4.19: Index correlation of the spectra convoluted by $\sigma = 5\mathring{A}$ versus original.

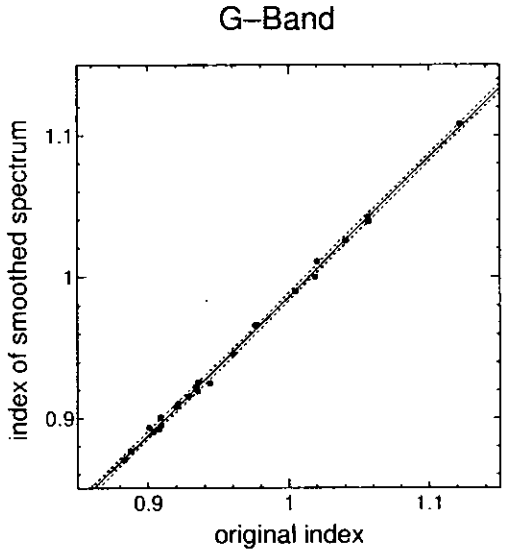

Figure 4.20: Index correlation of the spectra convoluted by $\sigma = 10\mathring{A}$ versus original.

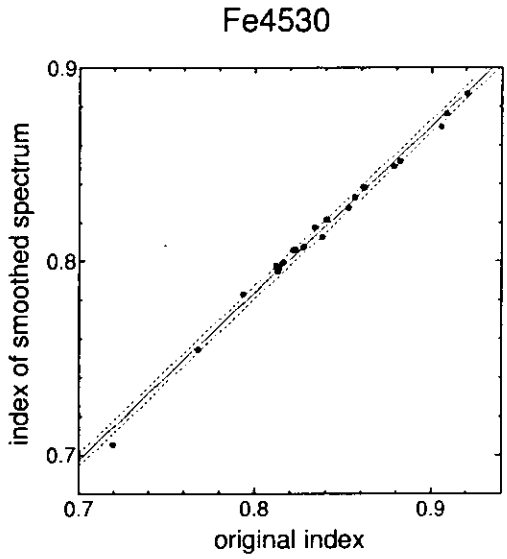

Figure 4.21: Index correlation of the spectra convoluted by $\sigma = 5\mathring{A}$ versus original.

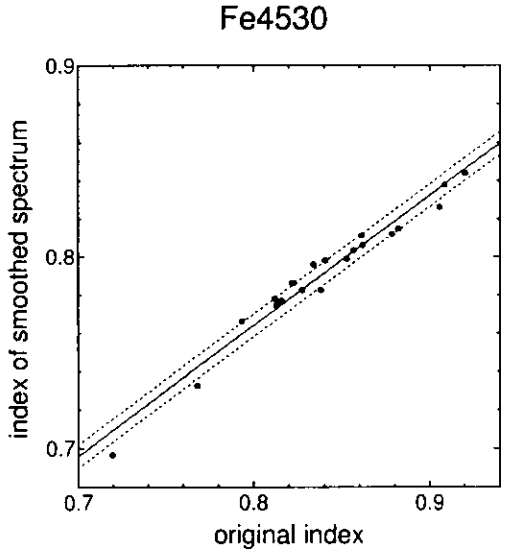

Figure 4.22: Index correlation of the spectra convoluted by $\sigma = 10\mathring{A}$ versus original.

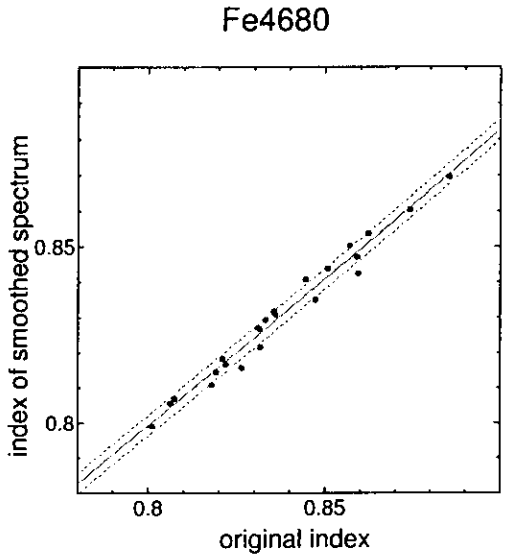

Figure 4.23: Index correlation of the spectra convoluted by $\sigma = 5\mathring{A}$ versus original.

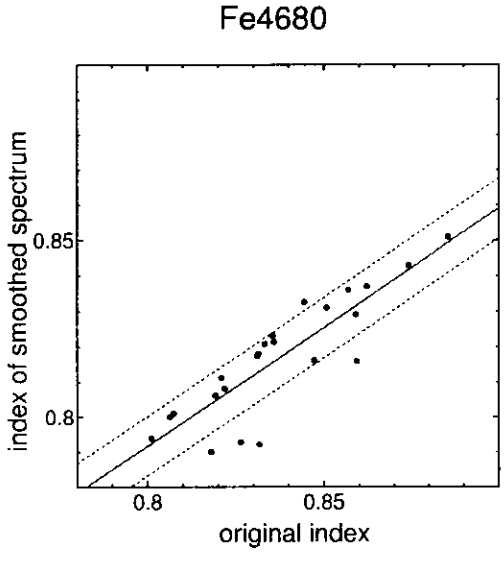

Figure 4.24: Index correlation of the spectra convoluted by $\sigma = 10\mathring{A}$ versus original.

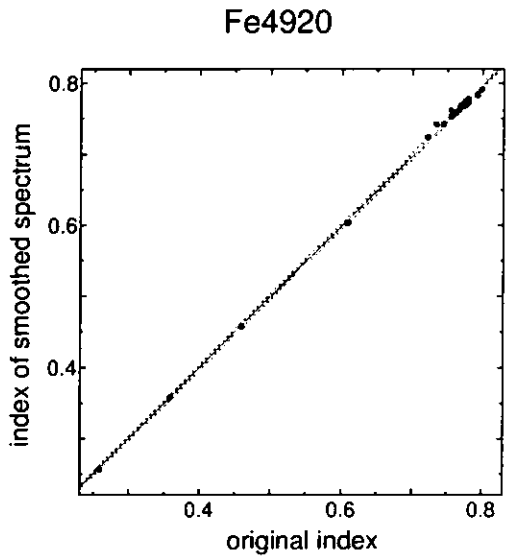

Figure 4.25: Index correlation of the spectra convoluted by $\sigma = 5\mathring{A}$ versus original.

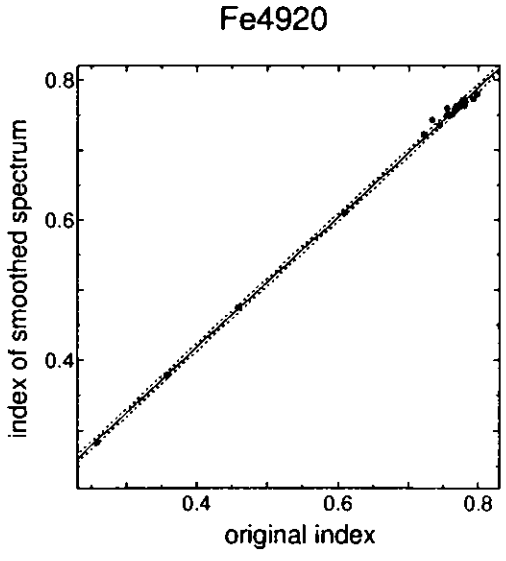

Figure 4.26: Index correlation of the spectra convoluted by $\sigma = 10\mathring{A}$ versus original.

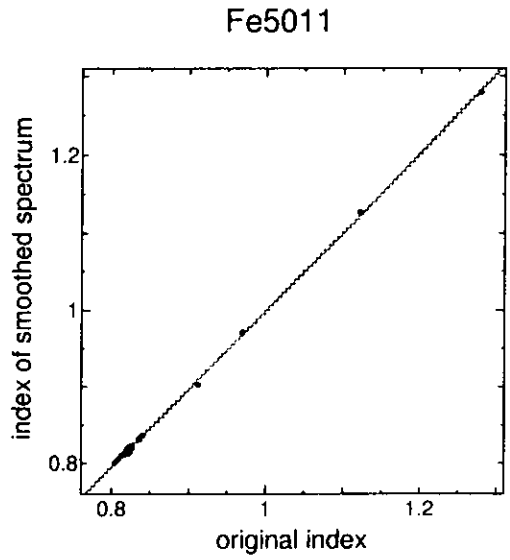

Figure 4.27: Index correlation of the spectra convoluted by $\sigma = 5\mathring{A}$ versus original.

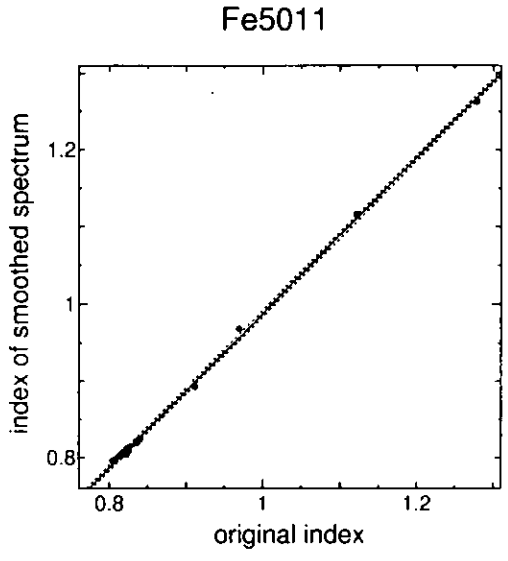

Figure 4.28: Index correlation of the spectra convoluted by $\sigma = 10\mathring{A}$ versus original.

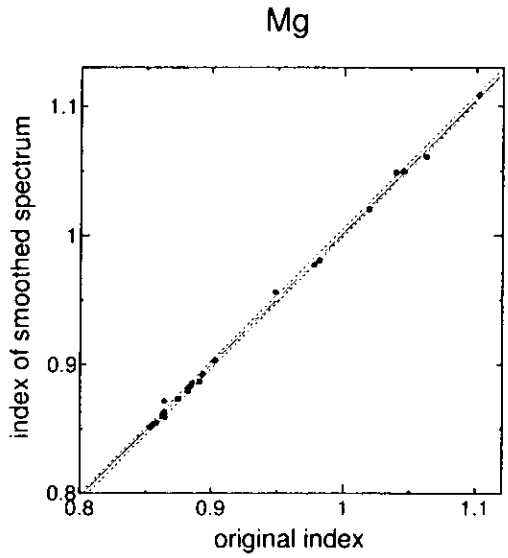

Figure 4.29: Index correlation of the spectra convoluted by $\sigma = 5\mathring{A}$ versus original.

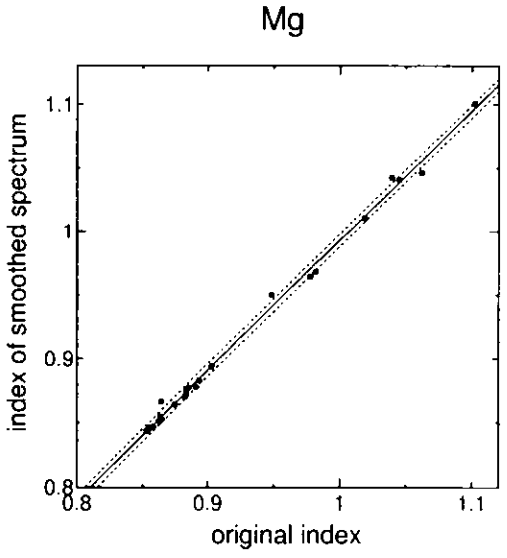

Figure 4.30: Index correlation of the spectra convoluted by $\sigma = 10\mathring{A}$ versus original.

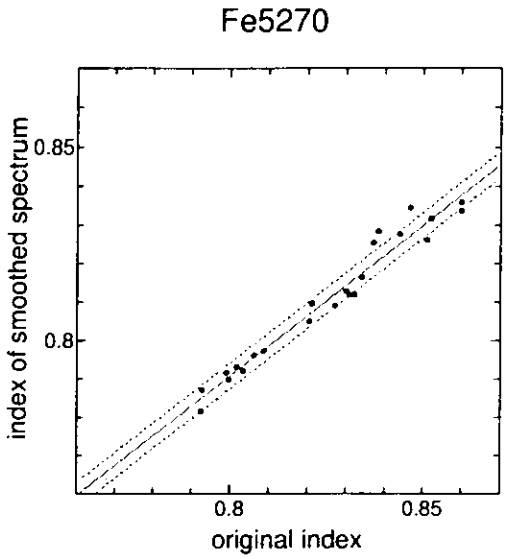

Figure 4.31: Index correlation of the spectra convoluted by $\sigma = 5\AA$ versus original.

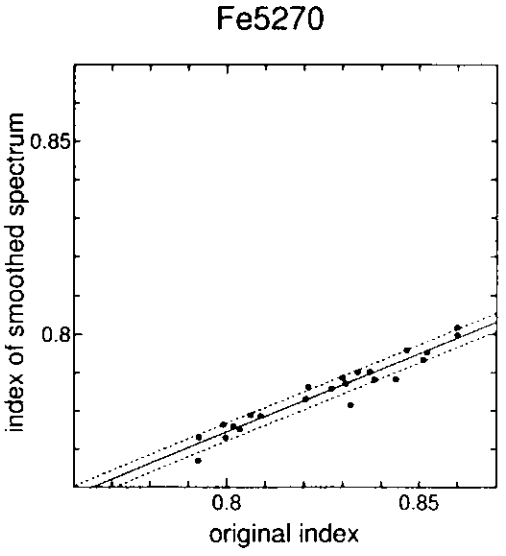

Figure 4.32: Index correlation of the spectra convoluted by $\sigma = 10\AA$ versus original.

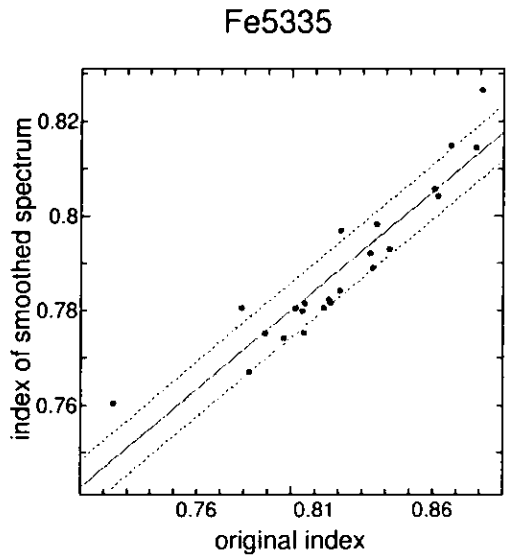

Figure 4.33: Index correlation of the spectra convoluted by $\sigma = 5\mathring{A}$ versus original.

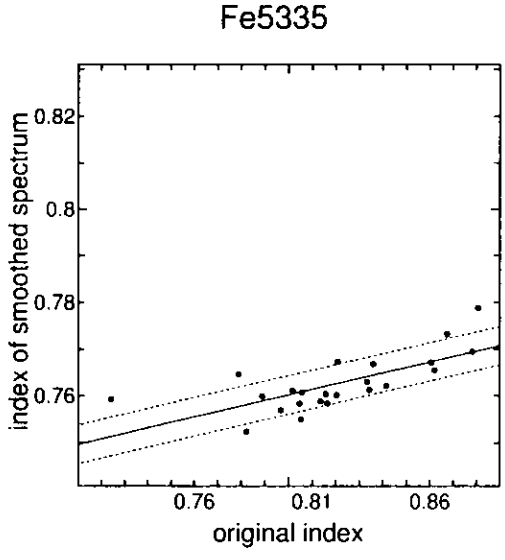

Figure 4.34: Index correlation of the spectra convoluted by $\sigma = 10\mathring{A}$ versus original.

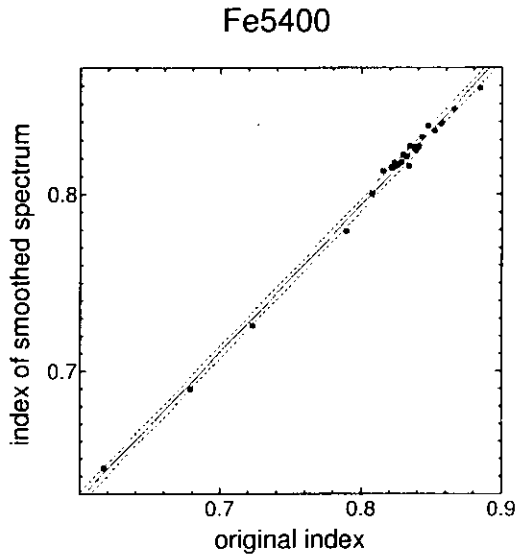

Figure 4.35: Index correlation of the spectra convoluted by $\sigma = 5\mathring{A}$ versus original.

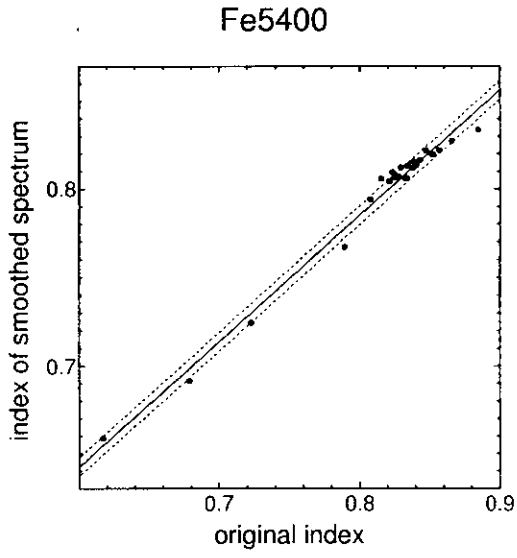

Figure 4.36: Index correlation of the spectra convoluted by $\sigma = 10\mathring{A}$ versus original.

Index	sigma(conv. 5Å)	sigma(conv. 10Å)
Mg3838	0.004	0.007
CN 3883	0.011	0.026
Ca II H+K	0.002	0.004
Fe4065	0.004	0.007
CN 4216	0.005	0.005
Ca4226	0.004	0.007
G-Band	0.002	0.003
Fe4530	0.003	0.006
Fe4680	0.003	0.008
Fe4920	0.004	0.006
Fe5011	0.003	0.004
Mg	0.003	0.005
Fe5270	0.003	0.002
Fe5335	0.006	0.004
Fe5400	0.003	0.005

4.3 Observation

From 30th April to 6th May in 1999, we observed open cluster stars and field stars at Okayama Astrophysical Observatory (OAO). Table 4.3 shows the object list. We used the OAO's 1.8-m telescope and the Okayama Fiber Multi-Object Spectrograph attached to the Newton focus. Fortunately, there were only two days that we could not observe at all, although we were troubled with high humidity.

4.3.1 Field Stars

We observed sixteen stars shown in Table 4.3 to calibrate the indices obtained by our observation. Friel observed these stars and determined the metallicity indices. Metallicities, [Fe/H], of the stars range from -0.67 to $+0.30$ dex. This criterion bases on typical metallicities of open clusters. Table 4.4, 4.5, and 4.6 show color, [Fe/H] and the indices presented in Friel's paper.

4.3.2 Open Clusters

We observed four open clusters NGC6709, IC4665, NGC6866, and NGC6633. For IC4665, we observed twice. The metallicity had not observed previously for the three clusters, NGC6709, IC4665, and NGC6866, but had been determined for one cluster NGC6633. We observed NGC6633 to estimate metallicity obtained by our observation. Table 4.7 shows the observed stars in these clusters. Numbers of observed stars of NGC6709, IC4665, NGC6866, and NGC6633 are 2,8,2, and 11, respectively. All of these stars are regarded as giant or subgiant from color-magnitude diagram of each cluster, and have the color of $(B-V)_0 > 0.5$. We referred to the coordinates, the spectral types, the magnitudes and the colors of the stars presented in SIMBAD, and to the extinction, $E(B-V)$, presented in

Object	exposure time [sec.]	Object	exposure time [sec.]
metallicity calibration stars		**open clusters (number)**	
HD1225560	60	NGC6709 (2)	2400
HD146470	600	IC4665 (8)	2400
HD112127	120	NGC6866 (2)	2400
HD108225	60	NGC6633 (11)	3000
HD117876	120	IC4665 (10)	2700
HD72324	600		
HD76291	600	**spectra calibration stars**	
HD81192	300	Feige34	1200
HD91612	120	Feige67	3600
HD100030	180	Feige34	3600
HD92588	300	HD192281	300
HD97907	60		
HD104304	60		
HD107328	30		
HD134063	600		
HD129312	30		

Table 4.3: objects list

the COCD (Lynga 1987) [7].

Figure 4.37 shows the image of IC4665 overlayed observational configuration of fiber probes. Figure 4.38 shows the raw image of the spectra. Thirty apertures of the fibers line up horizontally and each spectrum is observed vertically.

Name	$(B-V)_0$	[Fe/H]	Mg3838	CN3883	CaII	Fe4065
HD125560	1.230	+0.30	−0.0807	1.9449	1.1287	0.8539
HD146470	1.350	−0.67	0.0527	1.7068	1.3566	0.8089
HD112127	1.270	−0.09			1.1564	0.8793
HD108225	0.950	+0.01	−0.1657	1.6624	1.1183	0.8422
HD117876	0.960	−0.41	−0.1176	1.6379	1.1619	0.8022
HD72324	1.020	+0.22	−0.2640	1.8642	1.1257	0.8459
HD76291	1.090	+0.08	−0.1245	1.8346	1.1467	0.8648
HD81192	0.950	−0.57			0.7412	0.8402
HD91612	0.930	−0.21	−0.1314	1.6291	1.1156	0.8431
HD100030	0.880	−0.29	−0.1335	1.5546	1.1239	0.8199
HD92588	0.880	−0.25	−0.0398	1.5550	1.0726	0.8561
HD97907	1.200	−0.05	0.0894	1.4138	1.0865	0.8302
HD104304	0.760	+0.18			0.8387	0.8067
HD107328	1.160	−0.47	−0.0871	1.8127	1.2190	0.8151
HD134063	0.920	−0.60	−0.1330	1.5150	1.1243	0.7844
HD129312	1.010	+0.00	−0.1935	1.6605	1.1209	0.8453

Table 4.4: Friel indices of calibration stars

Name	CN4216	Ca4226	G-Band	Fe4530	Fe4680	Fe4920
HD125560	1.0678	0.9051	1.0182	0.8968	0.8945	0.7847
HD146470	0.8805	0.9637	1.1000	0.9005	0.8135	0.7351
HD112127	1.0114	0.8793	1.0114	0.9167	0.9479	0.7901
HD108225	0.9082	0.8555	0.9542	0.8539	0.8362	0.7611
HD117876	0.8529	0.8341	1.0018	0.8638	0.8215	0.7577
HD72324	1.0112	0.8291	0.9473	0.8834	0.8473	0.7755
HD76291	0.9386	0.8729	1.0352	0.8741	0.8488	0.7732
HD81192	1.0433	0.8402	1.0433	0.8435	0.8053	0.7666
HD91612	0.8628	0.8280	0.9928	0.8628	0.8255	0.7745
HD100030	0.8125	0.8294	1.0103	0.8439	0.8152	0.7666
HD92588	0.7954	0.8453	1.0529	0.8462	0.8427	0.7784
HD97907	0.9369	0.9016	1.0132	0.8944	0.8482	0.7706
HD104304	1.0099	0.8067	1.0099	0.8339	0.8497	0.7913
HD107328	0.9181	0.8669	1.0424	0.8820	0.8301	0.7655
HD134063	0.7805	0.8094	1.0492	0.8465	0.8051	0.7652
HD129312	0.9844	0.8235	0.9346	0.8654	0.8331	0.8021

Table 4.5: continued

Name	Fe5011	Mg	Fe5270	Fe5335	Fe5400
HD125560	0.8274	1.0369	0.8635	0.8803	0.8040
HD146470	0.8108	1.0258	0.8322	0.8444	0.8011
HD112127	0.8211	1.0643	0.8619	0.8538	0.8143
HD108225	0.8214	0.8716	0.8339	0.8523	0.7551
HD117876	0.8091	0.8913	0.8083	0.8118	0.7760
HD72324	0.8197	0.8798	0.8312	0.8410	0.7952
HD76291	0.8134	0.9658	0.8468	0.8464	0.8001
HD81192	0.7951	0.8781	0.8148	0.8149	0.7977
HD91612	0.8152	0.8547	0.8195	0.8223	0.7920
HD100030	0.7975	0.8622	0.8189	0.8270	0.7847
HD92588	0.7998	0.9091	0.8292	0.8389	0.7983
HD97907	0.8153	0.9778	0.8452	0.8671	0.8024
HD104304	0.8018	0.9295	0.8135	0.8396	0.8119
HD107328	0.8142	0.9578	0.8248	0.8408	0.7948
HD134063	0.8038	0.8627	0.7985	0.8153	0.7826
HD129312	0.8215	0.8788	0.8248	0.8632	0.7898

Table 4.6: continued

Name	α	δ	Sp. Type	mv	(B − V)	$(B-V)_0$
NGC 6709 HSS 208	18 51 32	+10 19 09	A0	9.2	1.550	1.230
NGC 6709 HSS 303	18 51 10	+10 18 06	K0	9.1	1.310	0.990
IC 4665 42	17 45 14	+5 25 58	K5	10.6	1.400	1.240
IC 4665 54	17 45 51	+5 43 30	G7	10.4	1.400	1.240
IC 4665 74	17 46 41	+5 29 19	G8	10.2	1.500	1.340
IC 4665 MM 2	17 44 13	+5 15 02	K2	7.8	1.280	1.120
IC 4665 MM 4	17 44 47	+5 12 13	G7	9.7	1.270	1.110
IC 4665 MM 6	17 45 01	+5 50 01	K2	10.2	1.290	1.130
IC 4665 V 119	17 46 33	+5 17 39	A0	10.3	1.270	1.110
GEN +3.46650024	17 43 53	+5 33 17	A0	9.3	1.250	1.090
GEN +3.46650026	17 43 55	+5 27 23	K0	8.1	1.260	1.100
GEN +3.46650059	17 45 58	+5 07 05	?	11.0	1.390	1.230
NGC 6866 5	20 03 55	+44 08 24	?	11.6	1.000	0.870
NGC 6866 26	20 03 34	+44 02 32	K0	9.4	1.500	1.370
NGC 6633 41	18 26 23	+6 55 34	K2	9.1	1.200	1.030
NGC 6633 42	18 26 24	+6 40 51	K5	10.6	1.800	1.630
NGC 6633 121	18 28 20	+6 35 23	K0	10.7	1.230	1.060
NGC 6633 124	18 28 22	+6 21 02	?	10.3	1.500	1.330
NGC 6633 HILT 14	18 26 33	+6 31 34	F5	8.3	1.060	0.890
NGC 6633 HILT 56	18 27 05	+6 32 14	A2	8.2	0.820	0.650
NGC 6633 HILT 67	18 27 14	+7 00 33	K2	7.3	1.430	1.260
NGC 6633 HILT 116	18 27 54	+6 36 01	K2	8.3	1.090	0.920
NGC 6633 HILT 122	18 28 00	+6 54 51	K2	8.7	1.070	0.900
NGC 6633 HILT 140	18 28 22	+6 42 30	K0	8.8	1.040	0.870
NGC 6633 SAN 456	18 28 17	+6 45 59	K0	9.0	1.010	0.840

Table 4.7: We observed these stars in the clusters.

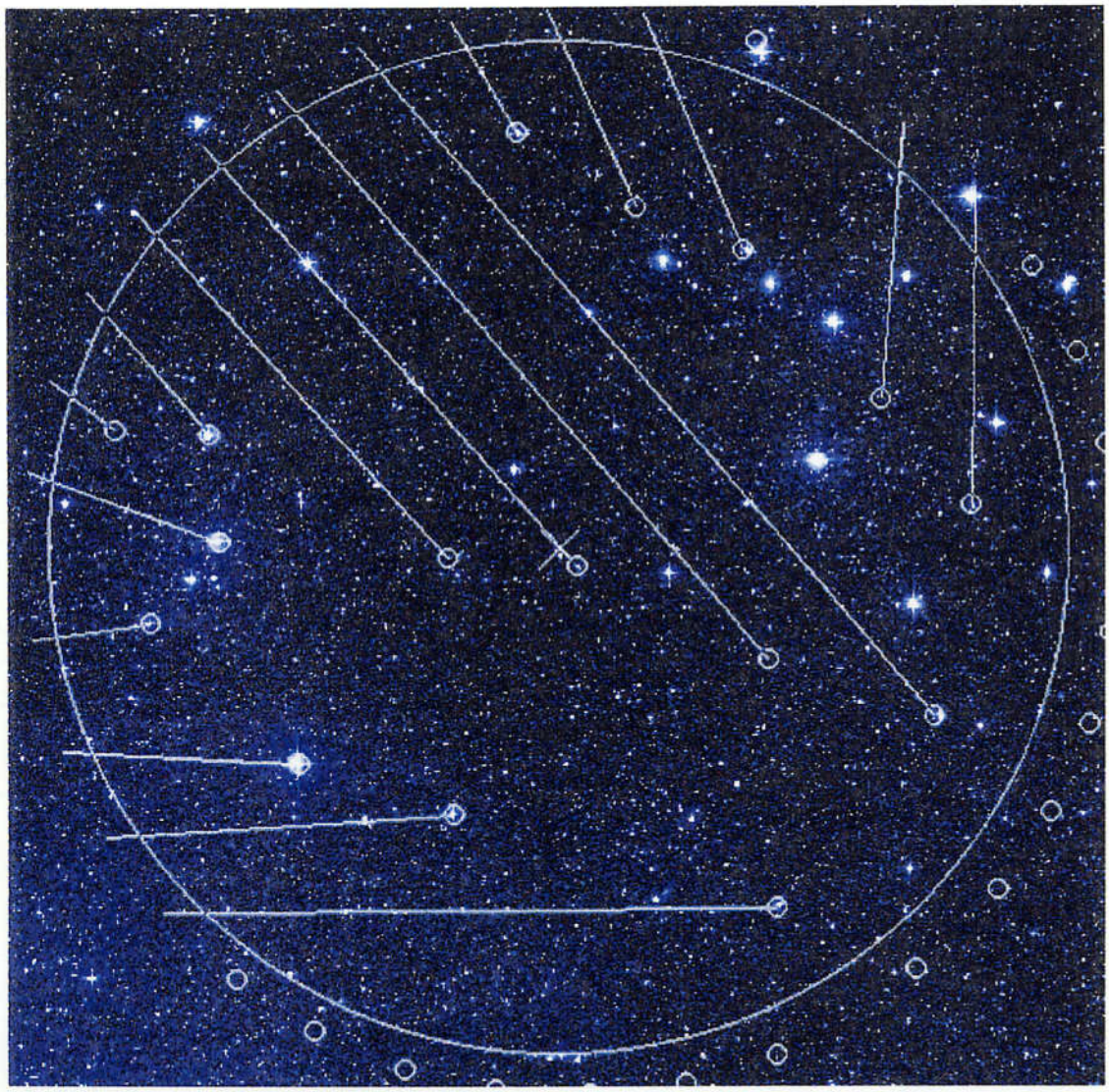

Figure 4.37: We observed the open cluster IC4665 with fiber probes arranged as this figure.

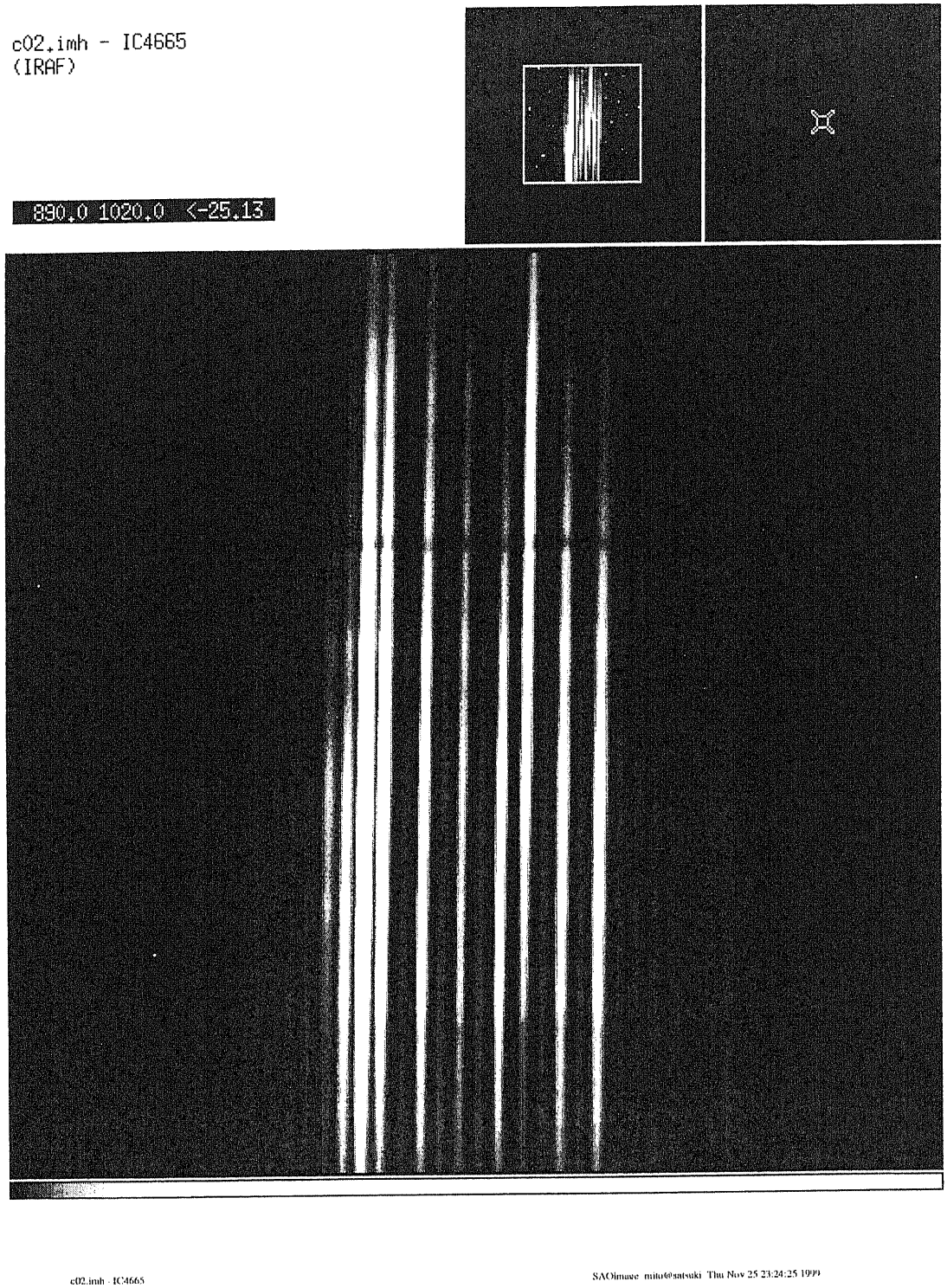

Figure 4.38: Raw spectra image of IC4665. Thirty apertures of the fibers line up horizontally and each spectrum is observed vertically. Above absorption line shows A band.

4.4 Reductions

4.4.1 Outline

a) First Reduction

We reduced our data using the IRAF package. After subtracting bias, all images were adjusted shifts of slit direction to flat field frame of each night. Adjustment of shift of dispersion direction is not performed at this point. This is performed lately at the step of the dispersion correction in *"dofibers"* task. The task adjusts the shift of object frames by interpolating linearly between comparison frames based on the Julian date.

b) Extraction of Spectra

After the first reduction, the data was reduced by *"dofibers"* task. This task is specialized for reducing multi-fiber spectra, extraction, flat fielding, fiber throughput correction, wavelength calibration, and sky subtraction. The default flat-fielding operation (*'fitflat=yes'*) is to be not introduce flat-field spectrum shape into object spectra. After this step, flux calibration was performed by using flux calibration stellar spectrum. However, we did not select default operation, because we could not obtain enough spectra of flux calibration star. Alternatively, we calibrated object spectra by using the flat-field spectrum(*'fitflat=no'*). In fact, since the metallicity indices are represented a ratio of the average flux centered on a feature with that of two continuum bands on either side, only the negligible error was produced by this choice. Finally, we obtained spectra with one pixel width.

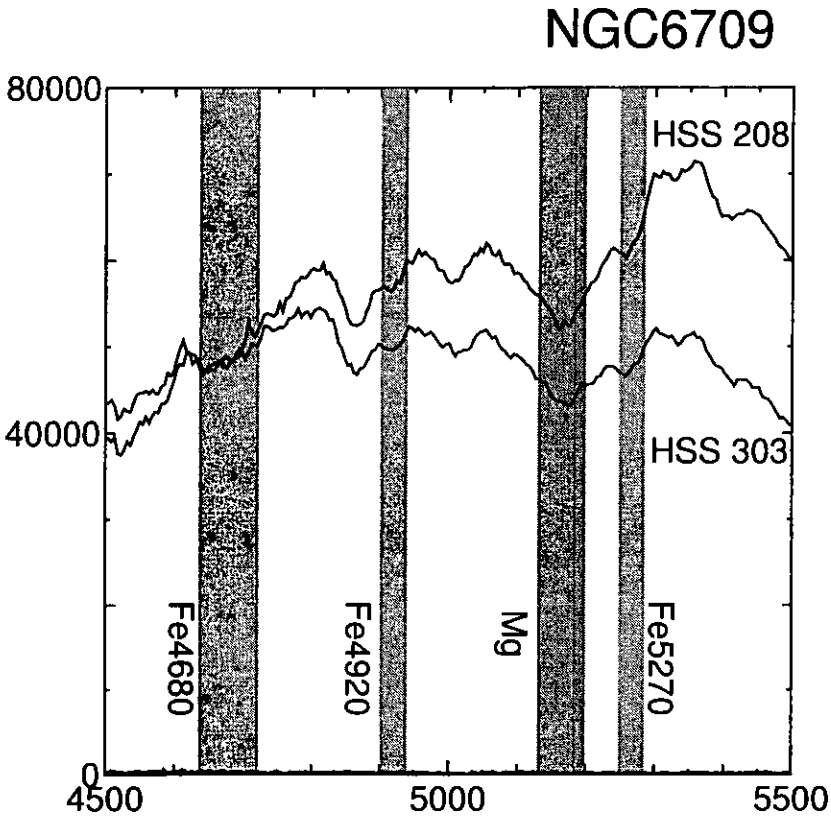

Figure 4.39: We confirmed the regions absorbed by metals in our spectra. Gray rectangles show the regions of the metallicity indices defined by Friel(1987)

c) Calculation of Friel Indices

Figure 4.39 is the spectra of NGC6709 showing four absorption bands, Fe4680, Fe4920, Mg, and Fe5270.

We used the task *bplot* to obtain the indices defined by Friel which computes the mean, RMS, and signal-to-noise ratio over a region. And metallicity indices were calculated following Friel definition. Figure 4.40 shows the regions used for calculation of the metallicity index Fe4920.

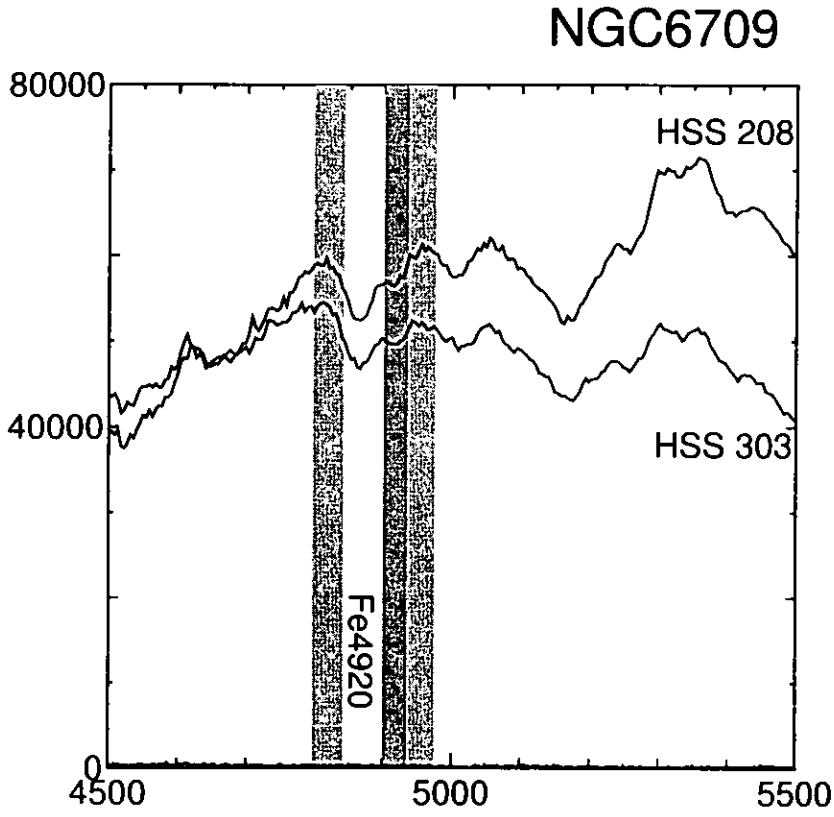

Figure 4.40: Central darker rectangle shows the region absorbed by Fe4920 and side dark rectangles do the ones of pseudo continuum.

4.4.2 Field Stars

a) Calibration of Our Indices

To calibrate our indices to Friel indices, we used the spectra of sixteen field stars. The spectra are shown in Figure 4.41 - 4.56. We could not observe the region of short wavelength about ten stars from the first due to the mechanical troubles in the beginning of the observation. Table 4.8 and 4.9 show the indices obtained with the observation. Ten stars lack eight bluer indices. Figure 4.57 - 4.71 show the correlation between our indices and Friel's. Table 4.10 shows the details of the regression lines. In the bar chart 4.72, all correlation coefficients are shown. White bars in the chart mean indices that Friel did not use to obtain metallicities after all. We see that Mg and Fe4680 indices agree well with Friel's ones, and Fe4530, Fe4065, Fe5270, and Fe4920 almost agree.

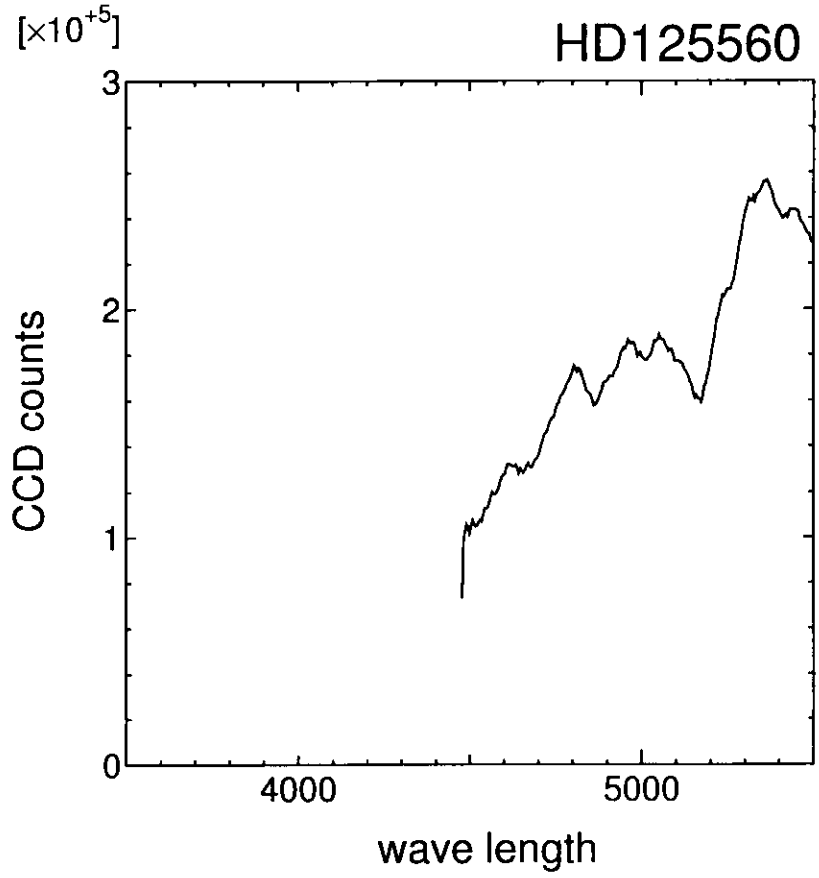

Figure 4.41: the spectrum of the field stars for index calibration

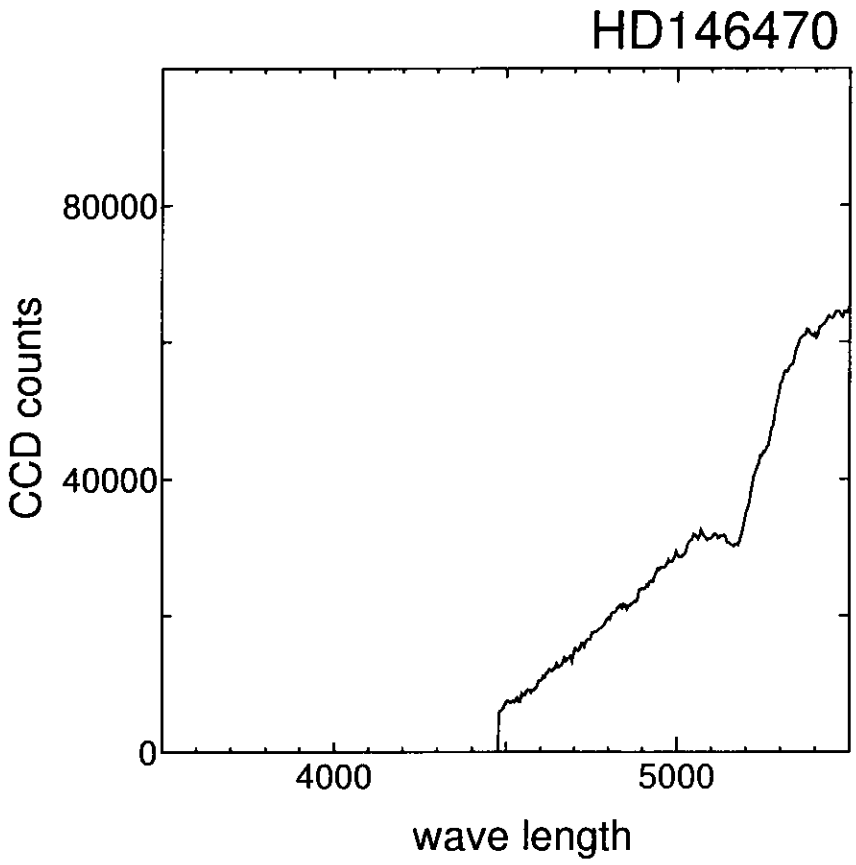

Figure 4.42: continued

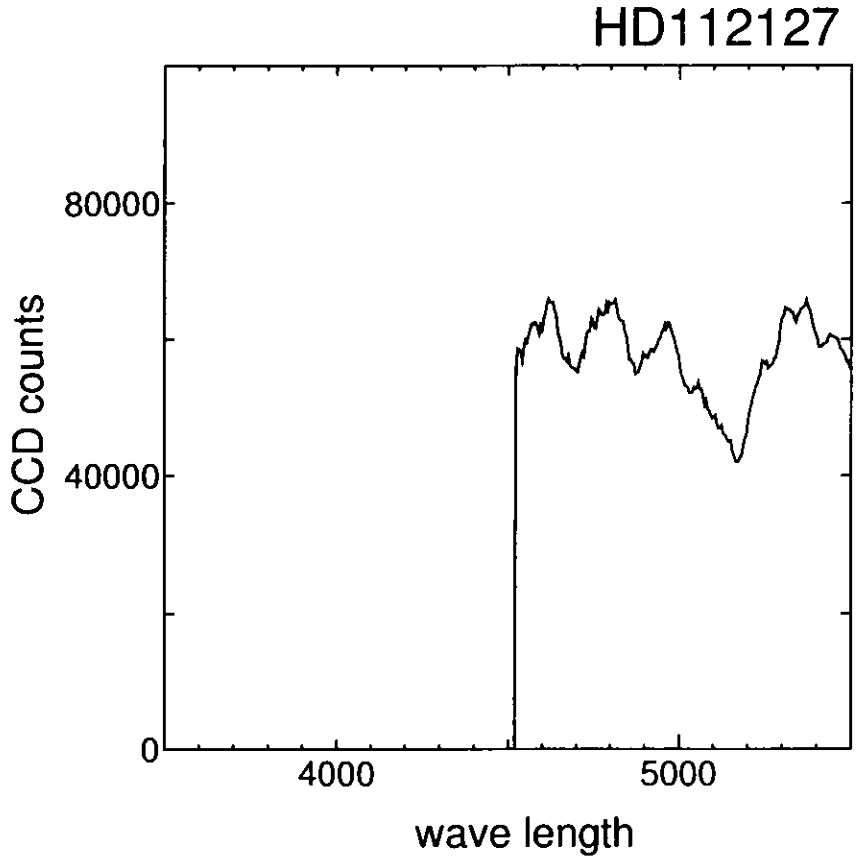

Figure 4.43: continued

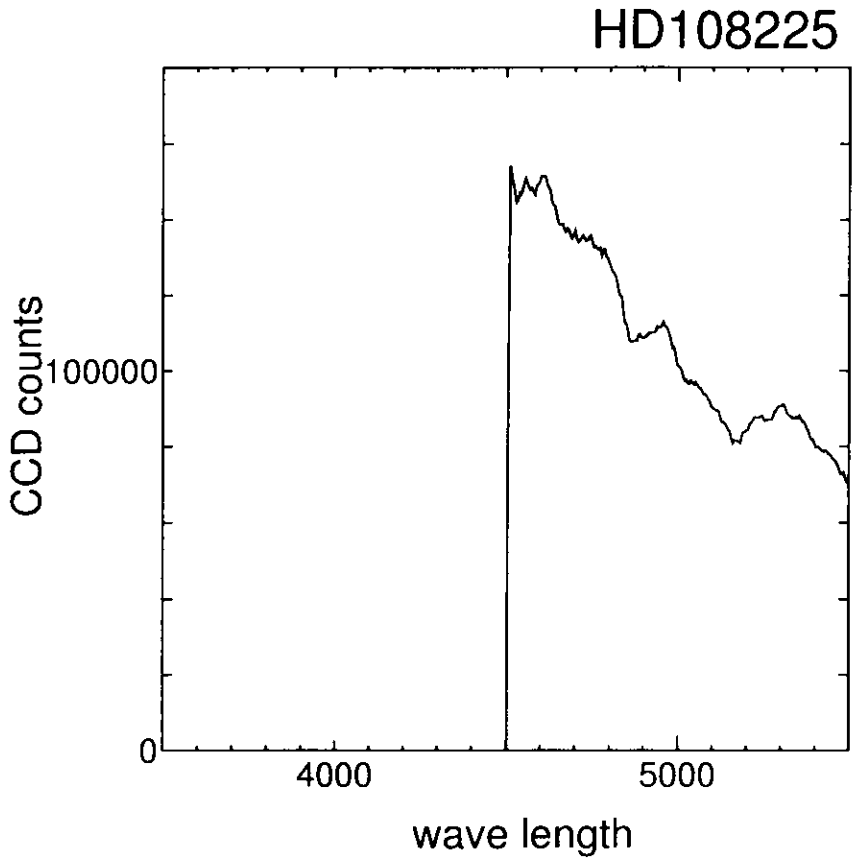

Figure 4.44: continued

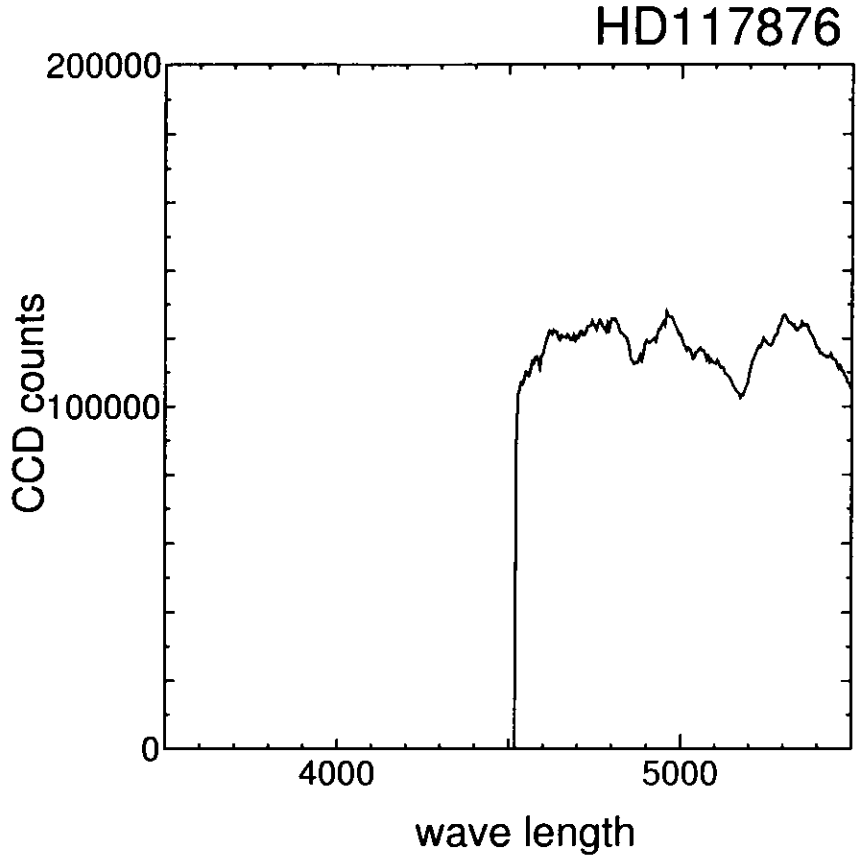

Figure 4.45: continued

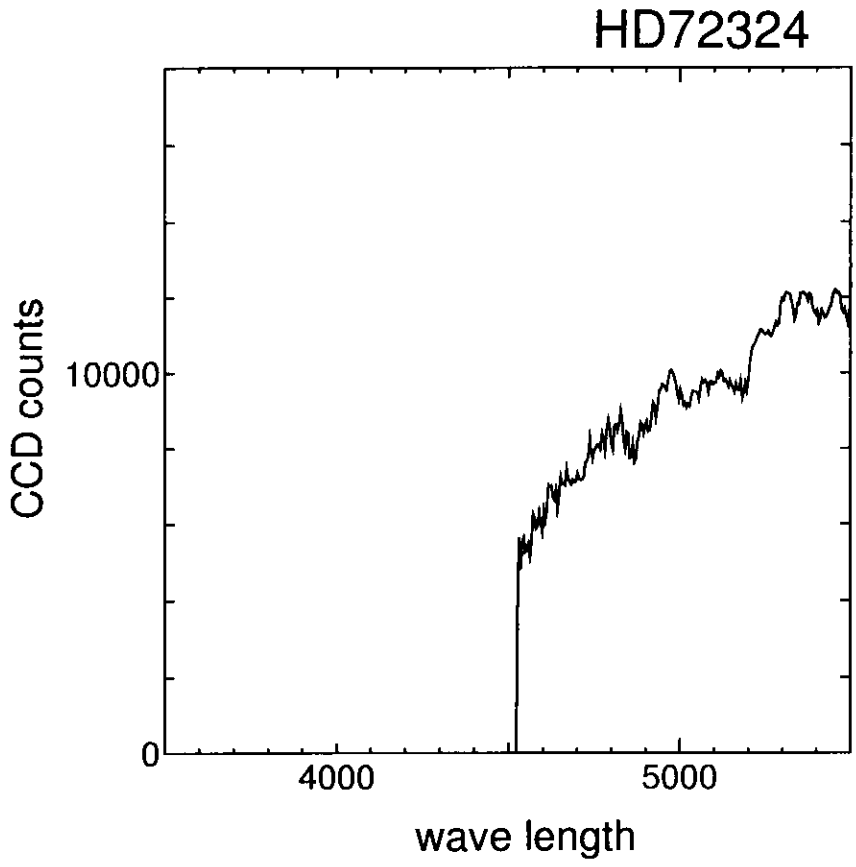

Figure 4.46: continued

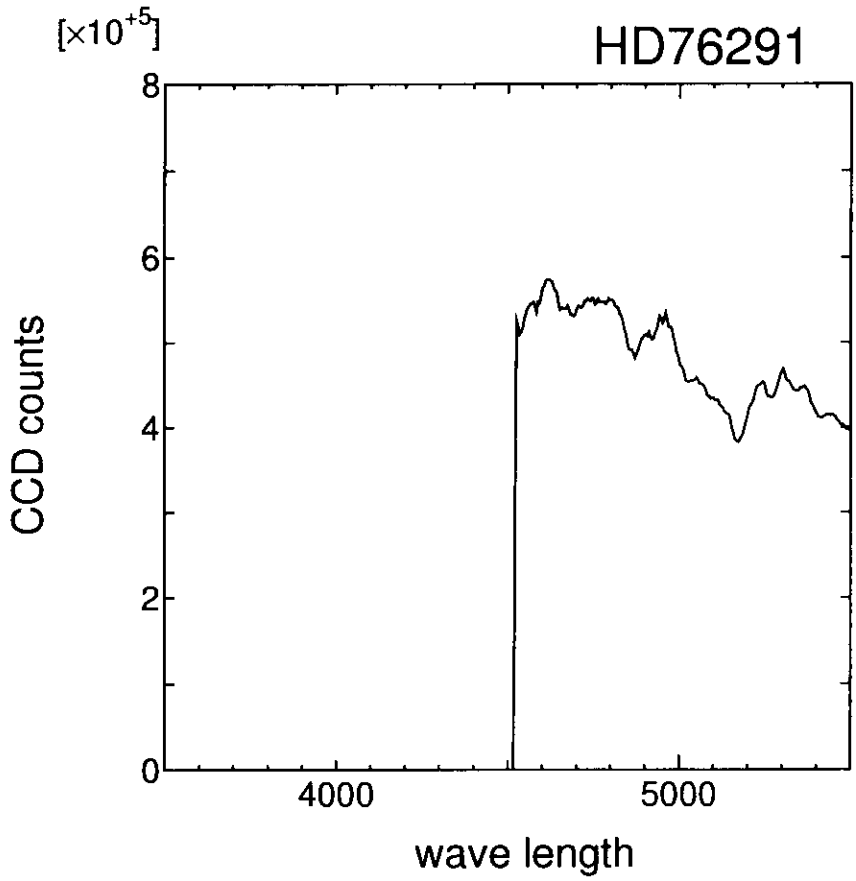

Figure 4.47: continued

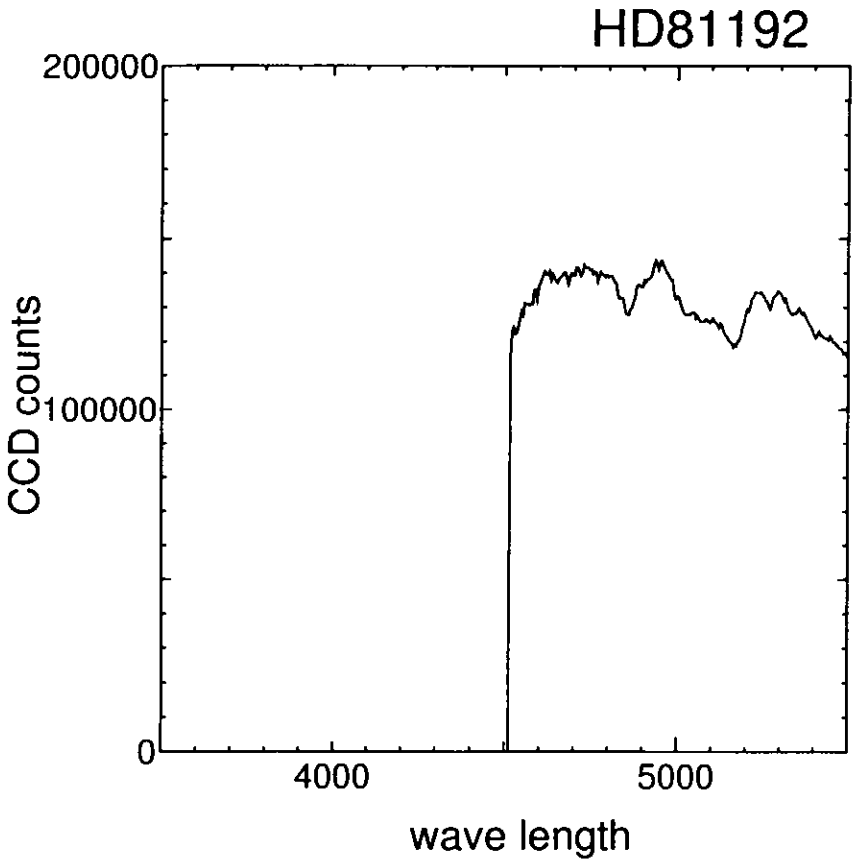

Figure 4.48: continued

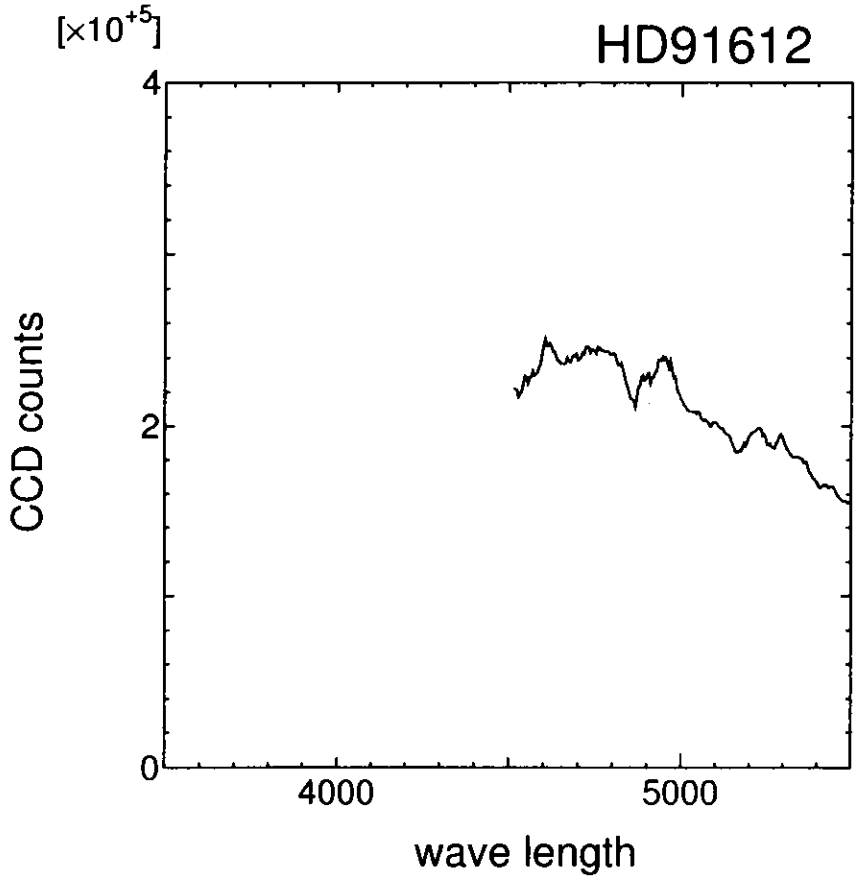

Figure 4.49: continued

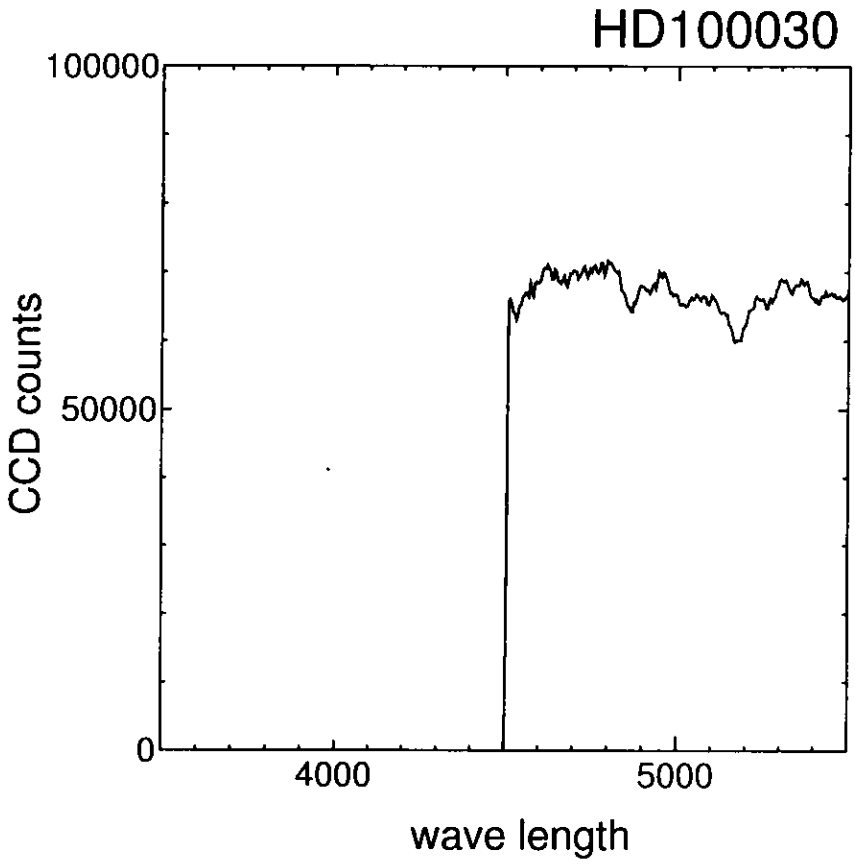

Figure 4.50: continued

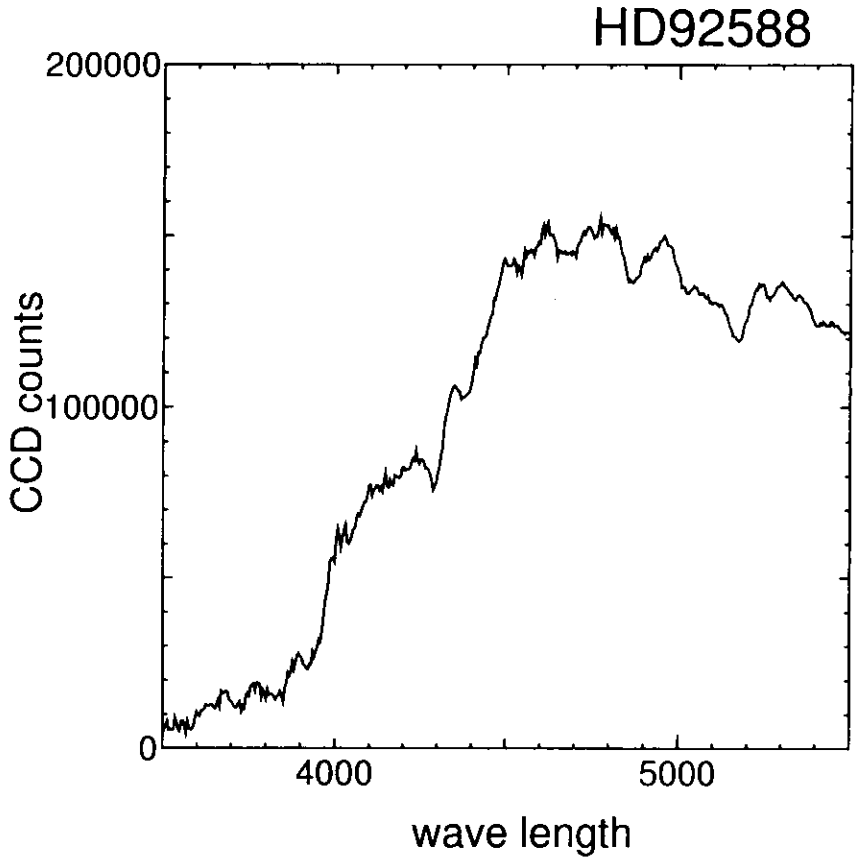

Figure 4.51: continued

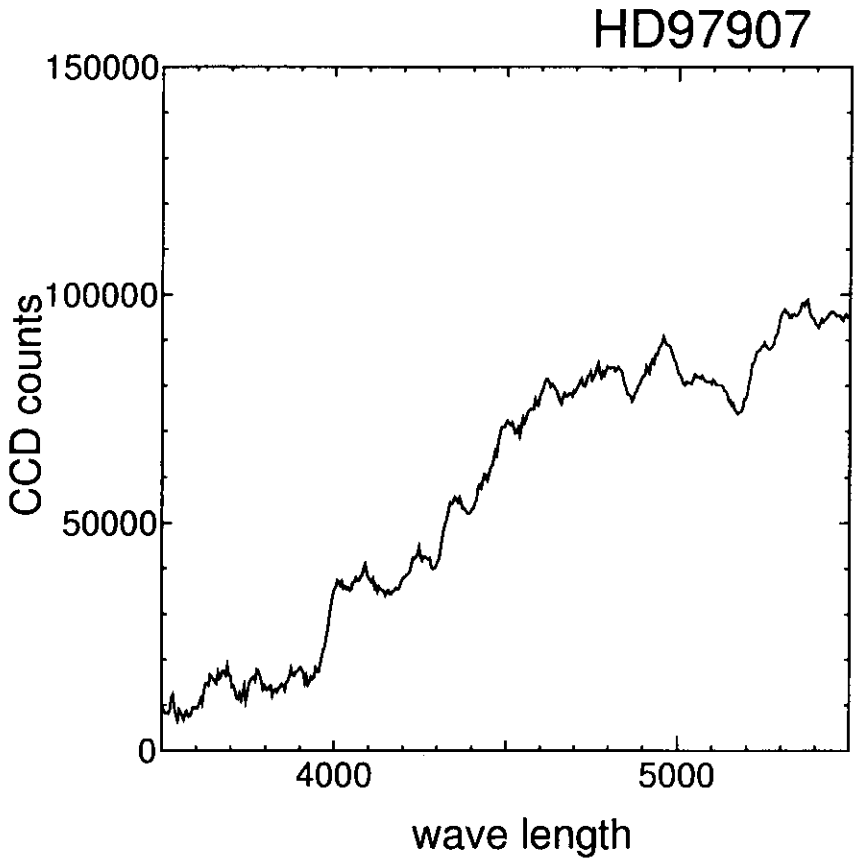

Figure 4.52: continued

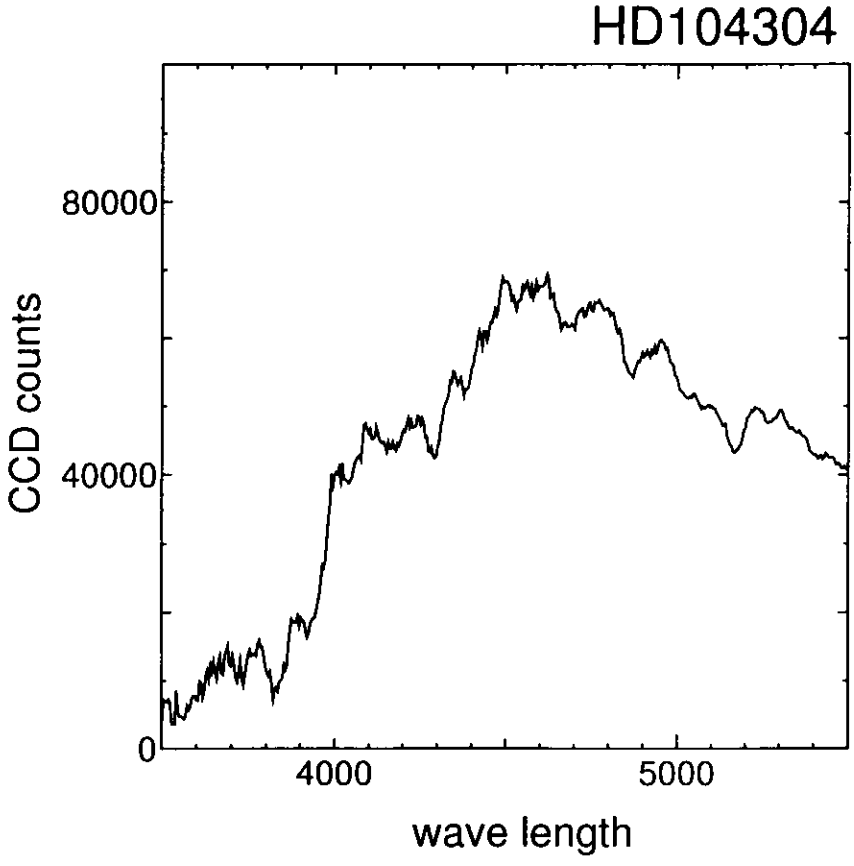

Figure 4.53: continued

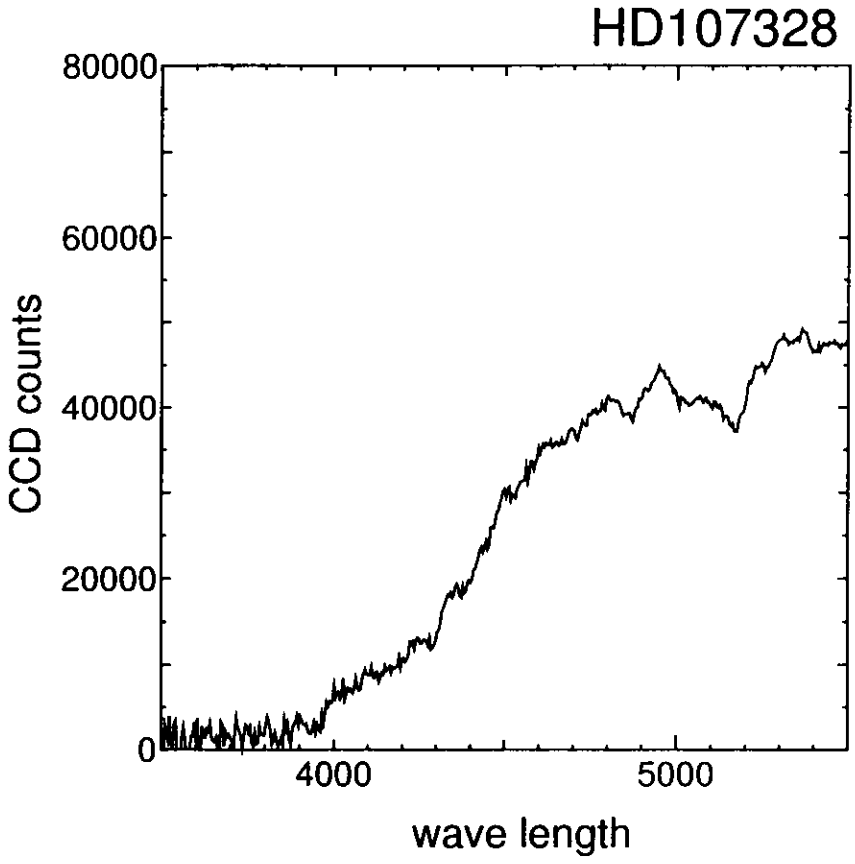

Figure 4.54: continued

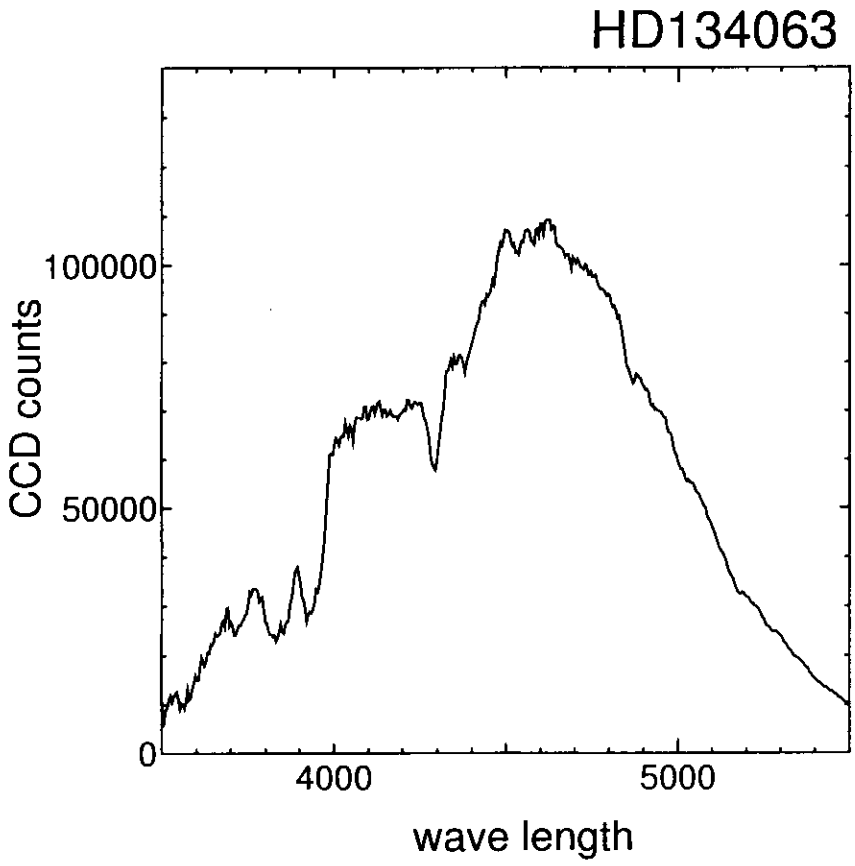

Figure 4.55: continued

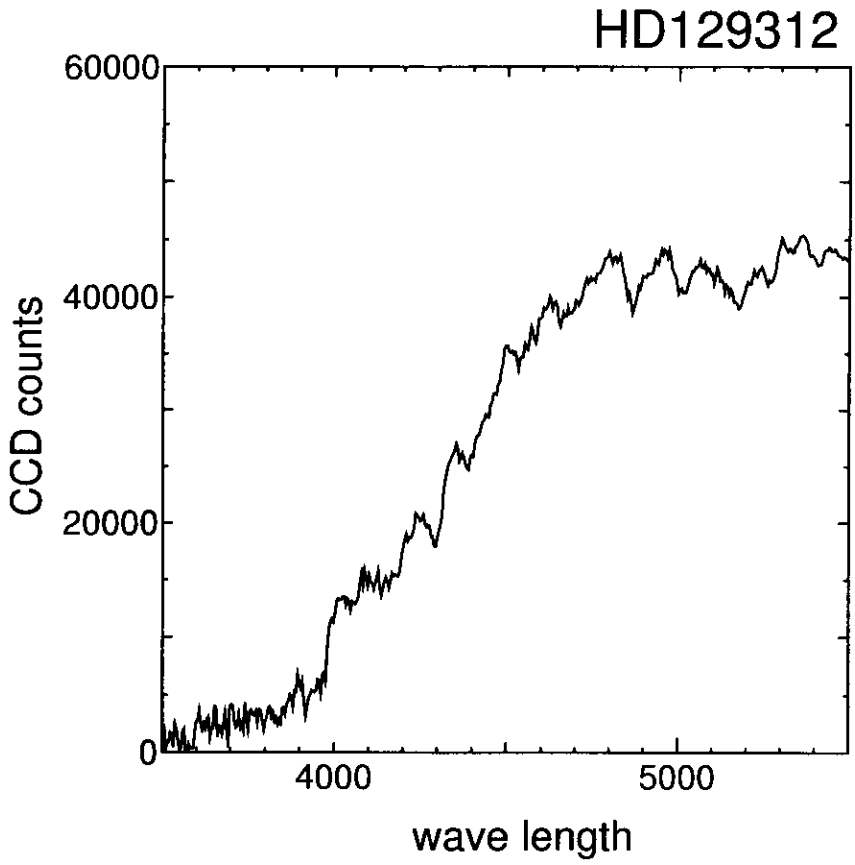

Figure 4.56: continued

Name	Mg3838	CN3883	CaII	Fe4065	CN4216	Ca4226	G-Band	Fe4530
HD125560								
HD146470								
HD112127								
HD108225								
HD117876								
HD72324								
HD76291								
HD81192								
HD91612								
HD100030								
HD92588	0.2619	1.4998	0.9261	0.7991	0.8301	0.7562	1.0145	0.7814
HD97907	0.0902	1.2527	0.9572	0.7560	0.8317	0.9079	0.9362	0.8114
HD104304	0.0737	1.3640	0.8553	0.7924	0.7843	0.7994	0.9478	0.7704
HD107328	0.1659	1.6192	0.9741	0.7642	0.8332	0.8663	1.0043	0.8055
HD134063	0.1119	1.2682	0.9081	0.7588	0.7983	0.7206	1.0334	0.7940
HD129312	0.1956	1.4498	1.0017	0.7969	0.7891	0.9030	0.9413	0.8105

Table 4.8: our indices of calibration stars

Name	Fe4680	Fe4920	Fe5011	Mg	Fe5270	Fe5335	Fe5400
HD125560	0.8258	0.7645	0.7630	1.0403	0.7804	0.7548	0.7817
HD146470	0.7998	0.6901	0.7353	1.0687	0.7728	0.7506	0.7595
HD112127	0.8632	0.8047	0.7847	1.1246	0.7884	0.7690	0.8023
HD108225	0.7752	0.8072	0.7797	0.9435	0.7595	0.7544	0.7779
HD117876	0.7696	0.7786	0.7681	0.9264	0.7666	0.7590	0.7770
HD72324	0.7792	0.7412	0.7956	0.8738	0.7826	0.7691	0.7956
HD76291	0.7862	0.7781	0.7874	0.9591	0.7807	0.7639	0.7887
HD81192	0.7574	0.7552	0.7730	0.8697	0.7610	0.7634	0.7726
HD91612	0.7782	0.7699	0.7781	0.8508	0.7743	0.7582	0.7816
HD100030	0.7653	0.7803	0.7790	0.8659	0.7743	0.7661	0.7750
HD92588	0.7898	0.7816	0.7722	0.8936	0.7659	0.7557	0.7797
HD97907	0.7929	0.7727	0.7805	0.9560	0.7800	0.7686	0.7817
HD104304	0.8059	0.8011	0.7796	0.9225	0.7727	0.7584	0.7860
HD107328	0.7817	0.7496	0.7839	0.9385	0.7715	0.7657	0.7792
HD134063	0.7578	0.8145	0.7666	0.8896	0.7710	0.7558	0.7981
HD129312	0.7953	0.7777	0.7946	0.8544	0.7894	0.7632	0.7856

Table 4.9: continued

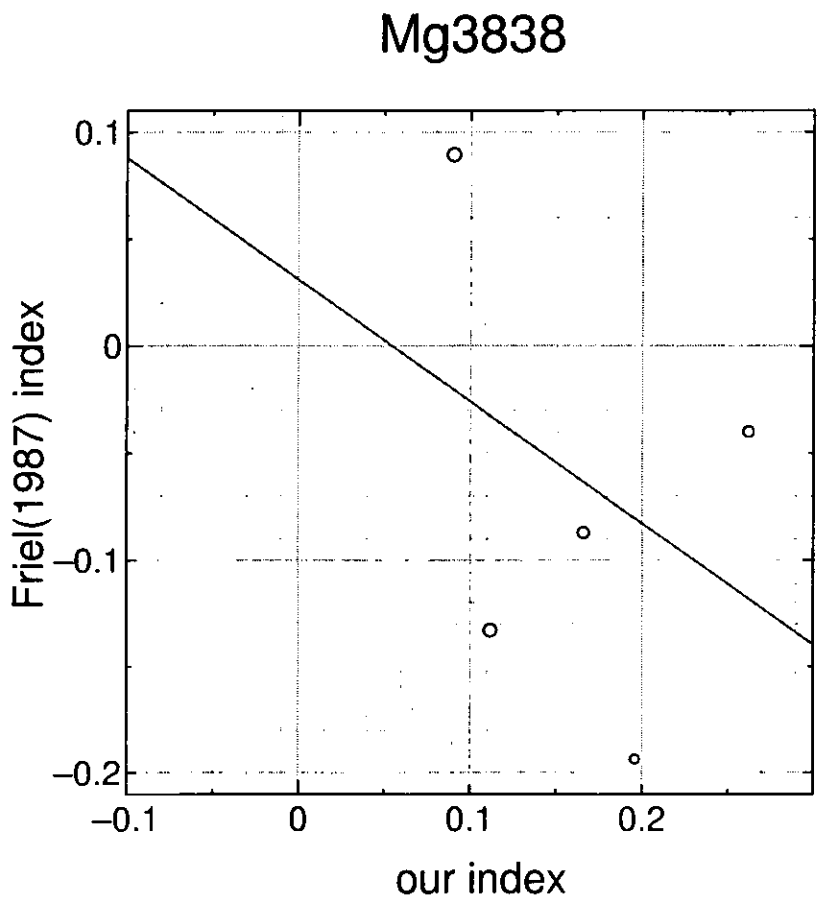

Figure 4.57: Index correlation between our indices and Friel's. Radii of the circles are in proportion to S/N of the spectrum.

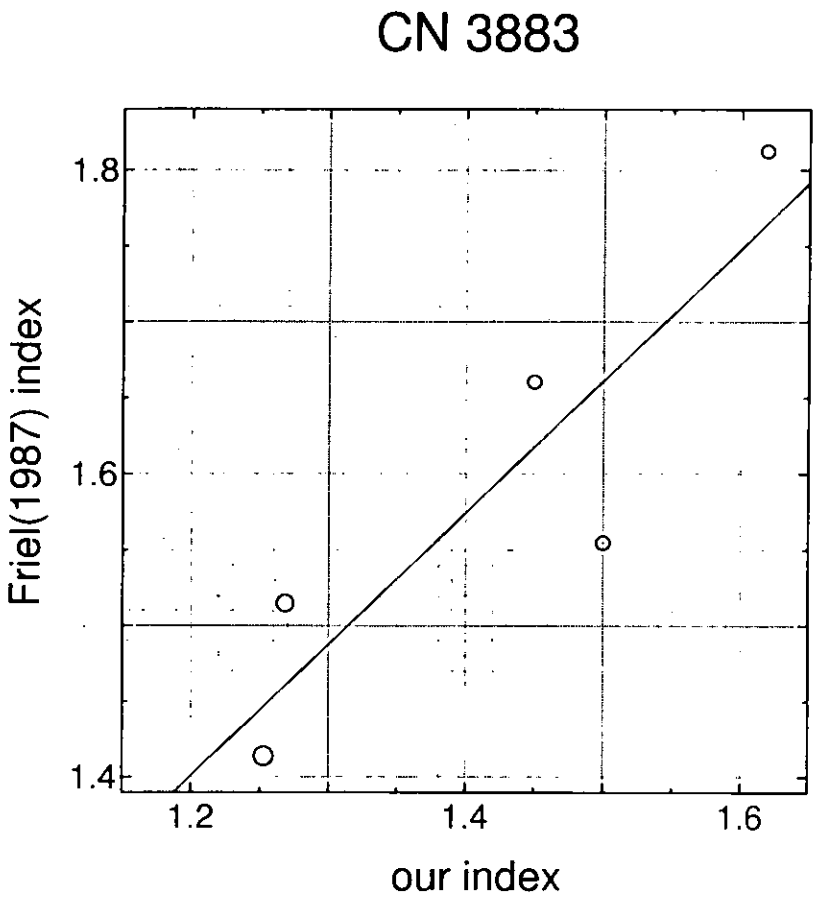

Figure 4.58: continued

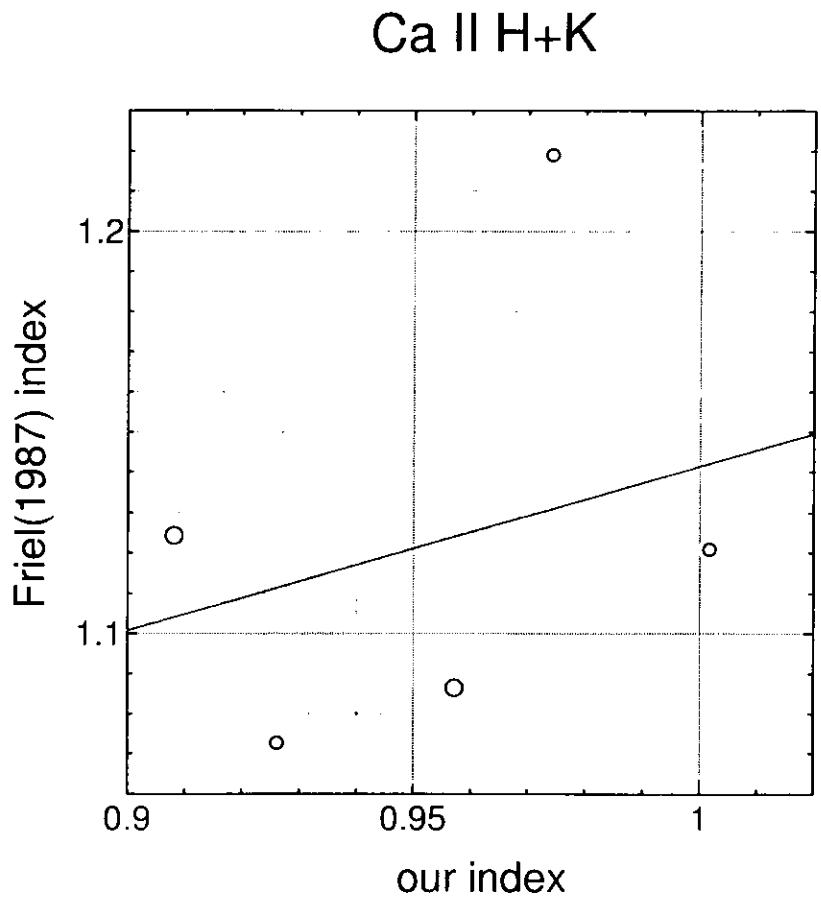

Figure 4.59: continued

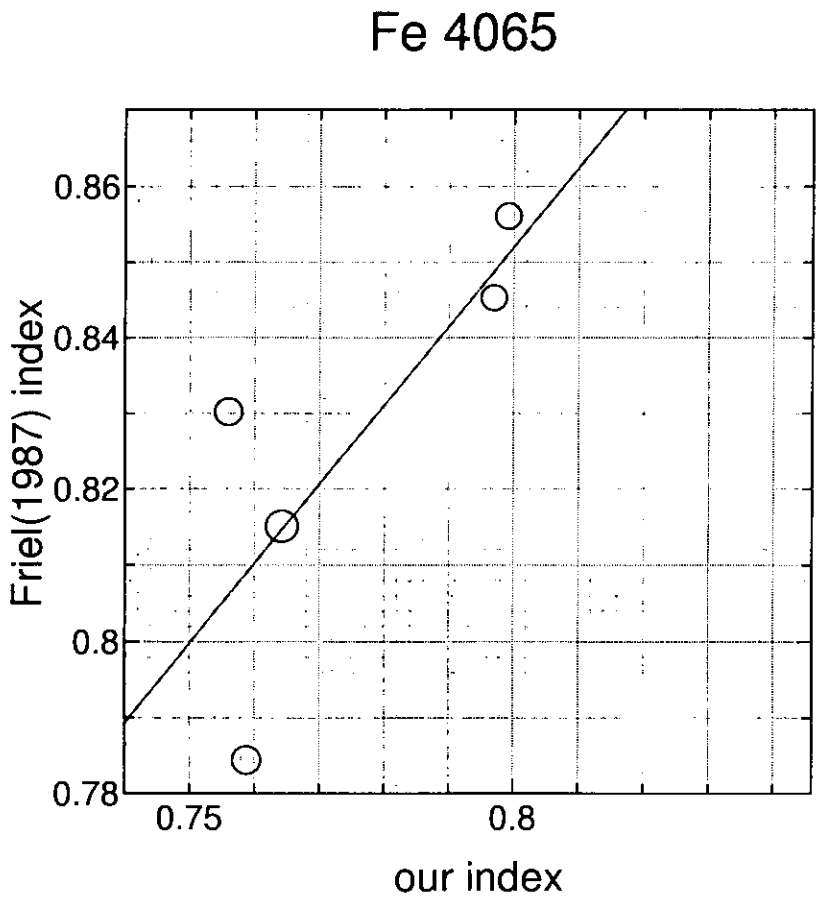

Figure 4.60: continued

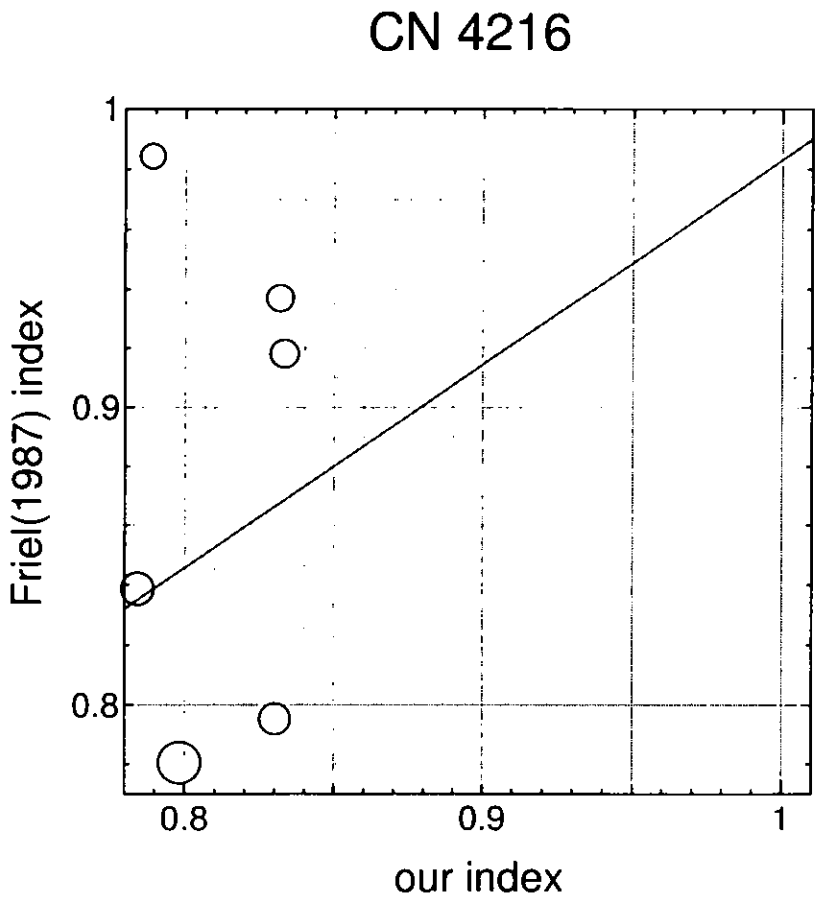

Figure 4.61: continued

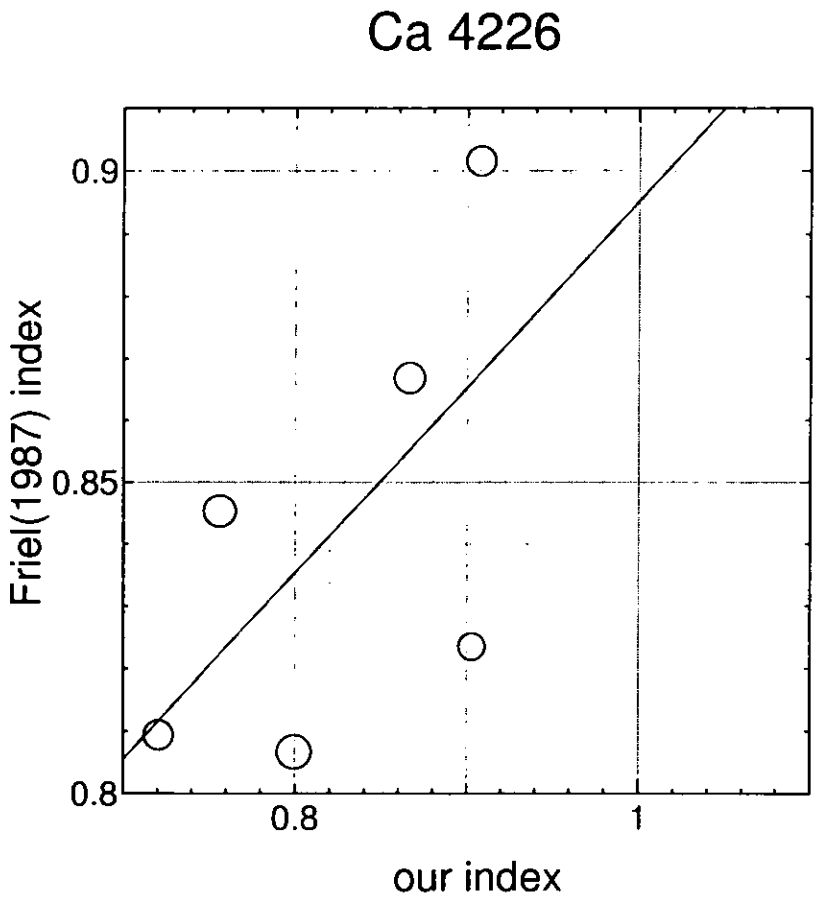

Figure 4.62: continued

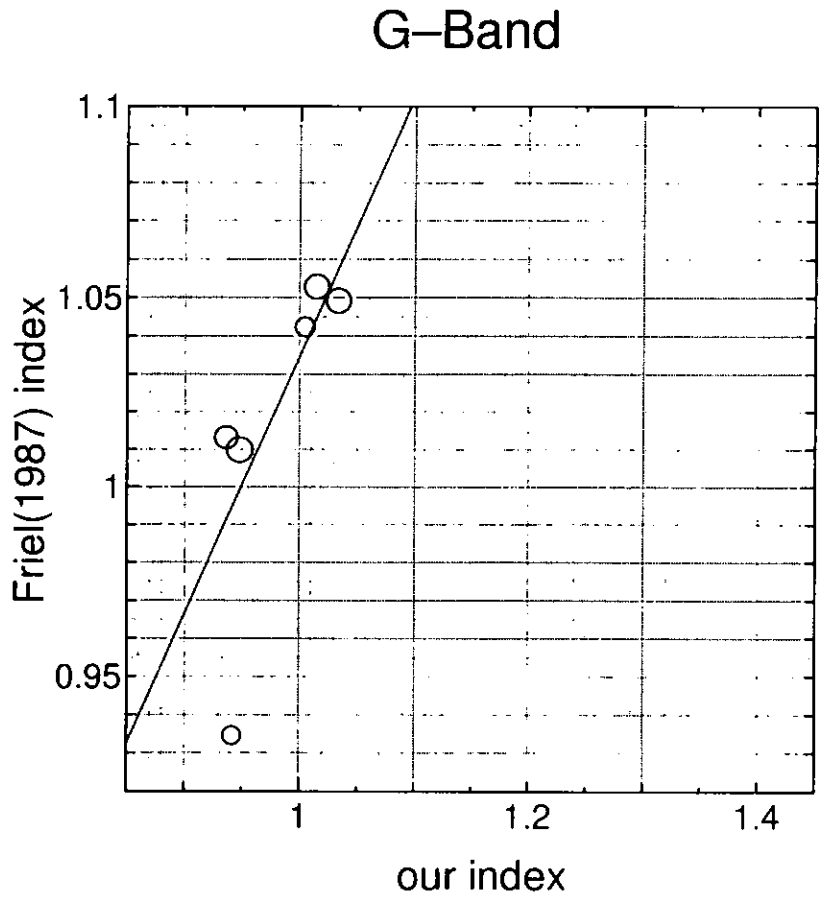

Figure 4.63: continued

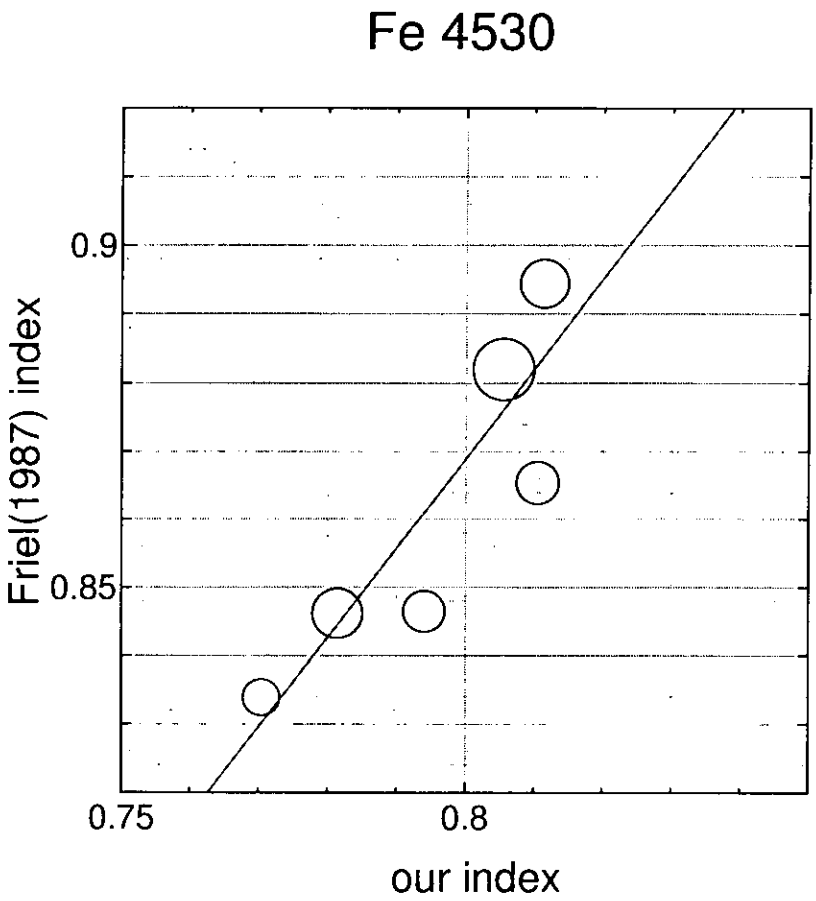

Figure 4.64: continued

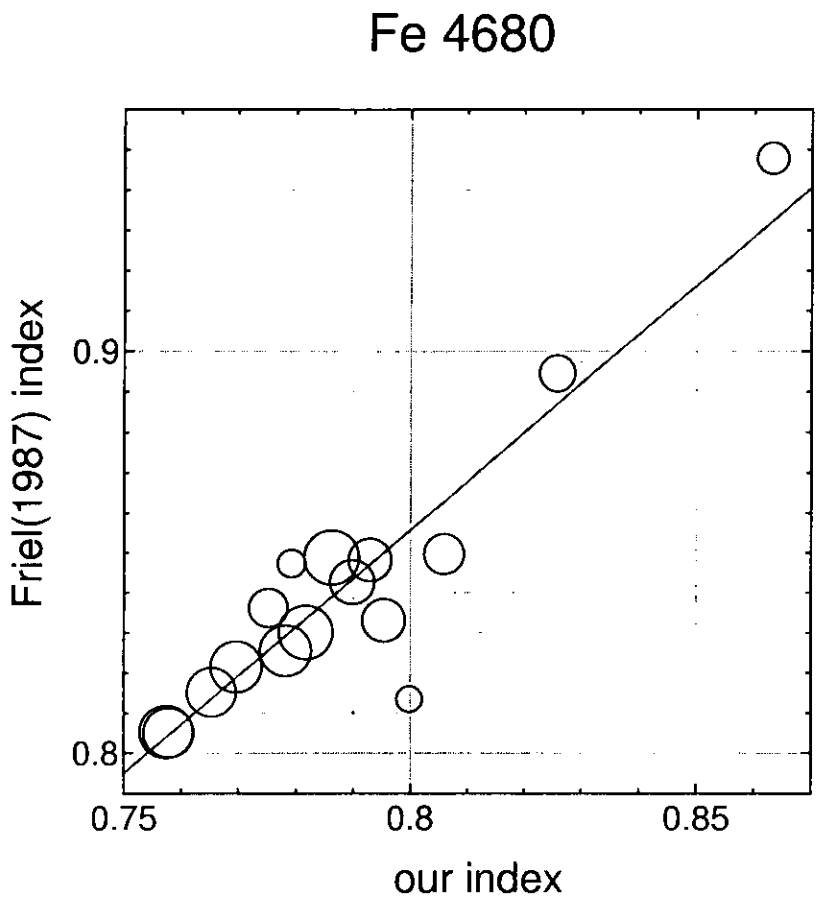

Figure 4.65: continued

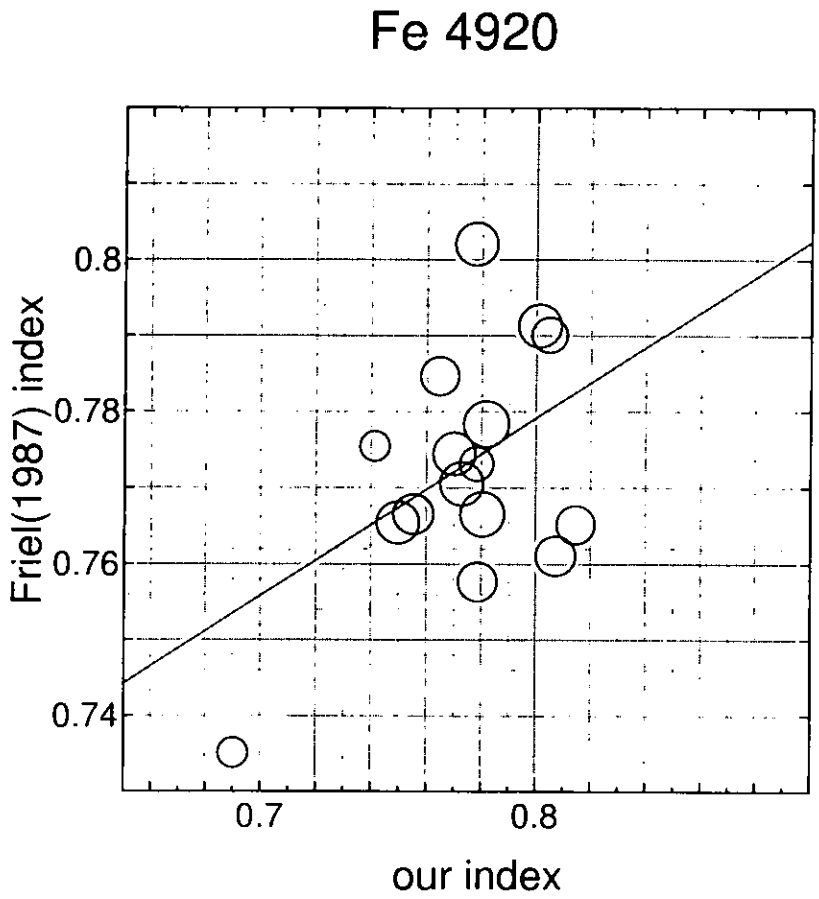

Figure 4.66: continued

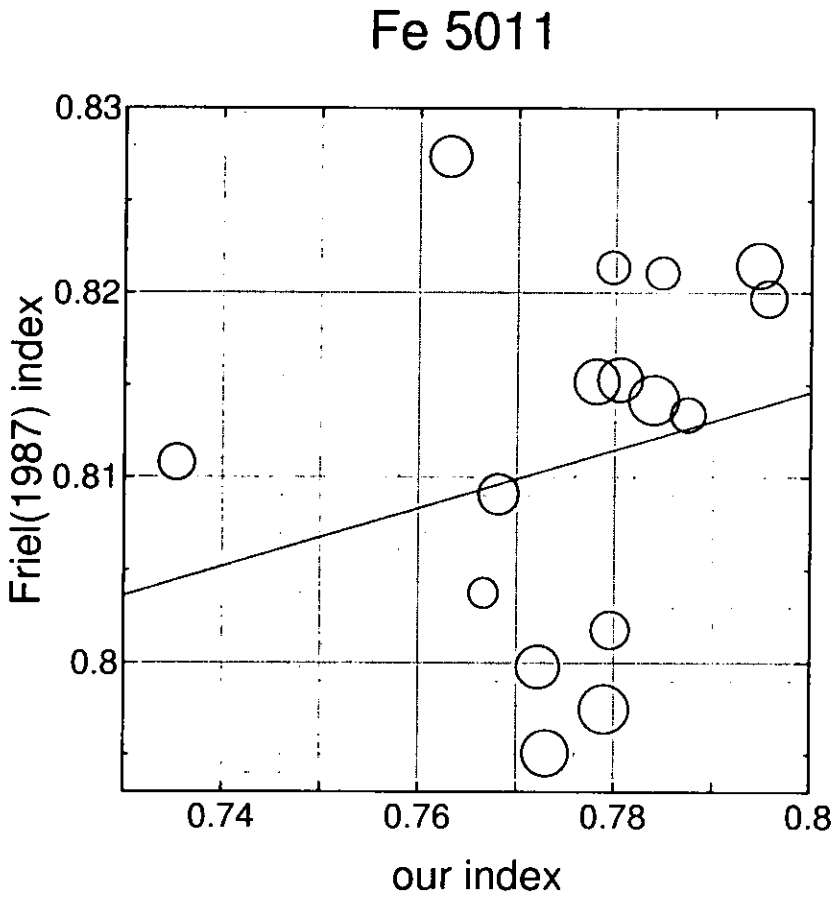

Figure 4.67: continued

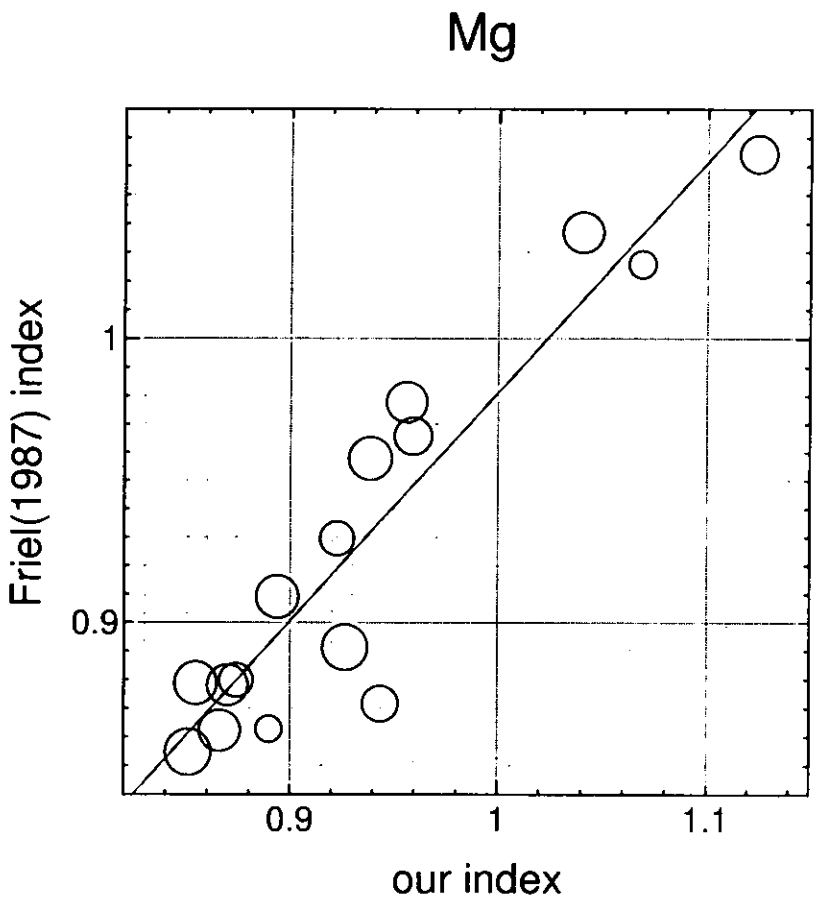

Figure 4.68: continued

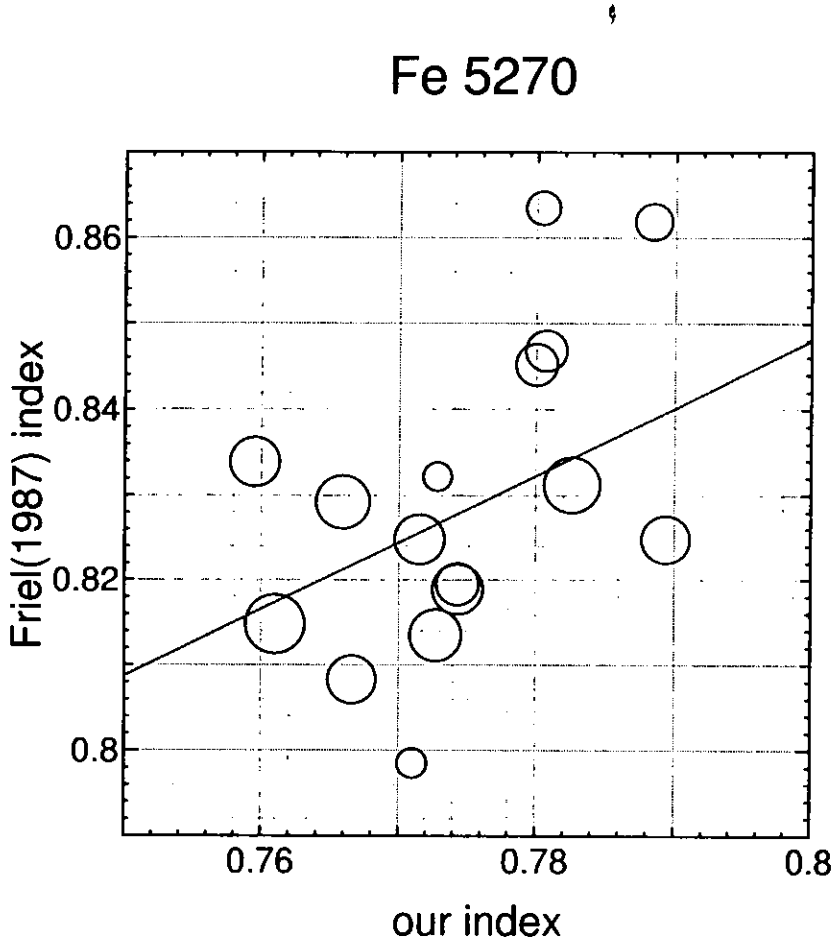

Figure 4.69: continued

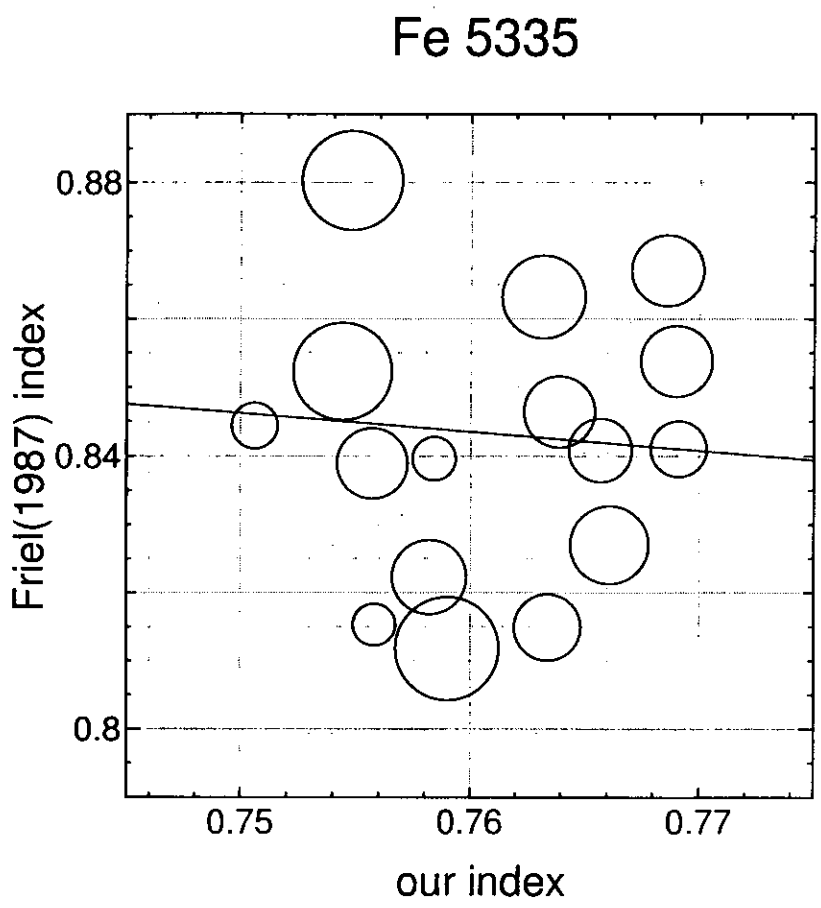

Figure 4.70: continued

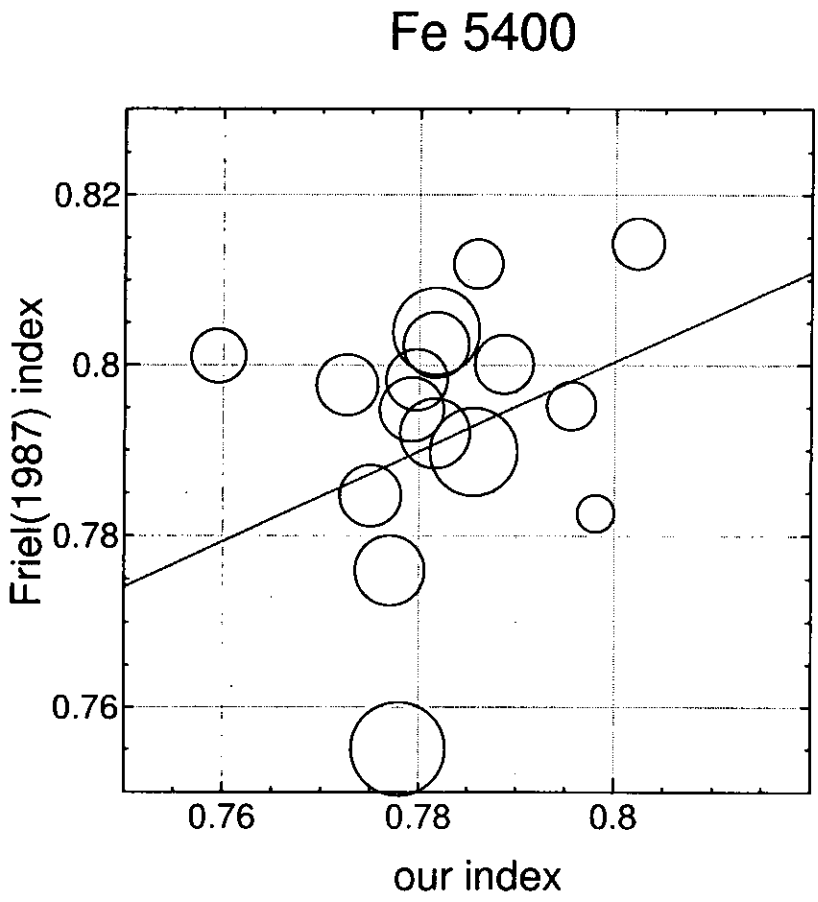

Figure 4.71: continued

	$y = ax + b$	
Index	a	b
Mg3838	−0.5692	0.0310
CN3883	0.8682	0.3592
CaII H+K	0.4063	0.7351
Fe4065	1.0445	0.0165
CN4216	0.6874	0.2958
Ca4226	0.2990	0.5962
G-Band	0.6816	0.3532
Fe4530	1.3108	−0.1797
Fe4680	1.2135	−0.1151
Fe4920	0.2331	0.5927
Fe5011	0.1569	0.6891
Mg	0.8042	0.1770
Fe5270	0.7859	0.2193
Fe5335	−0.2719	1.0501
Fe5400	0.5260	0.3796

Table 4.10: Details of the regression lines. x :our indices. y :Friel's indices.

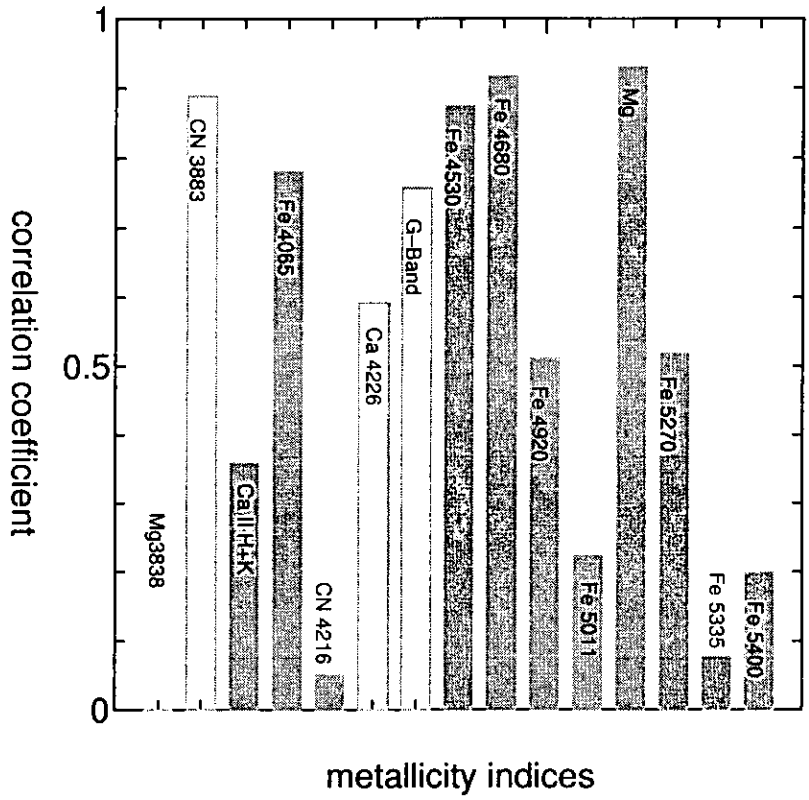

Figure 4.72: correlation coefficients between our indices and Friel's

b) Index Selections for Metallicity Determination

As discussed extensively by Friel & Janes (1993) [5], the Mg index for the cluster stars showed unexpected systematic variation. The difference between metallicities determined with Mg index and those done with Fe indices became increasingly negative with decreasing cluster age. The magnitude of the effect was large: in clusters with ages of less than 2 to 3 billion years, Mg indicated abundances some 0.5 dex more metal poor than those from Fe indices. This effect has been recently confirmed in an expanded sample with additional younger clusters by Thogersen *et al.*(1993) [18]. Consequently, we did not use Mg index to obtain the metallicities of open clusters. Finally, we determined to obtain the metallicities

by using three Fe indices, Fe4680, Fe4920, and Fe5270.

Friel defined the lines of constant metallicity on diagrams of $(B-V)_0$ and magnitudes of indices. We can see the relation between Fe4680, Fe5270 and Mg indices and metallicity in her paper(1987). Figure 4.73, 4.74, and 4.75 show the diagrams. However, Friel did not make the relation between Fe4920 index and metallicity clear in it. Therefore, we defined the lines of constant metallicity about Fe4920 index by using the method of least squares with respect to Friel's data of standard stars. Figure 4.76 shows the diagram.

The metallicities of each stars were obtained as an weighted average of metallicities of each indices. The weights optimized to three Fe indices were obtained by using 54 stars observed by Friel. Table 4.11 shows the weight. Figure 4.77 shows the correlation between the metallicities obtained by three indices (Fe4680, Fe4920 and Fe5270) and those by high dispersion spectroscopy (standard). The rms deviation is 0.16 dex and we can see that the three indices used here predict metallicities well.

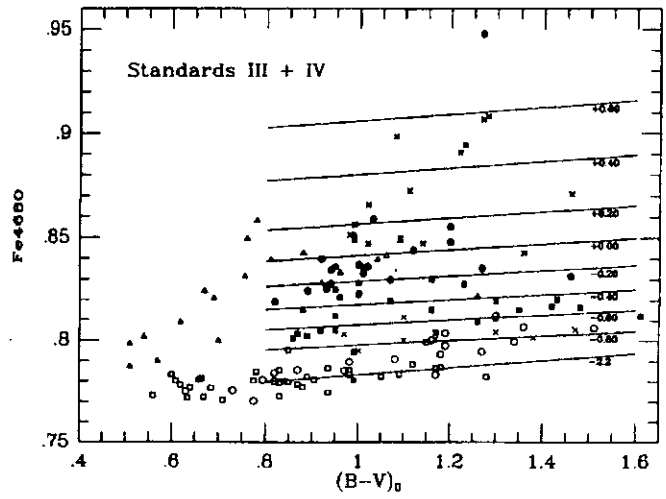

Figure 4.73: Fe4680 index versus $(B - V)_0$ for standard evolved stars of luminosity classes III and IV. Lines of constant metallicity are indicated (Friel 1987).

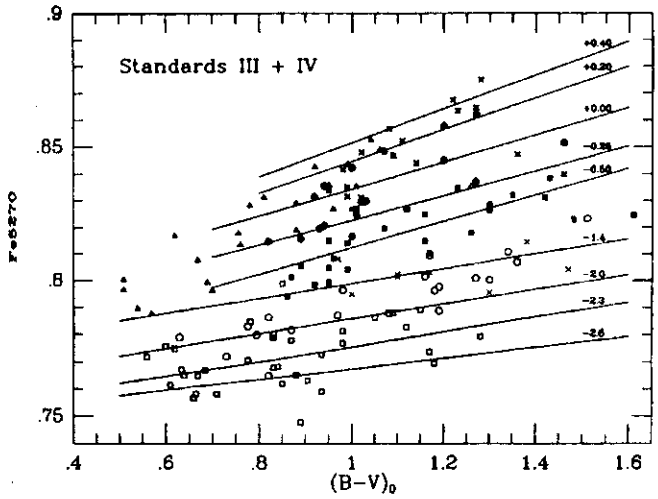

Figure 4.74: Fe5270 index versus $(B - V)_0$ for standard evolved stars of luminosity classes III and IV. Lines of constant metallicity are indicated (Friel 1987).

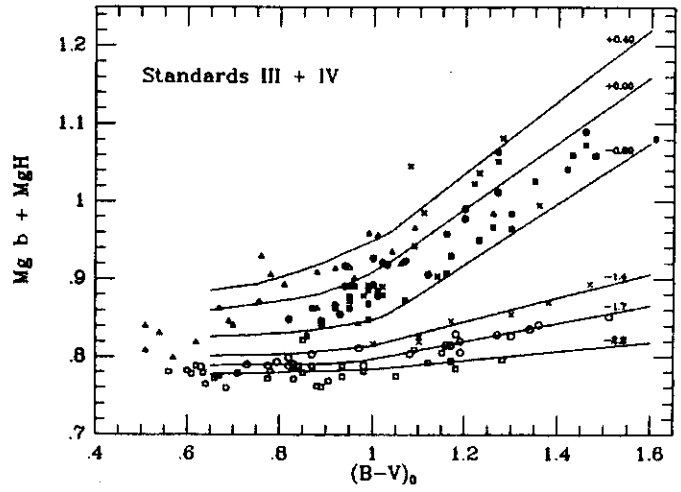

Figure 4.75: Mg index versus $(B - V)_0$ for standard evolved stars of luminosity classes III and IV. Lines of constant metallicity are indicated (Friel 1987).

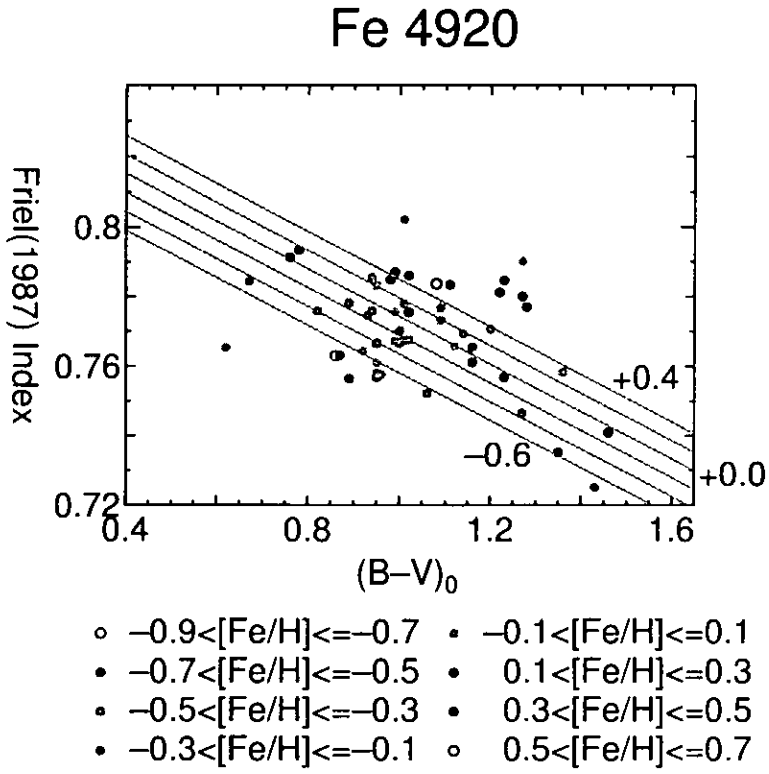

Figure 4.76: Fe4920 index versus $(B-V)_0$ for standard evolved stars of luminosity classes III and IV (Friel 1987). we defined the lines of constant metallicity by using the method of least squares.

	$y = ax_1 + bx_2 + cx_3$		
criteria	a	b	c
$0.0 \leq x_1, -0.5 < x_3$	0.700	0	0.312
$0.0 \leq x_1, x_3 \leq -0.5$	0.821	0.051	0.128
$x_1 < 0.0, -0.5 < x_3$	0.364	0.062	0.609
$x_1 < 0.0, x_3 \leq -0.5$	0.600	0.074	0.196

Table 4.11: weight definition. y : [Fe/H], x_1 : $[\mathrm{Fe/H}]_{\mathrm{Fe4680}}$, x_2 : $[\mathrm{Fe/H}]_{\mathrm{Fe4920}}$, x_3 : $[\mathrm{Fe/H}]_{\mathrm{Fe5270}}$

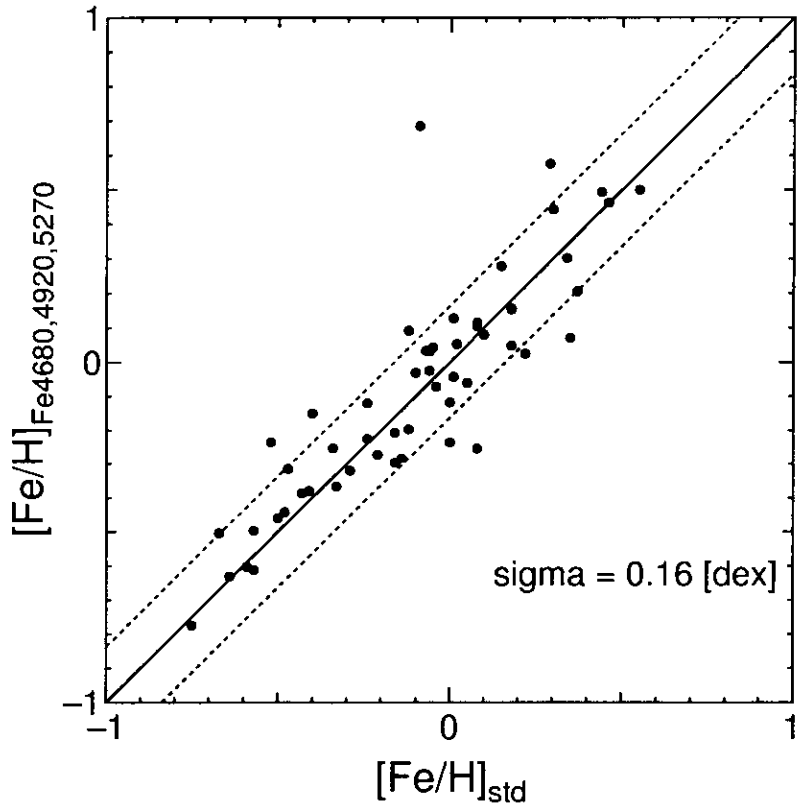

Figure 4.77: The correlation between the metallicities obtained by three indices (Fe4680, Fe4920 and Fe5270) and those by high dispersion spectroscopy (standard)

4.4.3 Open Clusters

a) Metallicity Calculation of Open Clusters

Figure 4.78 - 4.104 show the spectra of the stars in the clusters. In the figures, dark gray rectangles show the central bandpasses and light gray rectangles show the continuum bandpasses for metallicity indices. We obtained three Fe indices and Mg index from the spectra of cluster members. We do not use Mg index to determine the metallicity at this point, as we have mentioned before. We will use Mg index later, when we will study the relation between age of the clusters and the metallicities determined with the index. Table 4.12 and 4.13 show the indices obtained with our spectra. Table 4.13 shows the results of the second observation for IC4665. We transformed the indices into Friel's one by using the formulae shown in Table 4.10. Table 4.14 and 4.15 show the transformed indices. We plotted transformed indices on the diagrams and obtained the metallicities of the stars in the clusters. The plotted diagrams appear in Figure 4.105 - 4.109, Figure 4.110 - 4.114, Figure 4.115 - 4.118, and Figure 4.119 - 4.123. Table 4.16 and 4.17 show the metallicities obtained from the diagrams. Finally, metallicities of the clusters were obtained on the average of each stars.

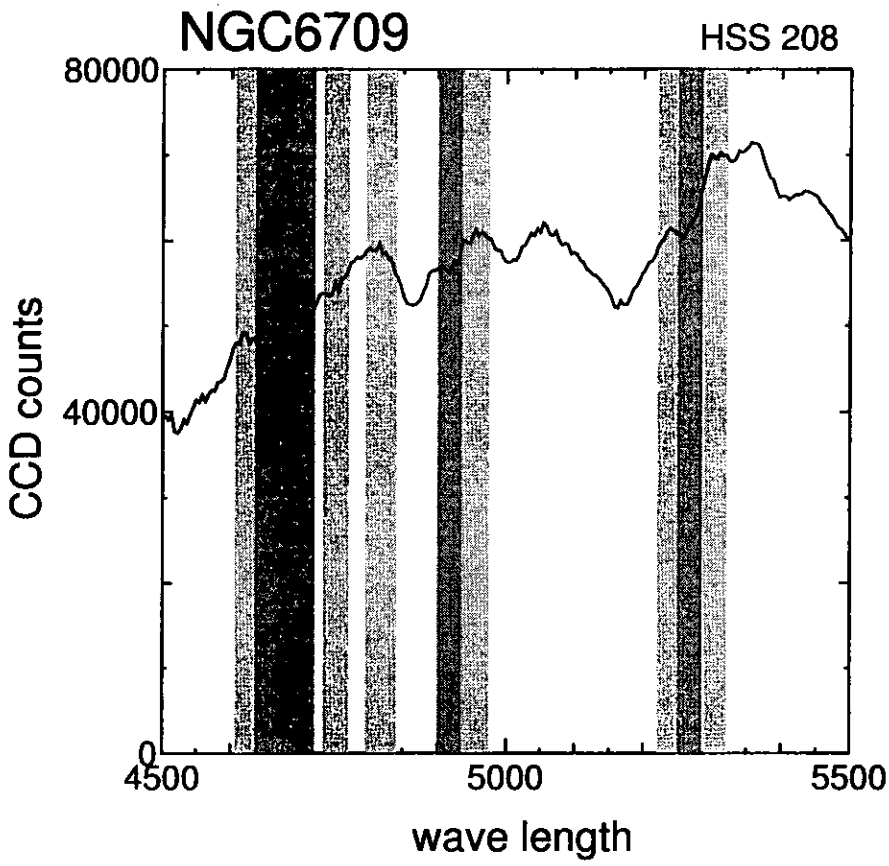

Figure 4.78: The spectrum of the stars in cluster. Dark gray rectangles show the central bandpasses and light gray rectangles show the continuum bandpasses for metallicity indices.

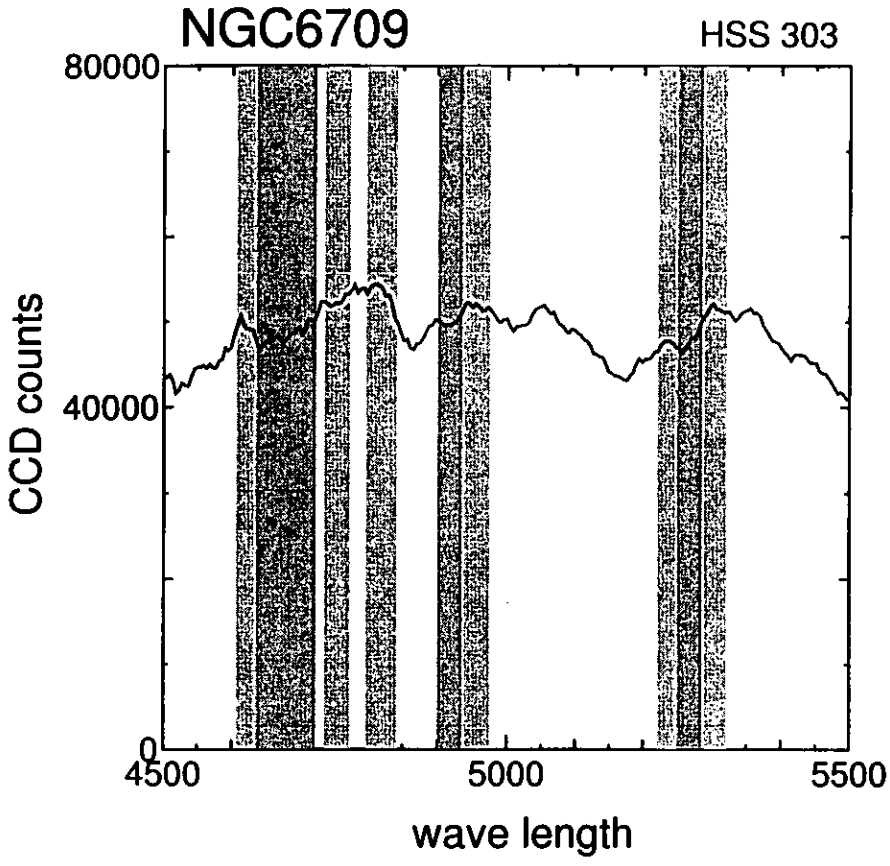

Figure 4.79: continued

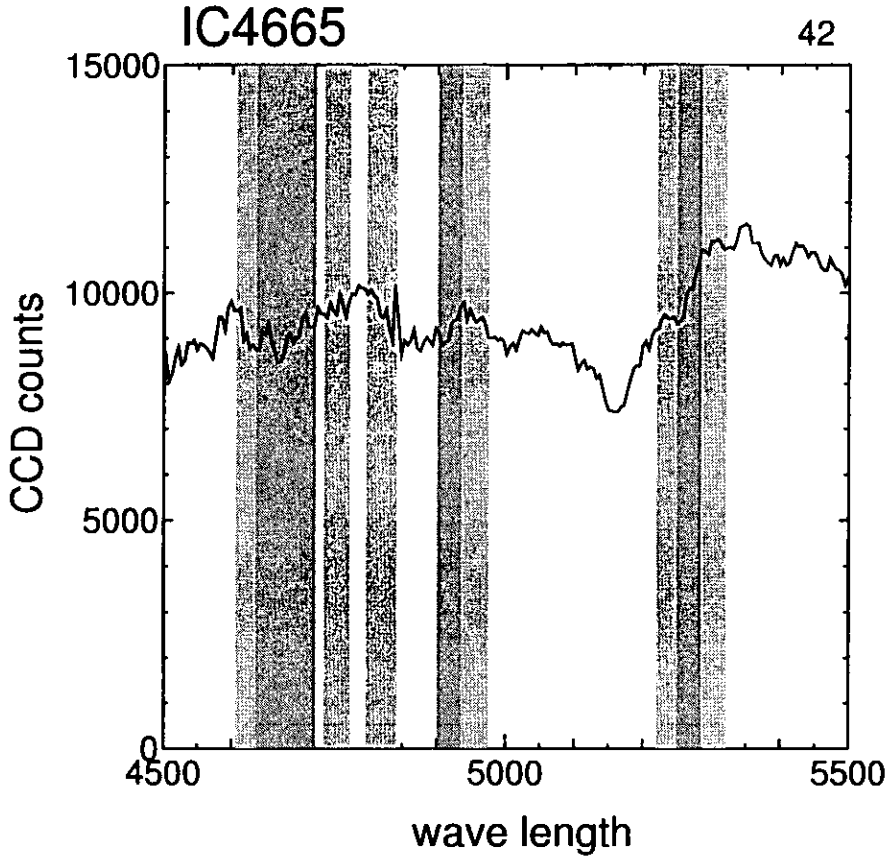

Figure 4.80: continued

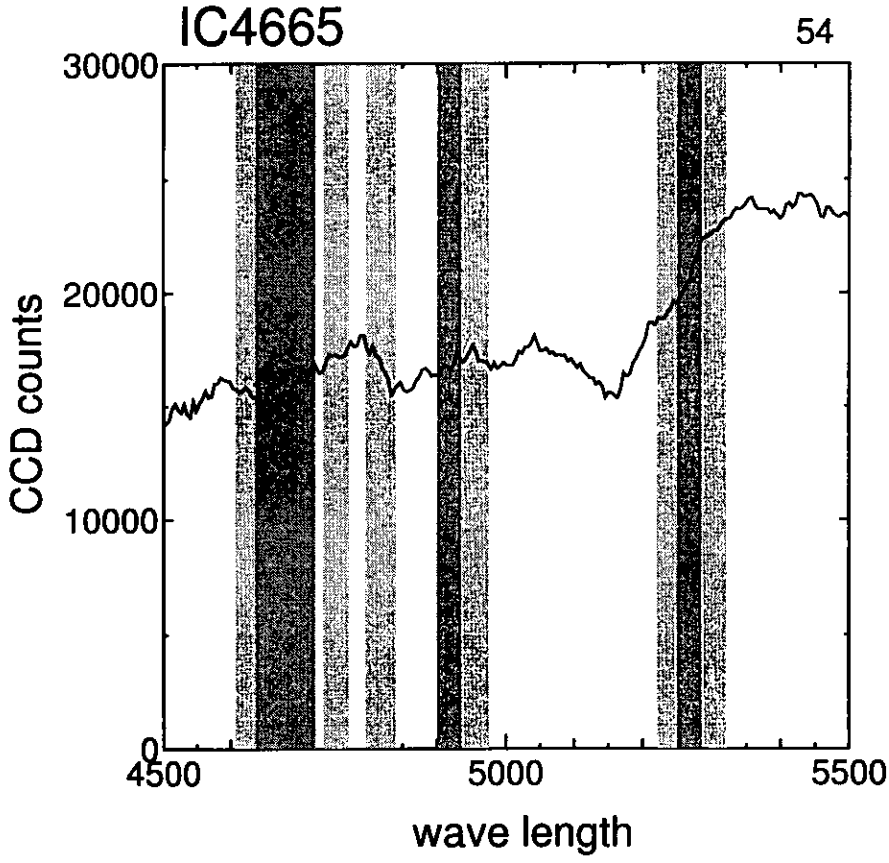

Figure 4.81: continued

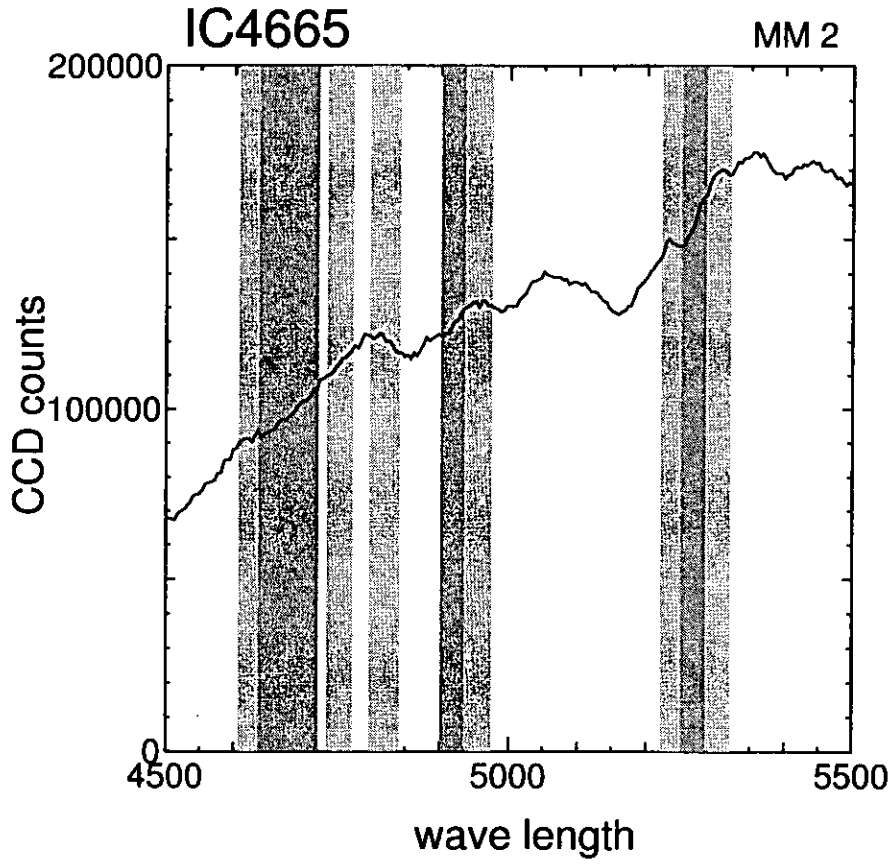

Figure 4.82: continued

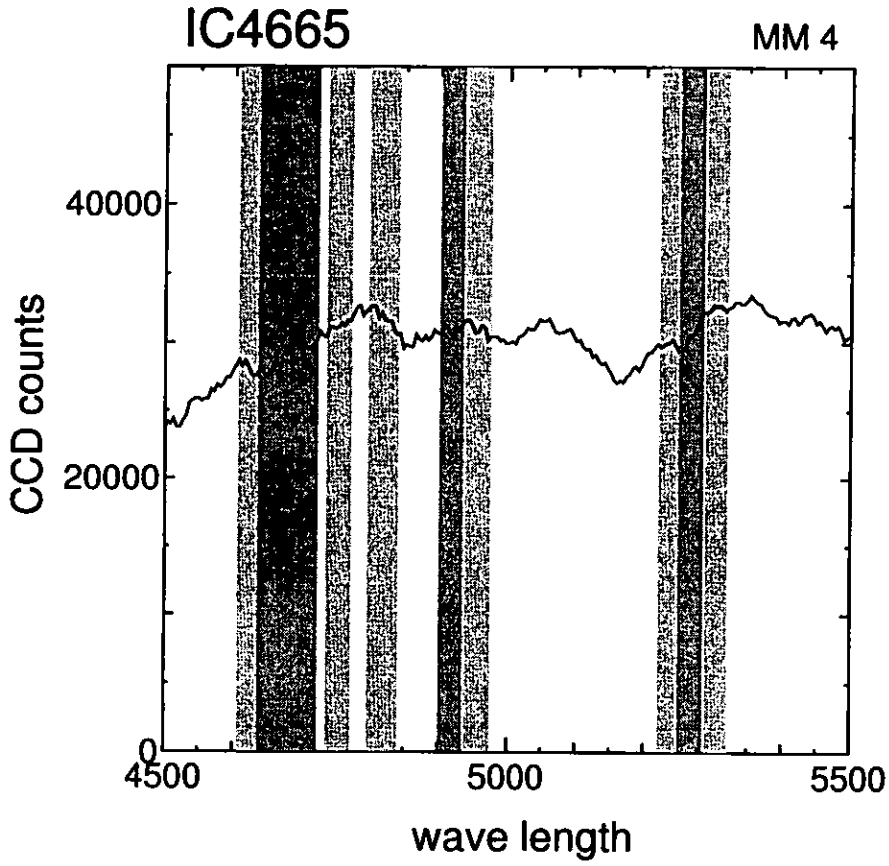

Figure 4.83: continued

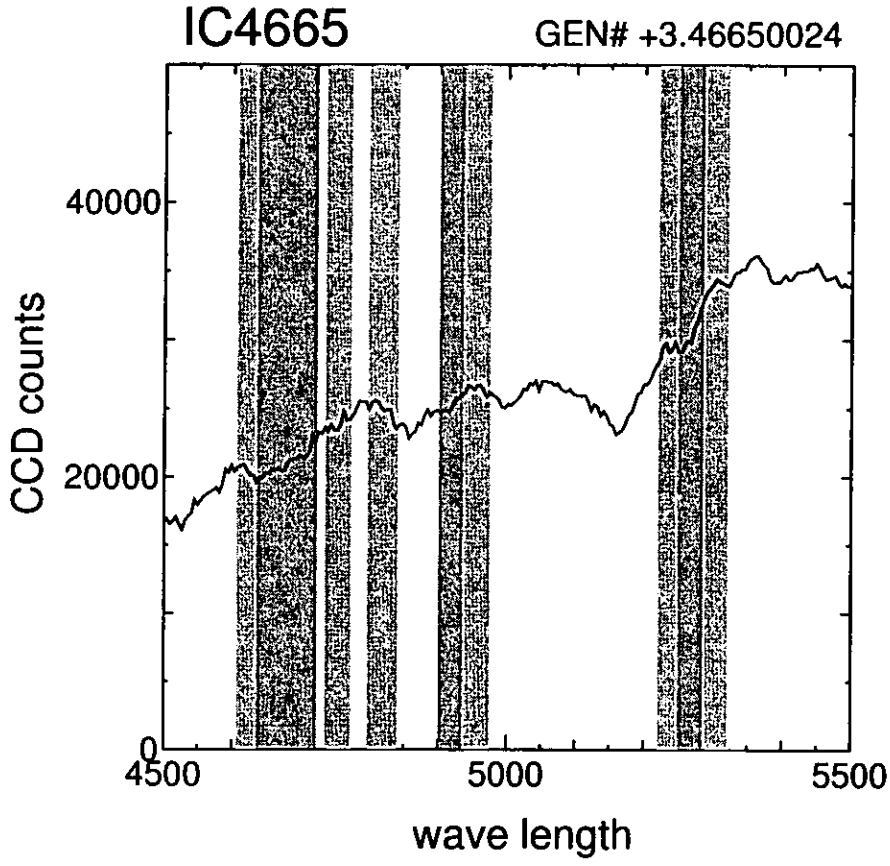

Figure 4.84: continued

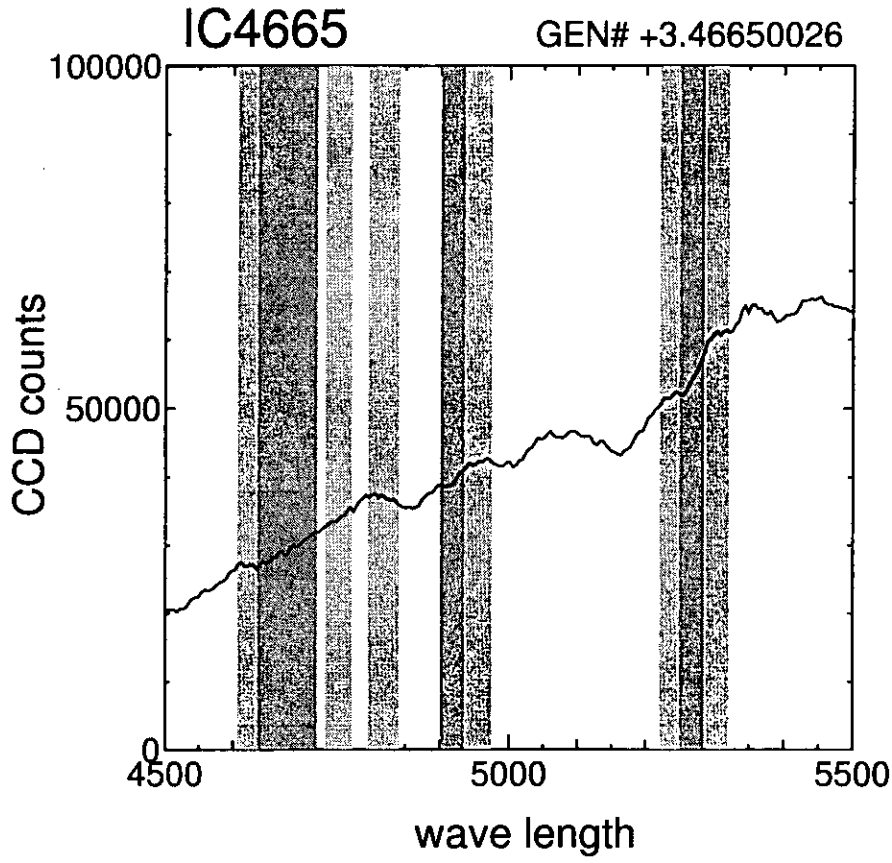

Figure 4.85: continued

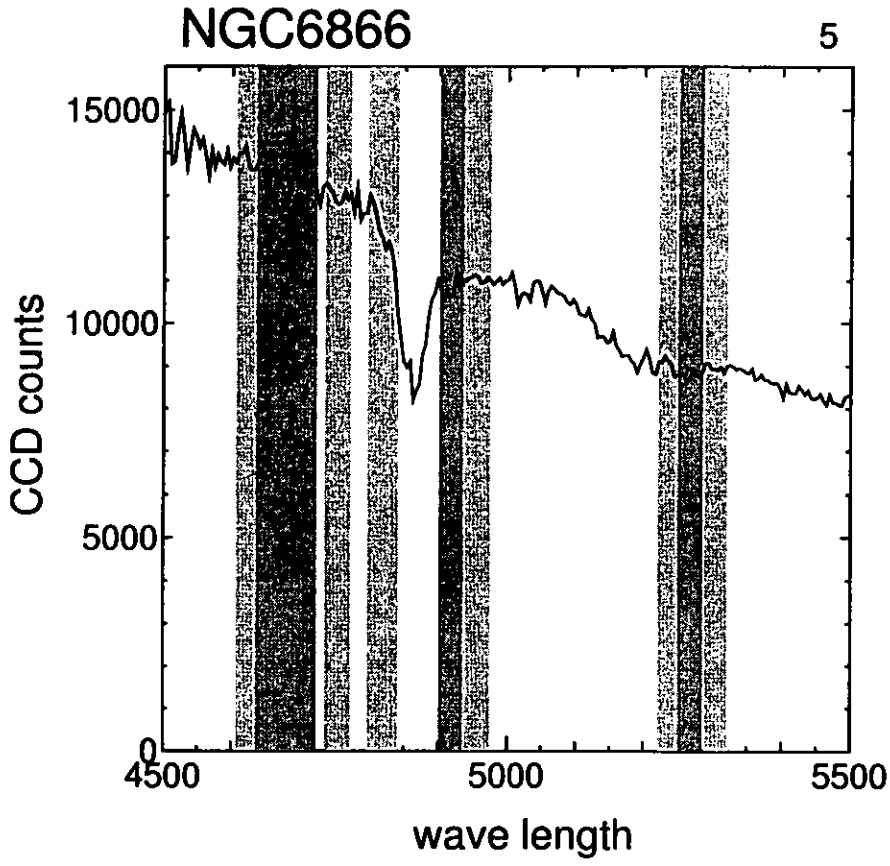

Figure 4.86: continued

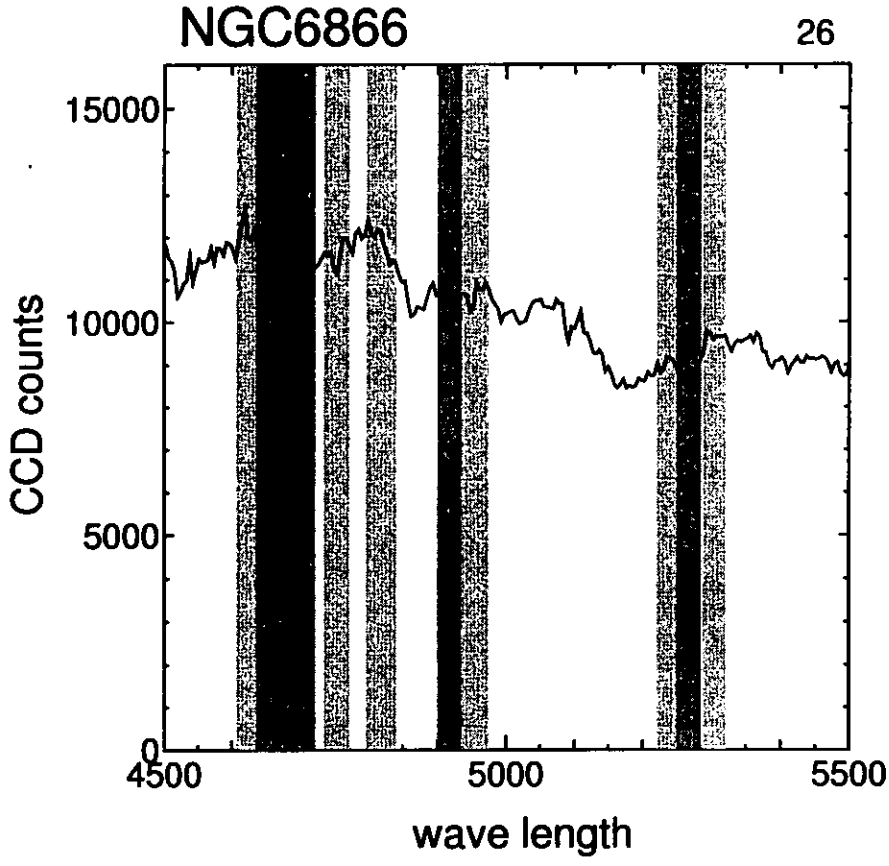

Figure 4.87: continued

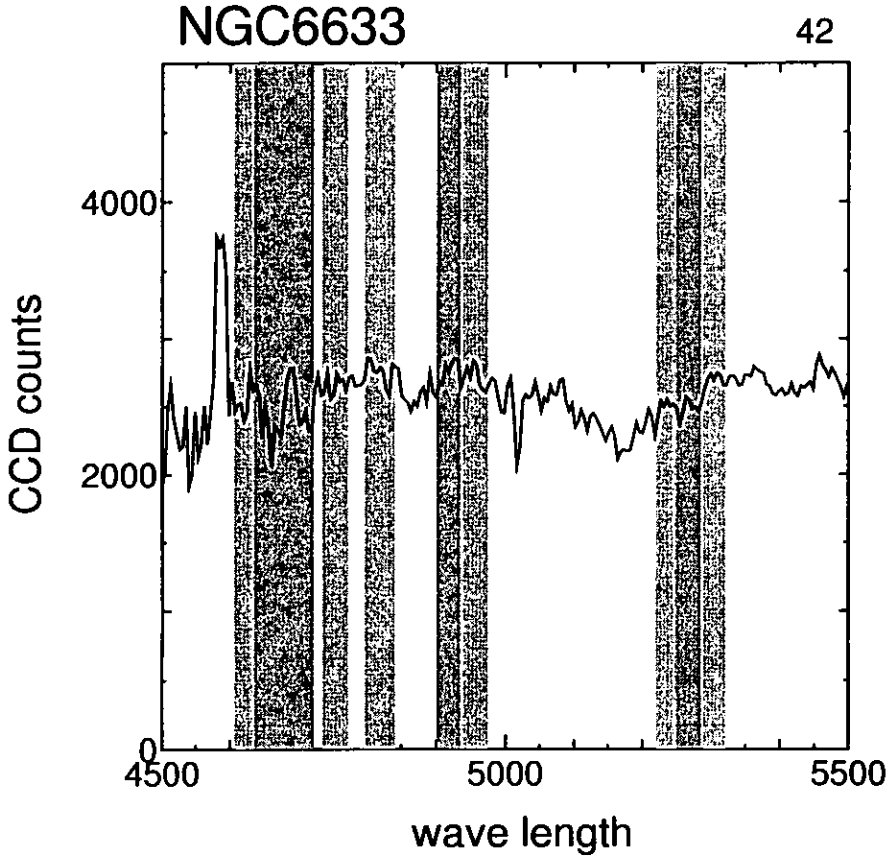

Figure 4.88: continued

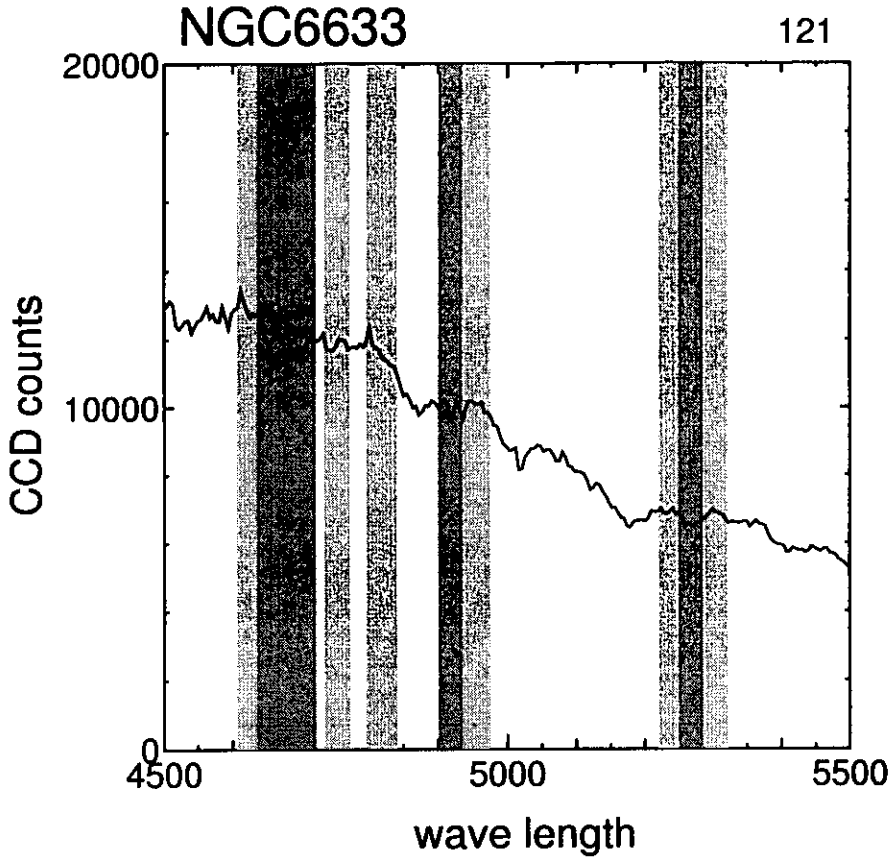

Figure 4.89: continued

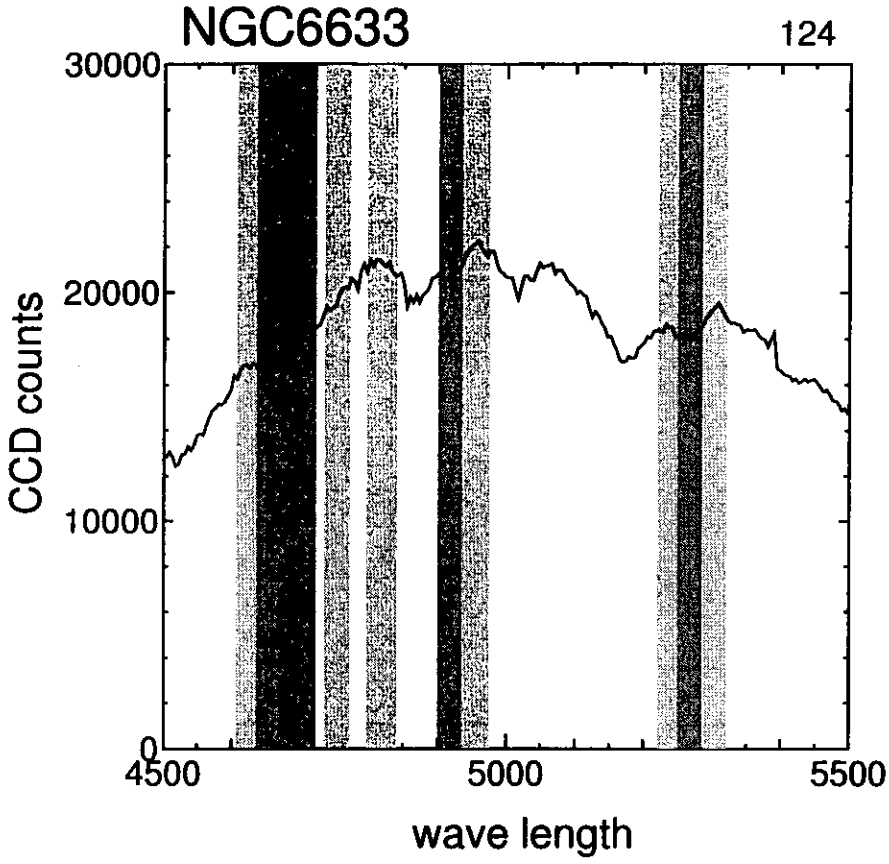

Figure 4.90: continued

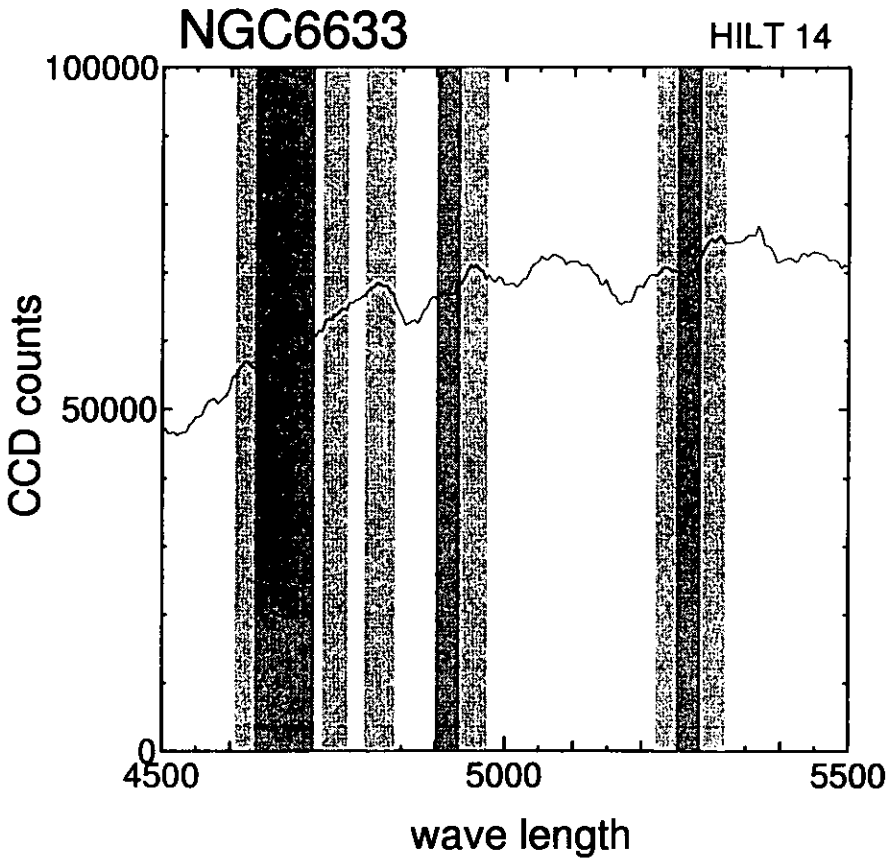

Figure 4.91: continued

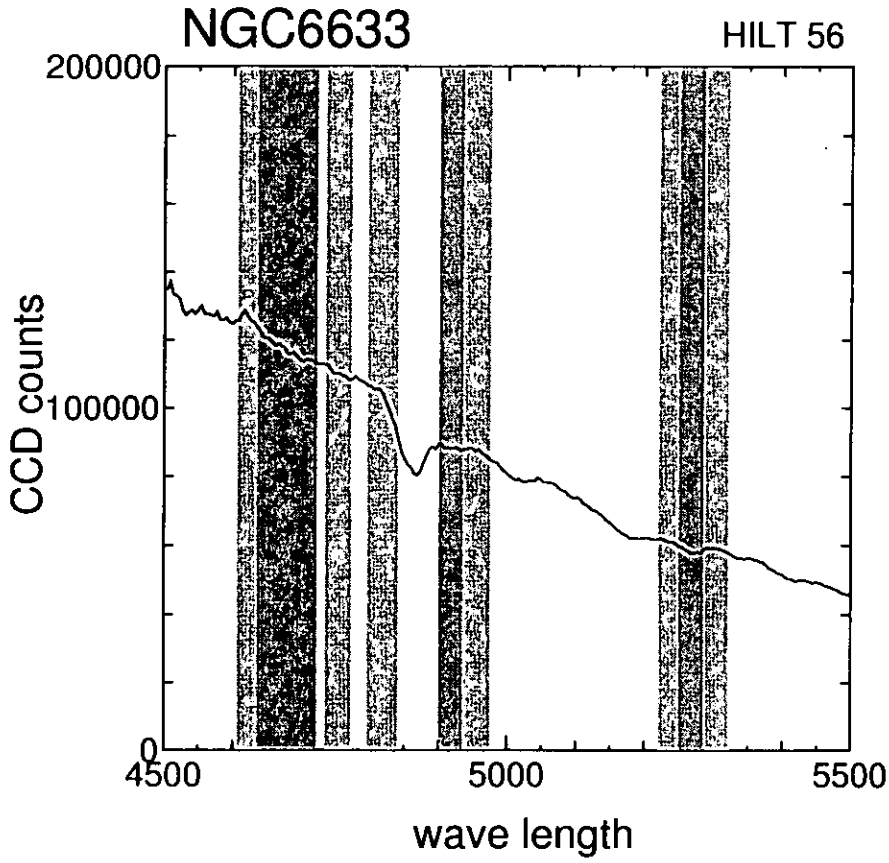

Figure 4.92: continued

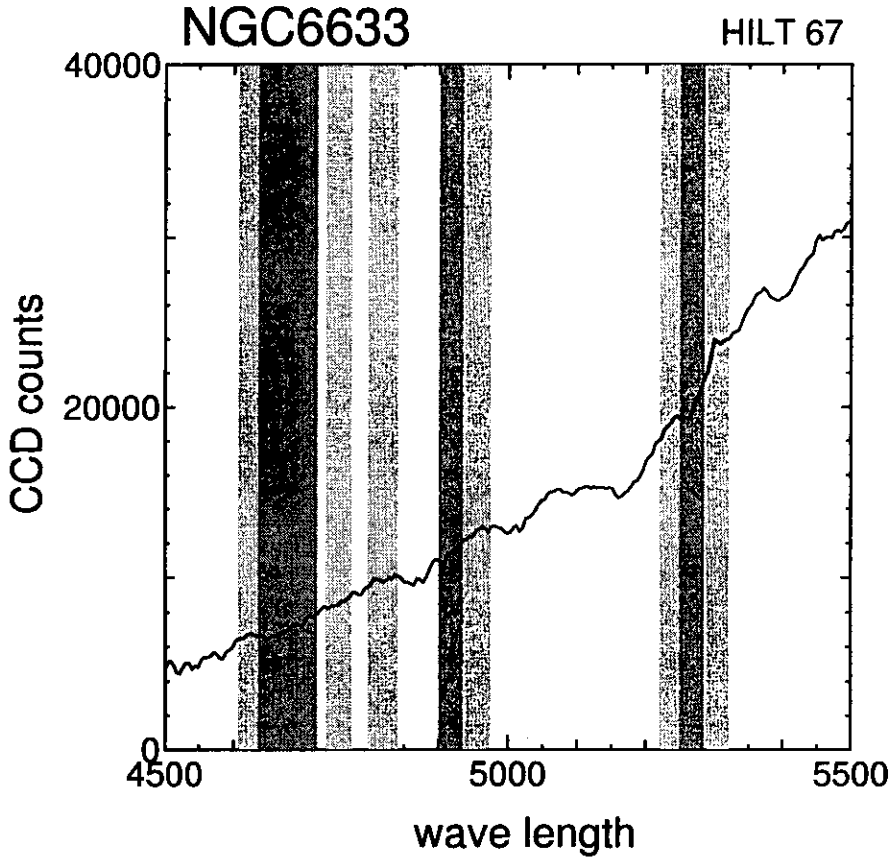

Figure 4.93: continued

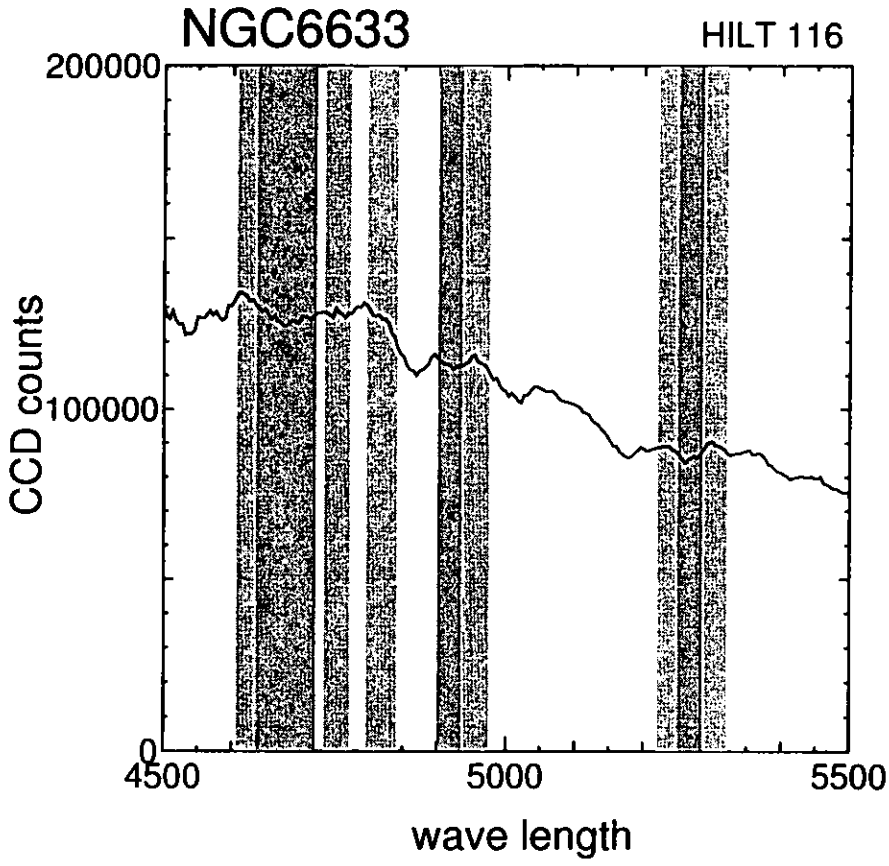

Figure 4.94: continued

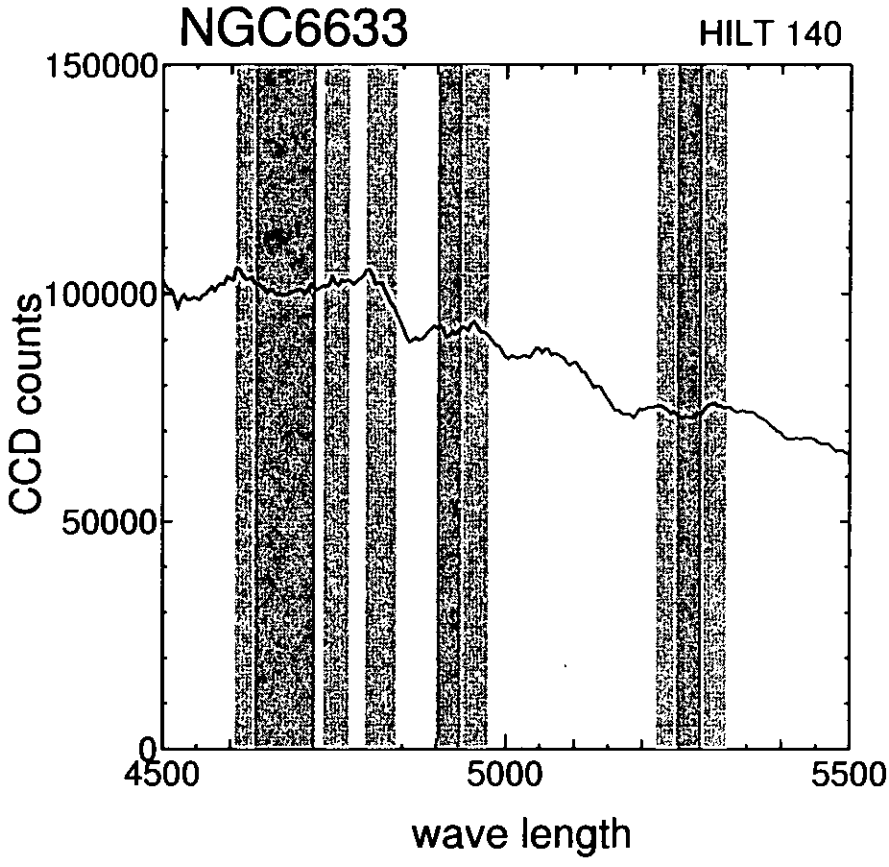

Figure 4.95: continued

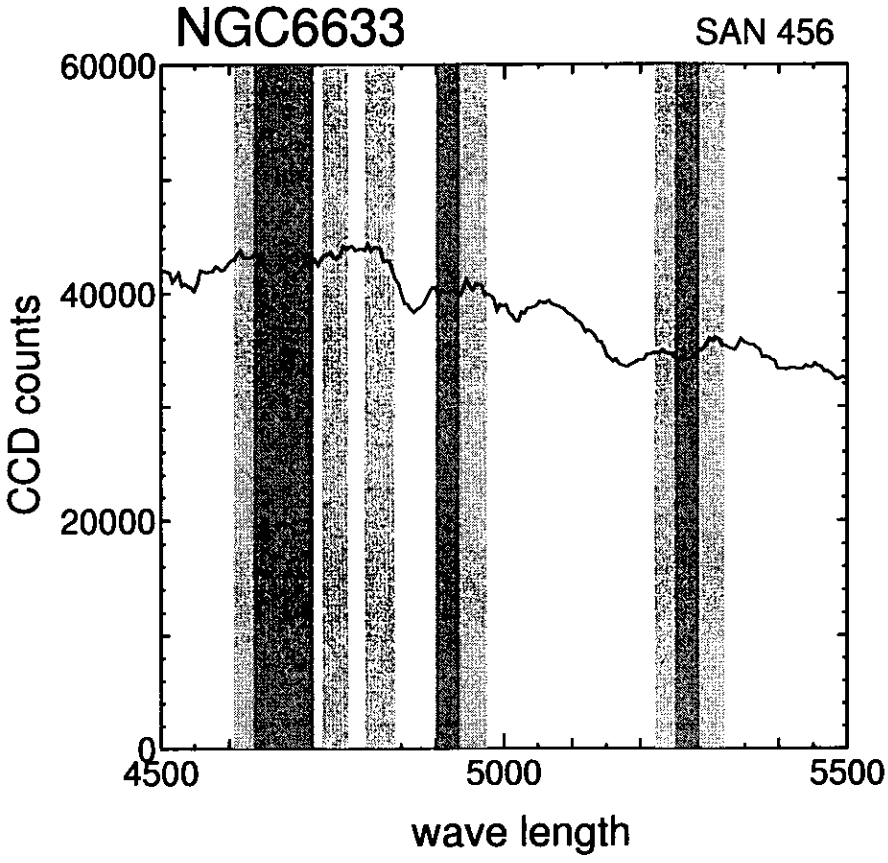

Figure 4.96: continued

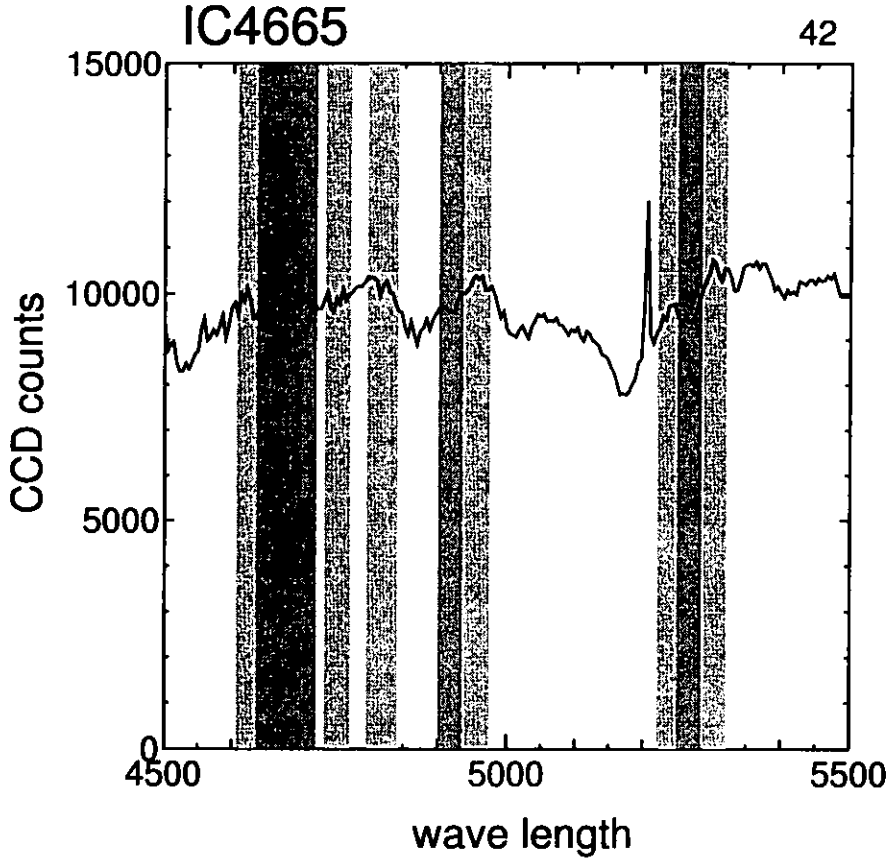

Figure 4.97: continued

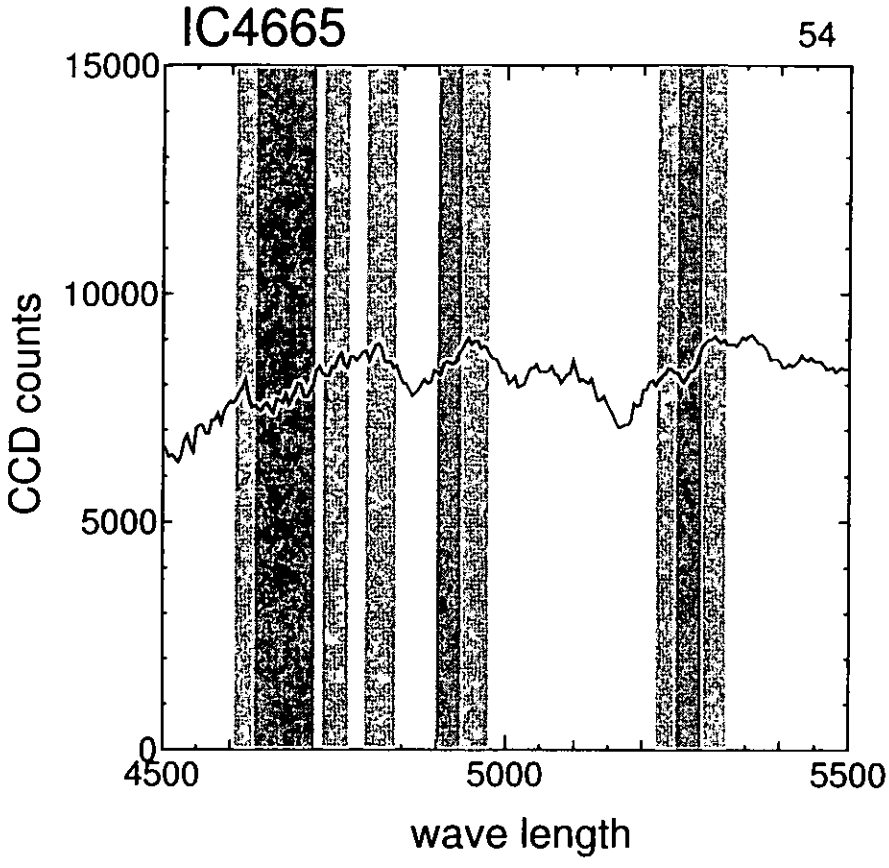

Figure 4.98: continued

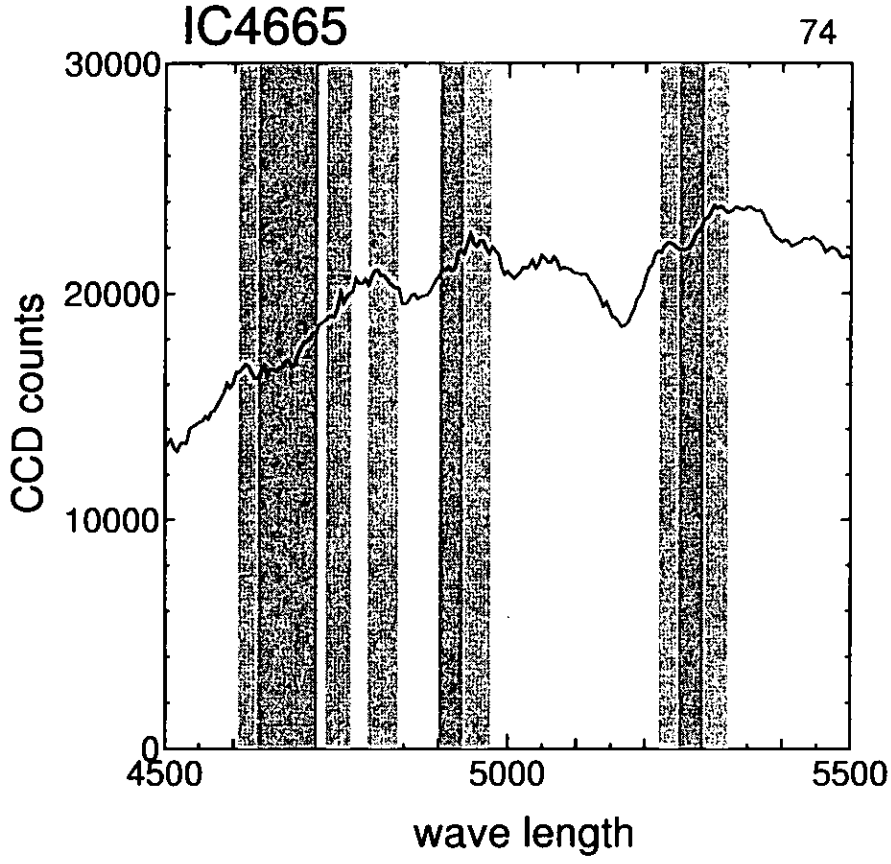

Figure 4.99: continued

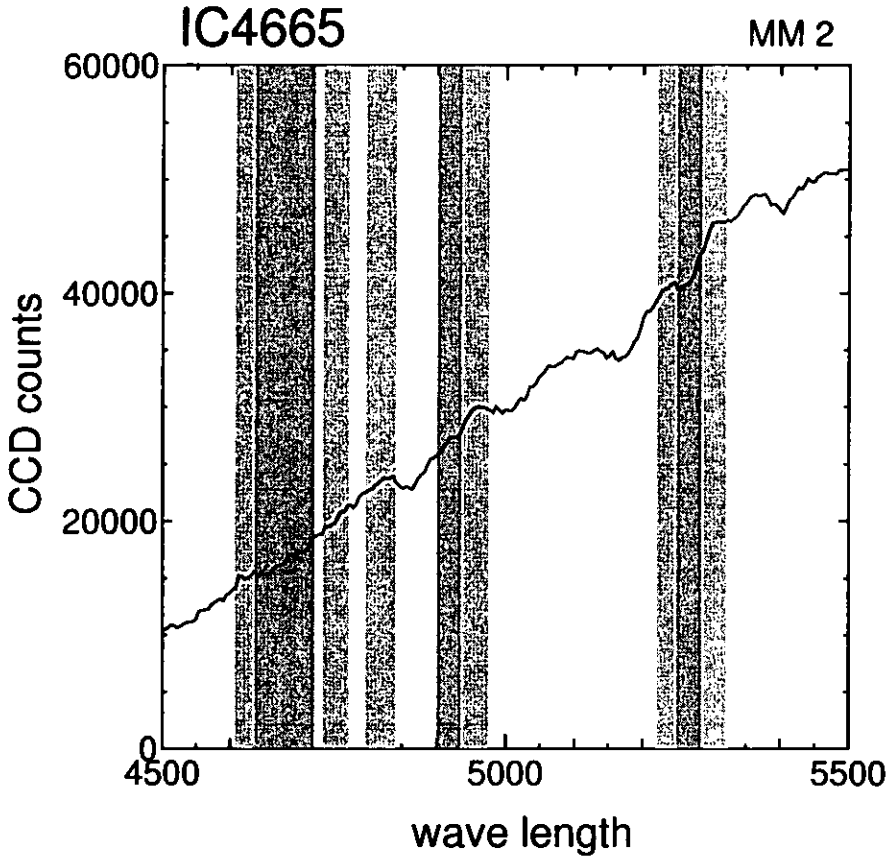

Figure 4.100: continued

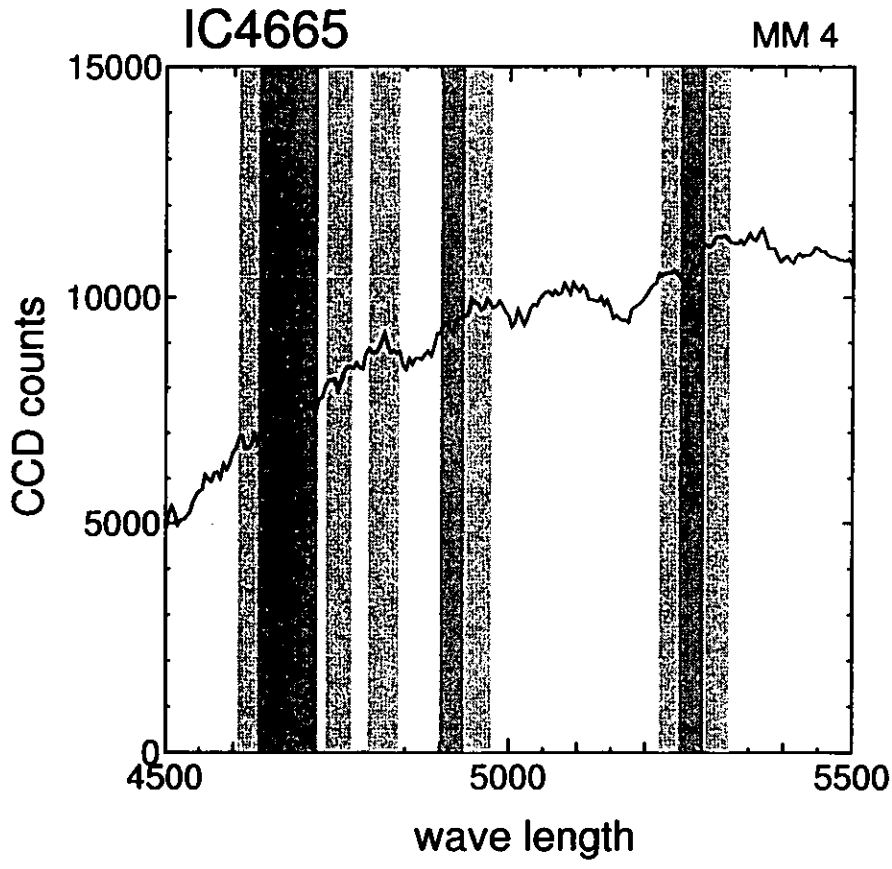

Figure 4.101: continued

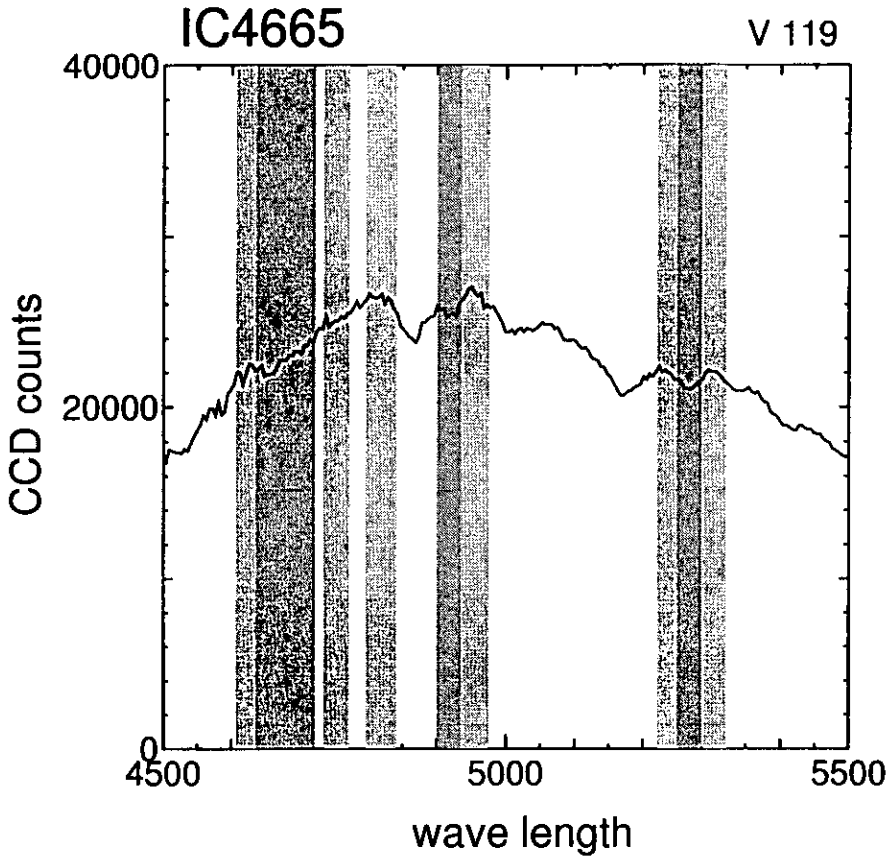

Figure 4.102: continued

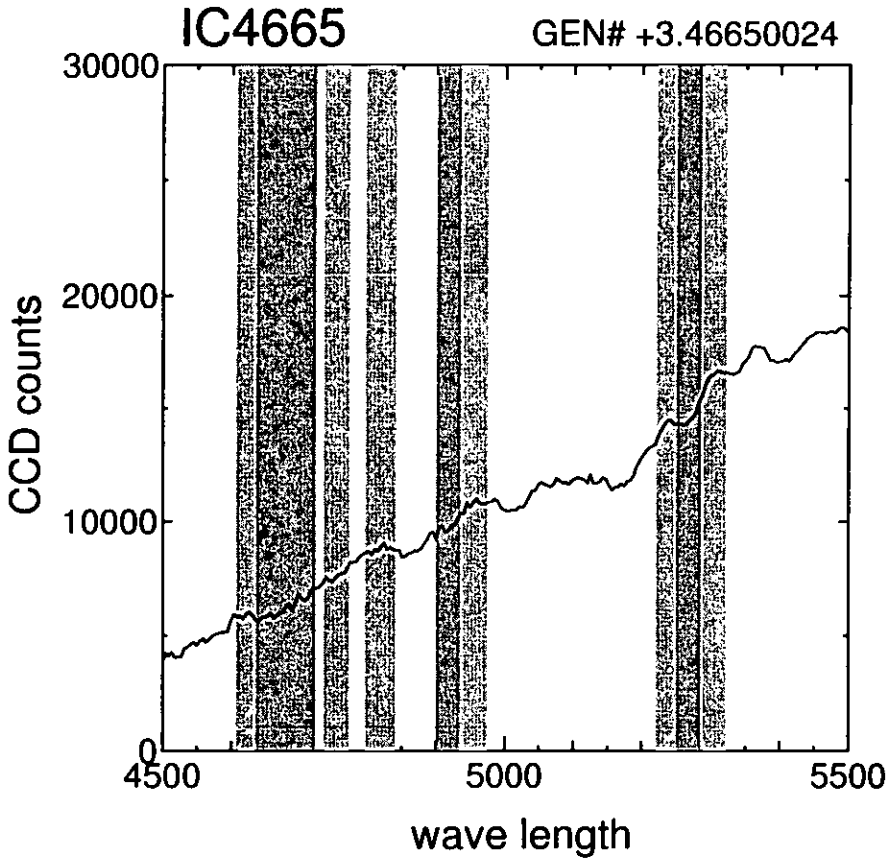

Figure 4.103: continued

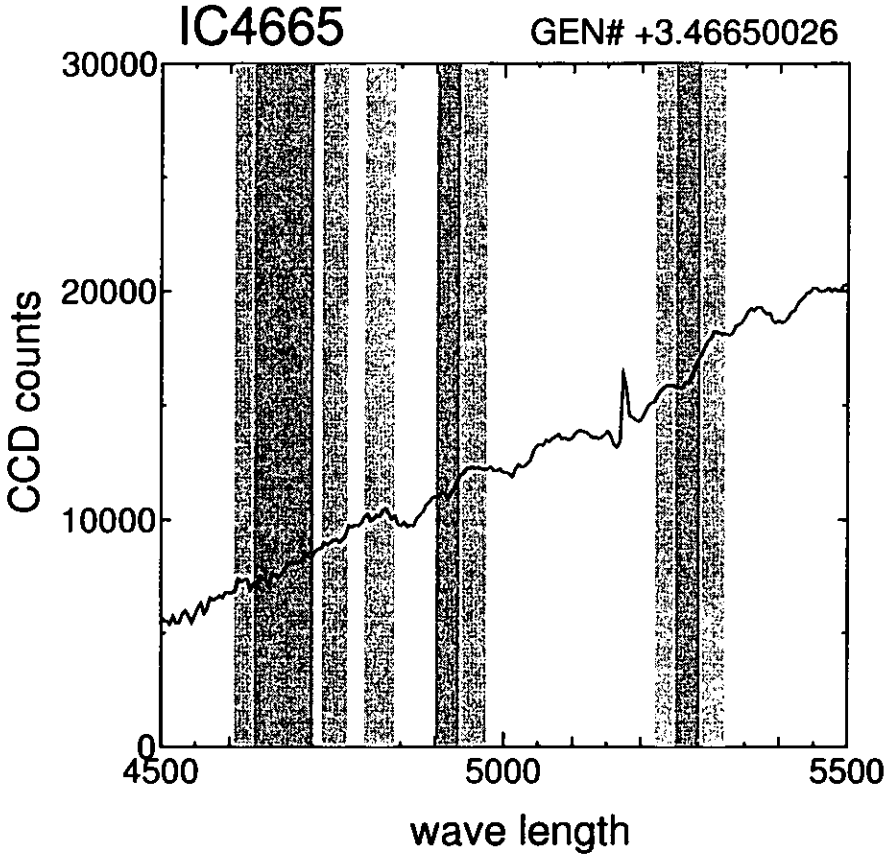

Figure 4.104: continued

Name	Fe4680	Fe4920	Fe5270	Mg
NGC 6709 HSS 208	0.805	0.782	0.793	0.960
NGC 6709 HSS 303	0.804	0.795	0.781	0.910
IC 4665 42	0.813	0.745	0.776	0.929
IC 4665 54	0.793	0.758	0.756	0.999
IC 4665 MM 2	0.801	0.750	0.772	0.902
IC 4665 MM 4	0.790	0.764	0.771	0.898
GEN +3.46650024	0.811	0.762	0.786	0.991
GEN +3.46650026	0.802	0.746	0.783	0.923
NGC 6866 5	0.740	0.817	0.778	0.820
NGC 6866 26	0.794	0.833	0.805	0.913
NGC 6633 42	0.808	0.750	0.788	0.939
NGC 6633 121	0.782	0.836	0.788	0.948
NGC 6633 124	0.816	0.779	0.784	0.894
NGC 6633 HILT 14	0.793	0.774	0.780	0.833
NGC 6633 HILT 56	0.761	0.824	0.776	0.868
NGC 6633 HILT 67	0.817	0.729	0.806	0.993
NGC 6633 HILT 116	0.781	0.812	0.784	0.878
NGC 6633 HILT 140	0.779	0.807	0.776	0.859
NGC 6633 SAN 456	0.780	0.798	0.775	0.857

Table 4.12: Indices calculated with our spectra.

Name	Fe4680	Fe4920	Fe5270	Mg
IC 4665 42	0.803	0.792	0.795	0.980
IC 4665 54	0.804	0.780	0.784	0.949
IC 4665 74	0.804	0.751	0.775	0.933
IC 4665 MM 2	0.817	0.723	0.789	0.849
IC 4665 MM 4	0.807	0.741	0.779	0.837
IC 4665 V 119	0.786	0.776	0.780	0.863
GEN +3.46650024	0.833	0.741	0.799	0.919
GEN +3.46650026	0.799	0.739	0.790	0.845

Table 4.13: continued

Name	Fe4680	Fe4920	Fe5270	Mg
NGC 6709 HSS 208	0.862	0.775	0.843	0.949
NGC 6709 HSS 303	0.861	0.778	0.833	0.909
IC 4665 42	0.853	0.776	0.824	1.017
IC 4665 54	0.847	0.769	0.816	0.981
IC 4665 MM 2	0.857	0.768	0.826	0.903
IC 4665 MM 4	0.843	0.771	0.825	0.899
GEN +3.46650024	0.869	0.770	0.837	0.974
GEN +3.46650026	0.858	0.766	0.835	0.919
NGC 6866 5	0.782	0.783	0.831	0.837
NGC 6866 26	0.849	0.787	0.852	0.911
NGC 6633 42	0.866	0.767	0.839	0.932
NGC 6633 121	0.833	0.788	0.839	0.939
NGC 6633 124	0.875	0.774	0.836	0.896
NGC 6633 HILT 14	0.847	0.773	0.832	0.847
NGC 6633 HILT 56	0.808	0.785	0.829	0.875
NGC 6633 HILT 67	0.876	0.763	0.852	0.975
NGC 6633 HILT 116	0.833	0.782	0.835	0.883
NGC 6633 HILT 140	0.830	0.781	0.829	0.867
NGC 6633 SAN 456	0.832	0.779	0.828	0.866

Table 4.14: Indices transformed into Friel's.

Name	Fe4680	Fe4920	Fe5270	Mg
IC 4665 42	0.860	0.777	0.844	0.965
IC 4665 54	0.861	0.774	0.836	0.940
IC 4665 74	0.860	0.768	0.828	0.927
IC 4665 MM 2	0.877	0.761	0.840	0.860
IC 4665 MM 4	0.864	0.765	0.829	0.850
IC 4665 V 119	0.839	0.774	0.833	0.871
GEN +3.46650024	0.895	0.765	0.847	0.916
GEN +3.46650026	0.854	0.765	0.840	0.858

Table 4.15: continued

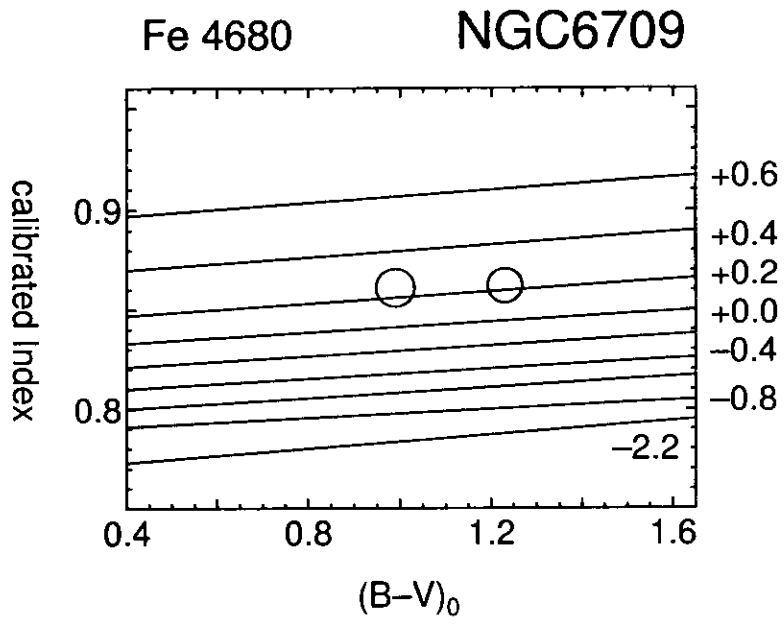

Figure 4.105: Fe4680 index versus $(B - V)_0$ for the stars in the clusters. Lines of constant metallicity presented by Friel are indicated. Radii of the circles are in proportion to S/N of the spectrum.

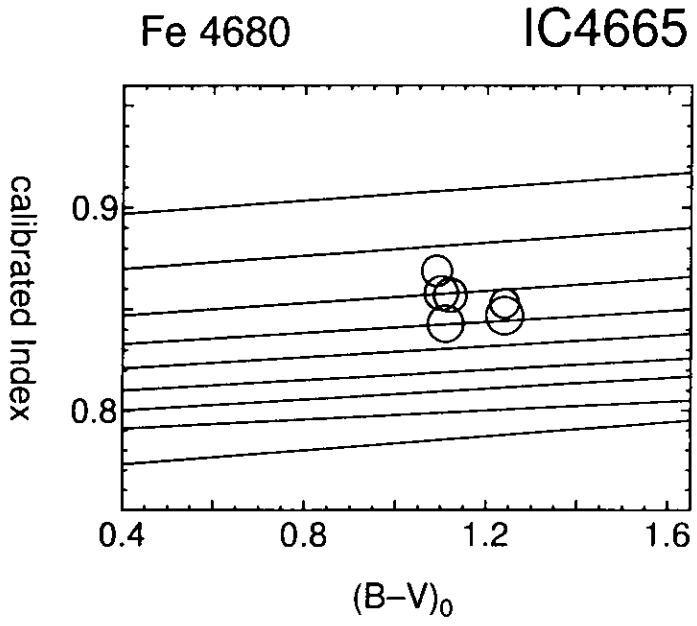

Figure 4.106: continued

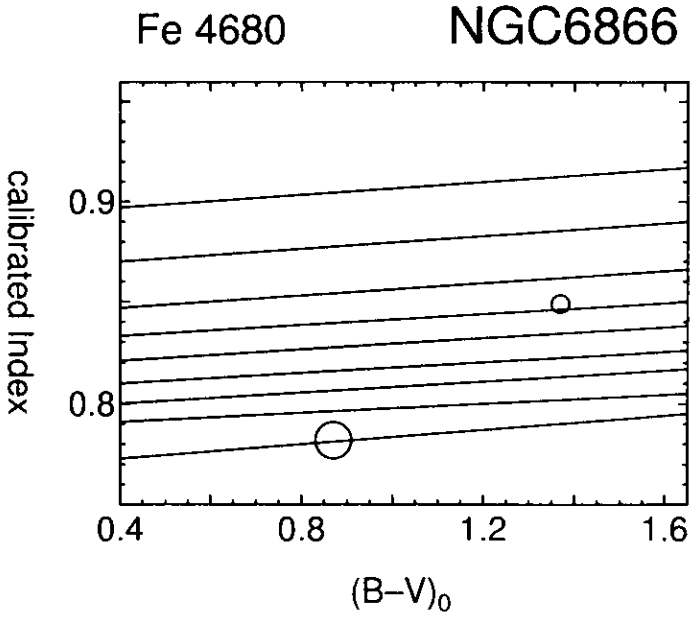

Figure 4.107: continued

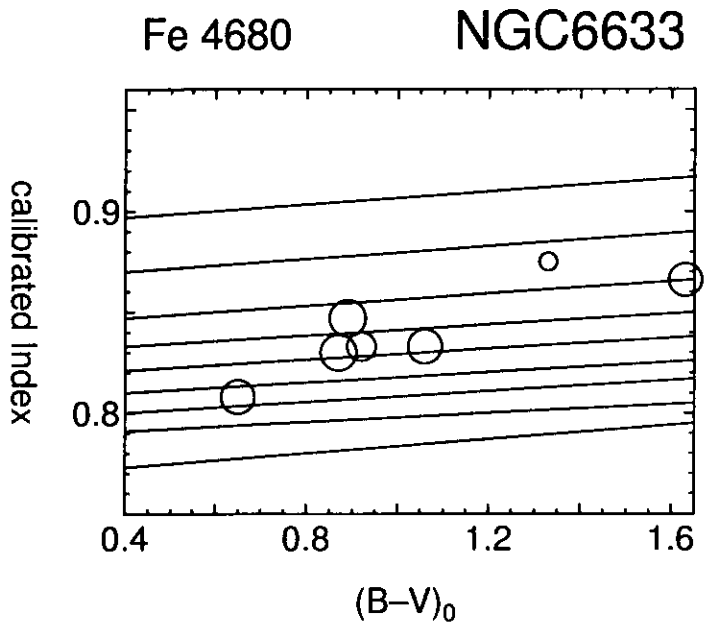

Figure 4.108: continued

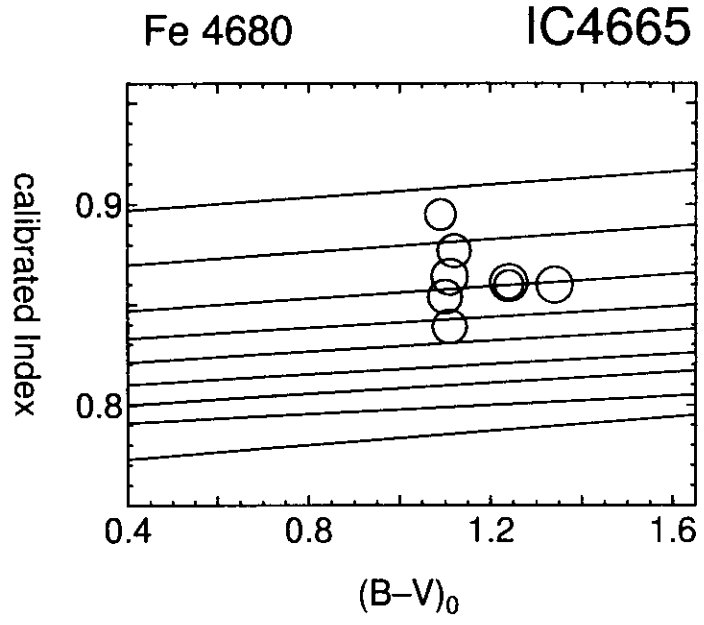

Figure 4.109: continued

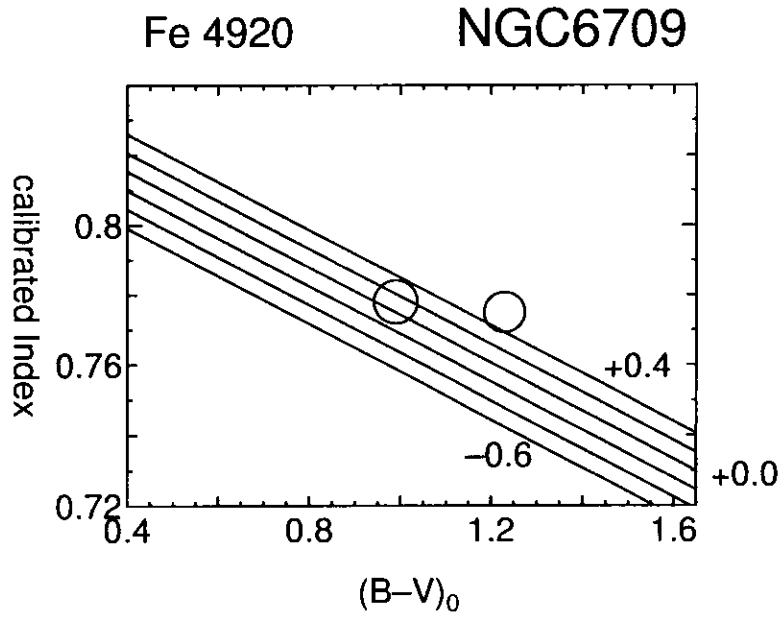

Figure 4.110: Fe4920 index versus $(B - V)_0$ for the stars in the clusters. Lines of constant metallicity presented by Friel are indicated. Radii of the circles are in proportion to S/N of the spectrum.

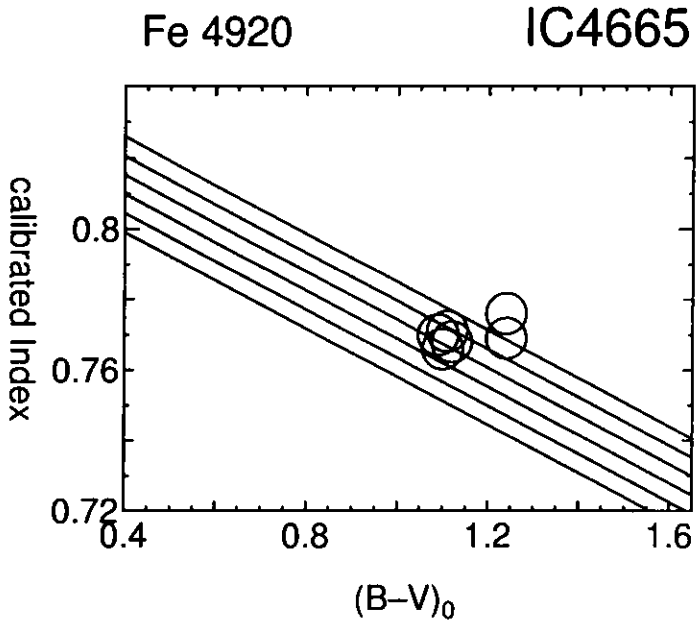

Figure 4.111: continued

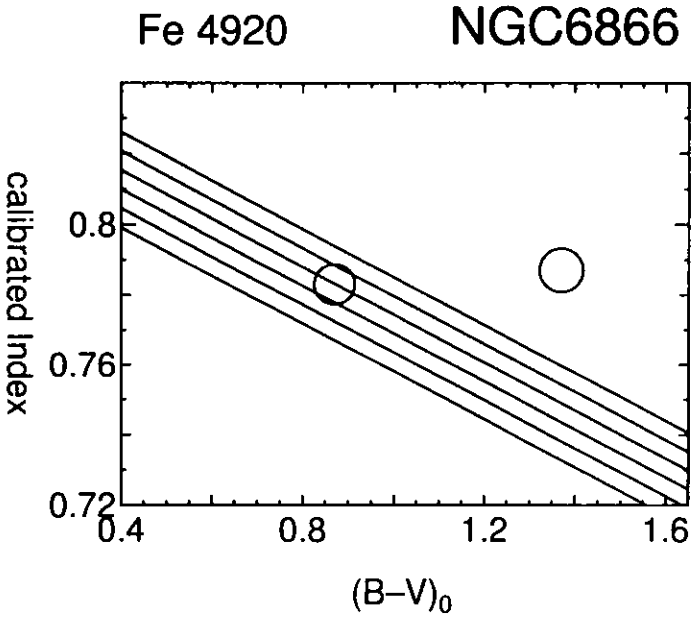

Figure 4.112: continued

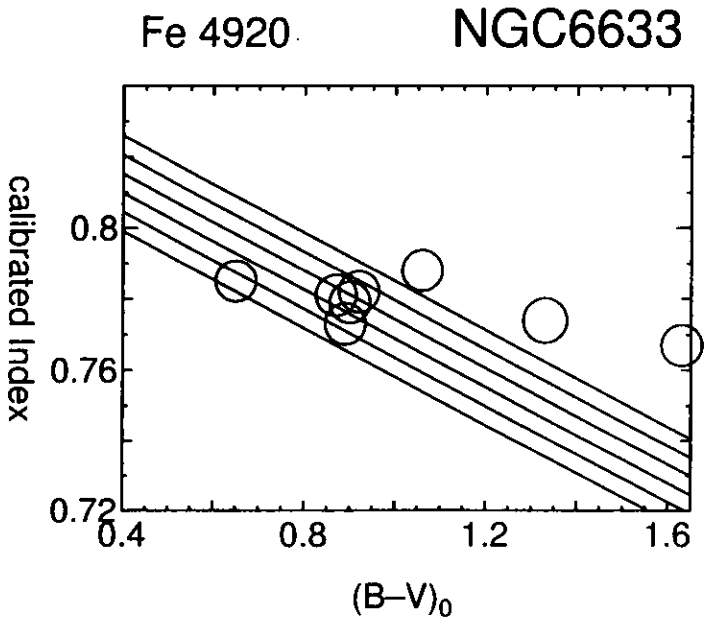

Figure 4.113: continued

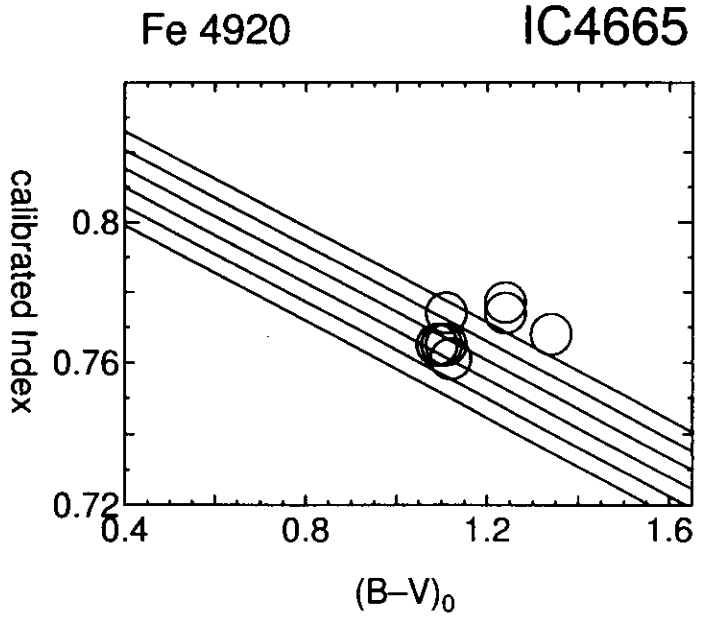

Figure 4.114: continued

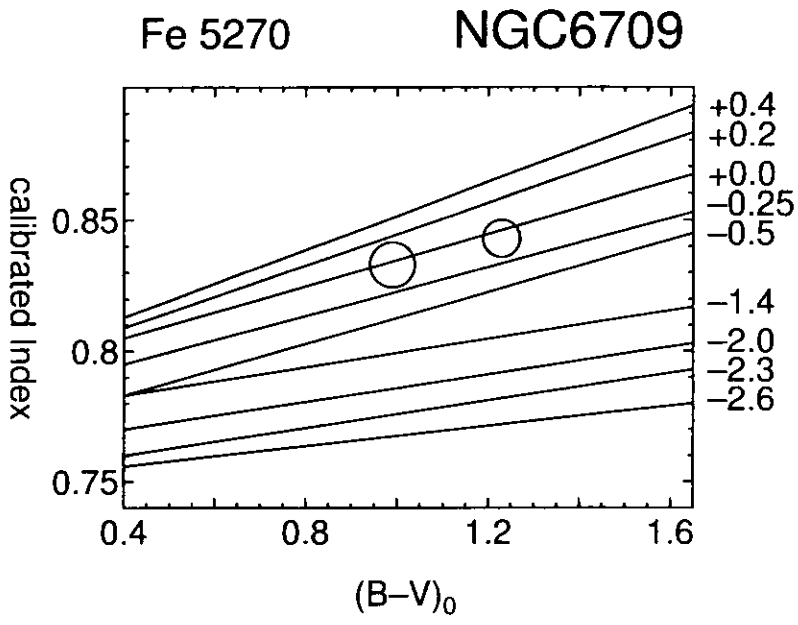

Figure 4.115: Fe5270 index versus $(B - V)_0$ for the stars in the clusters. Lines of constant metallicity presented by Friel are indicated. Radii of the circles are in proportion to S/N of the spectrum.

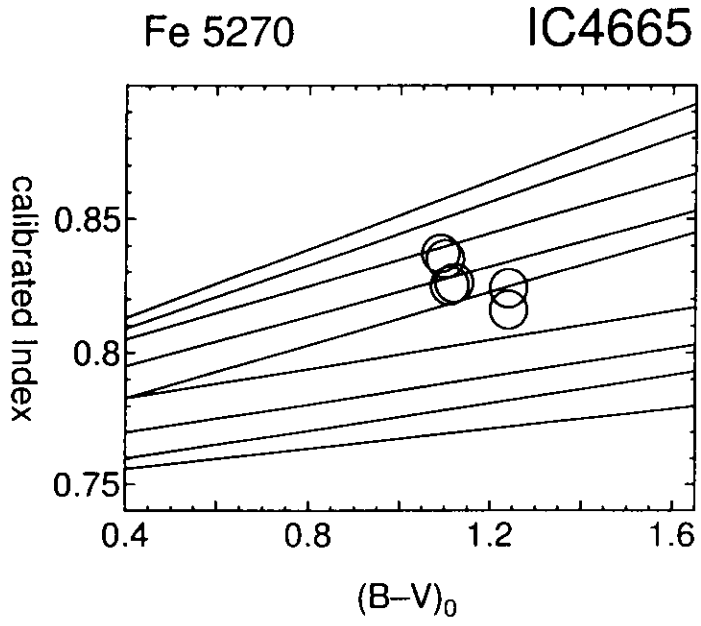

Figure 4.116: continued

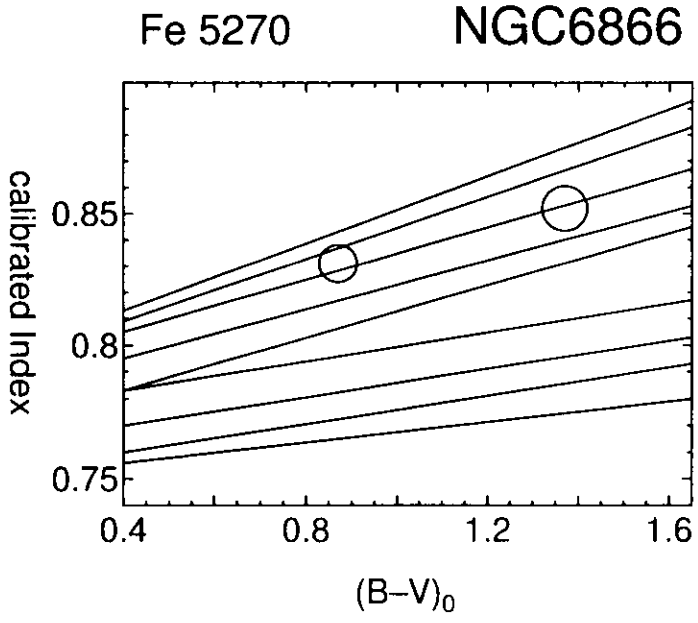

Figure 4.117: continued

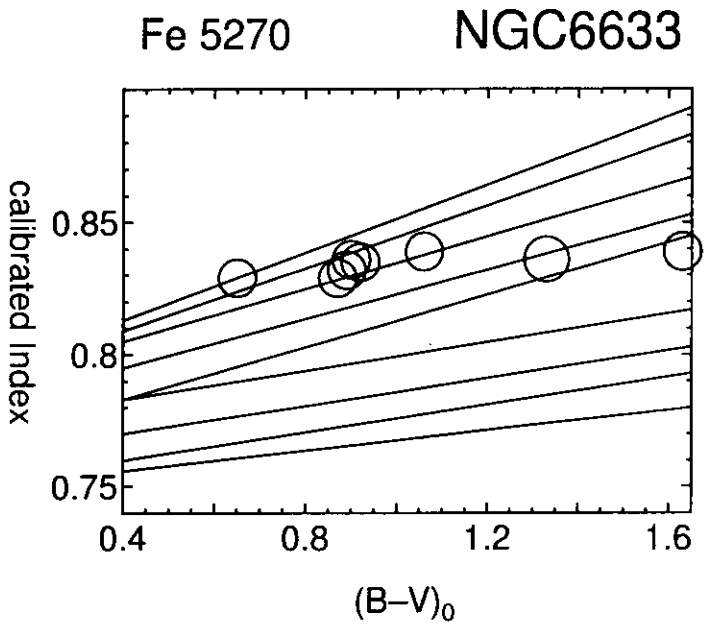

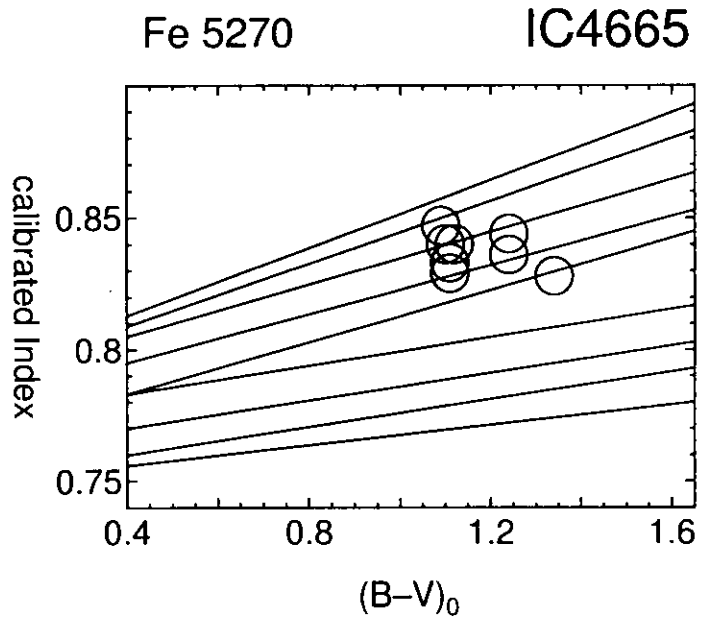

Figure 4.118: continued

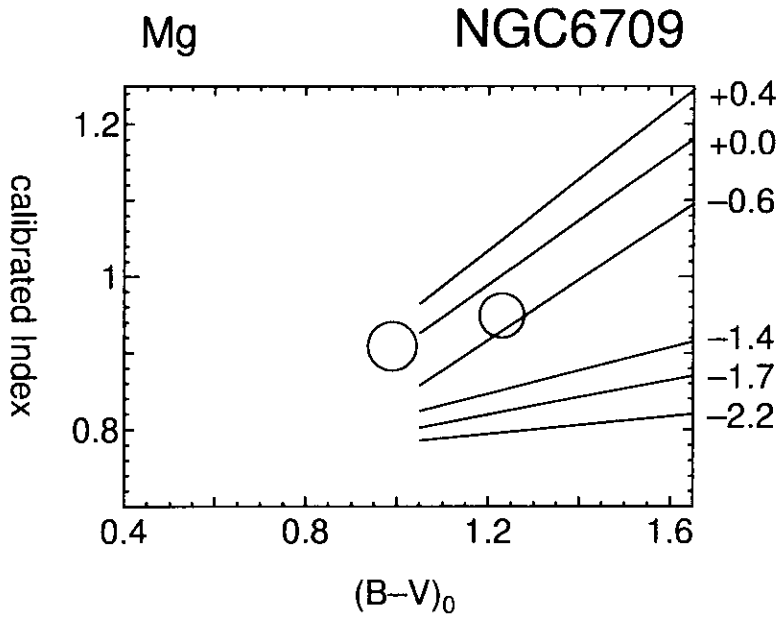

Figure 4.119: Mg index versus $(B-V)_0$ for the stars in the clusters. Lines of constant metallicity presented by Friel are indicated. Radii of the circles are in proportion to S/N of the spectrum. We also determined metallicities of the stars with $(B-V) < 1.05$ by following Friel's definition.

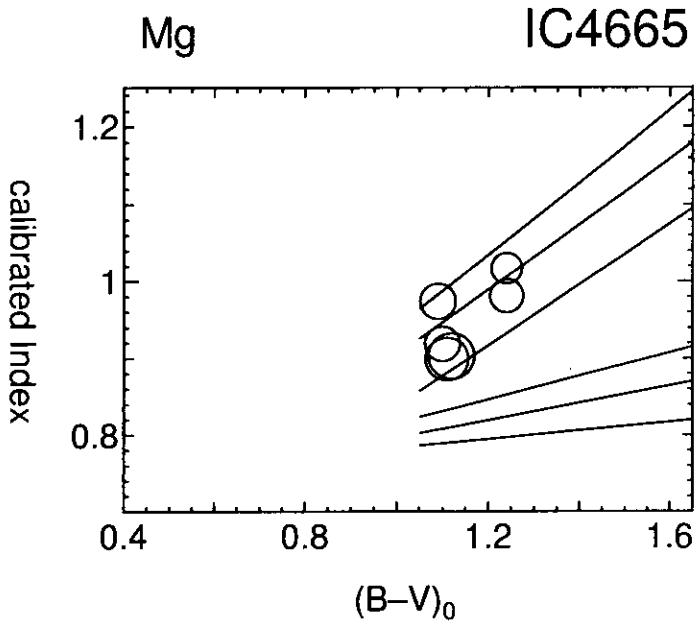

Figure 4.120: continued

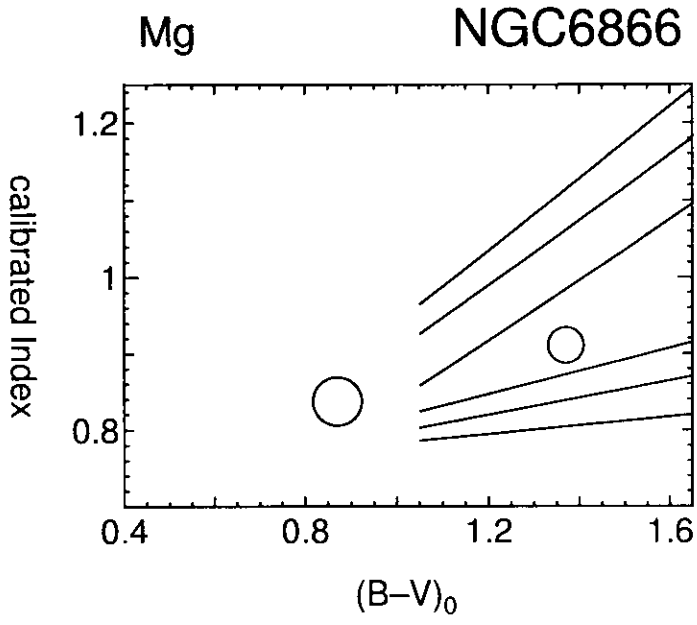

Figure 4.121: continued

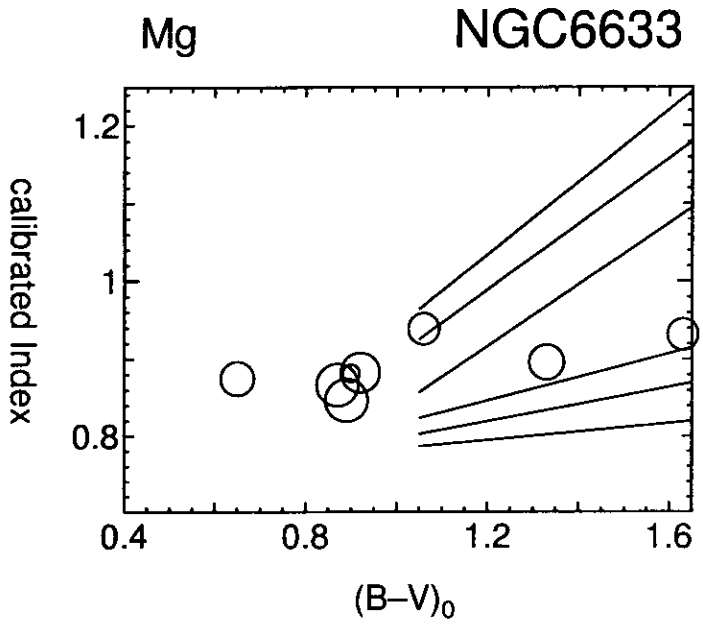

Figure 4.122: continued

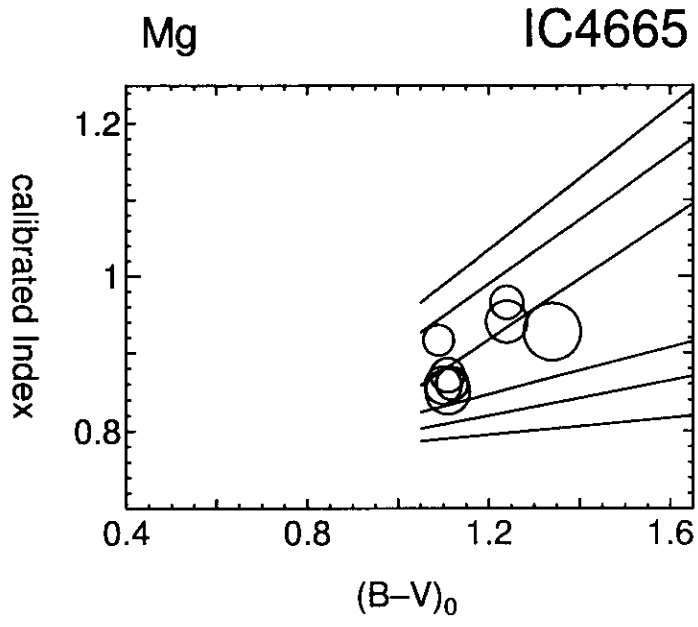

Figure 4.123: continued

Name	$[Fe/H]_{Fe4680}$	$[Fe/H]_{Fe4920}$	$[Fe/H]_{Fe5270}$	$[Fe/H]_{Mg}$	$[Fe/H]^{Weighted}_{Mean}$
NGC 6709 HSS 208	0.231	0.612	−0.063	−0.434	0.142
NGC 6709 HSS 303	0.243	0.115	−0.027	0.000	0.162
IC 4665 42	0.112	0.675	−0.518	0.092	0.060
IC 4665 54	0.034	0.415	−0.914	−0.205	−0.068
IC 4665 MM 2	0.188	0.072	−0.312	−0.447	0.034
IC 4665 MM 4	0.006	0.160	−0.326	−0.447	−0.098
GEN +3.46650024	0.298	0.071	−0.046	0.312	0.194
GEN +3.46650026	0.205	−0.054	−0.096	−0.240	0.114
NGC 6866 5	−2.132	−0.006	0.063	−0.600	−0.738
NGC 6866 26	0.036	1.411	−0.021	−1.058	0.019
NGC 6633 42	0.204	1.328	−0.655	−1.264	0.152
NGC 6633 121	−0.150	0.664	0.024	0.094	0.001
NGC 6633 124	0.317	0.828	−0.310	−1.124	0.125
NGC 6633 HILT 14	0.099	−0.326	0.062	−0.400	0.089
NGC 6633 HILT 56	−0.506	−0.489	0.400	0.300	0.029
NGC 6633 HILT 67	0.334	0.244	0.071	−0.321	0.256
NGC 6633 HILT 116	−0.118	0.085	0.094	−0.100	0.020
NGC 6633 HILT 140	−0.157	−0.080	0.016	−0.200	−0.052
NGC 6633 SAN 456	−0.116	−0.230	0.029	−0.200	−0.039

Table 4.16: each and weighted mean metallicities of the stars in cluster

Name	$[Fe/H]_{Fe4680}$	$[Fe/H]_{Fe4920}$	$[Fe/H]_{Fe5270}$	$[Fe/H]_{Mg}$	$[Fe/H]^{Weighted}_{Mean}$
IC 4665 42	0.203	0.712	−0.052	−0.336	0.126
IC 4665 54	0.216	0.601	−0.210	−0.540	0.086
IC 4665 74	0.183	0.631	−0.545	−0.947	0.113
IC 4665 MM 2	0.362	−0.188	−0.014	−0.997	0.249
IC 4665 MM 4	0.253	−0.065	−0.223	−1.117	0.108
IC 4665 V 119	−0.061	0.272	−0.147	−0.768	−0.095
GEN +3.46650024	0.503	−0.116	0.146	−0.230	0.398
GEN +3.46650026	0.152	−0.091	0.005	−0.935	0.108

Table 4.17: continued

Chapter 5

RESULTS OF THE OBSERVATION

5.1 Accuracy of Metallicity Determination

We estimated the error of our method with sixteen stars used for metallicity calibration. Figure 5.1 shows the correlation between the metallicities obtained by our method and those by high dispersion spectroscopy (standard). We confirmed that the error was ± 0.26 dex. In case of a cluster, since member stars were formed from the same molecular cloud, metallicity of one was obtained statistically and the error is reduced.

5.2 Metallicity of Open Clusters

Figure 5.2 - 5.5 show the metallicity of each stars in the clusters. Metallicity dispersions of the stars in each clusters are smaller than that expected with calibration stars ± 0.26 dex, except for NGC6866. Since NGC6866 5 shows extremely poorer metallicity than any others, this star does not seem to be a member of

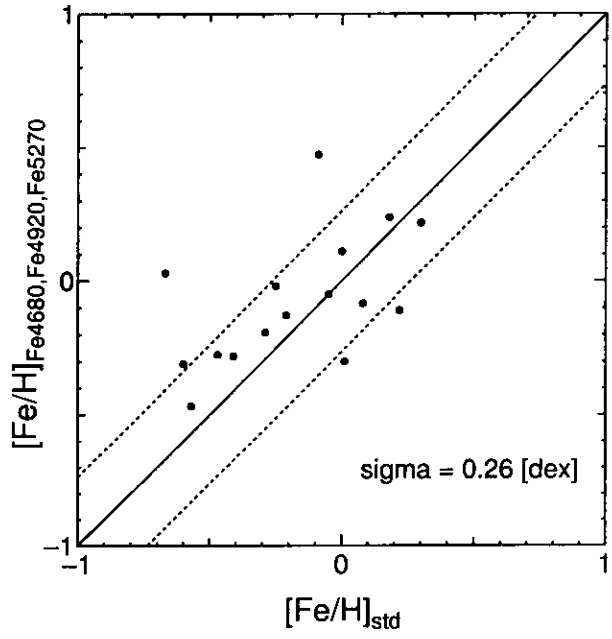

Figure 5.1: metallicity correlation between ours and standard

the cluster. Table 5.1 shows the metallicity of the clusters observed by us. The errors are estimated with processing statistically that for a star ± 0.26 dex and a number of stars in each clusters. Piatti et al.(1998) [16] has measured the metallicity of NGC6633. They have shown the metallicity of [Fe/H]$= -0.02$ dex. Our result [Fe/H]$= +0.07 \pm 0.09$ dex is consistent with this.

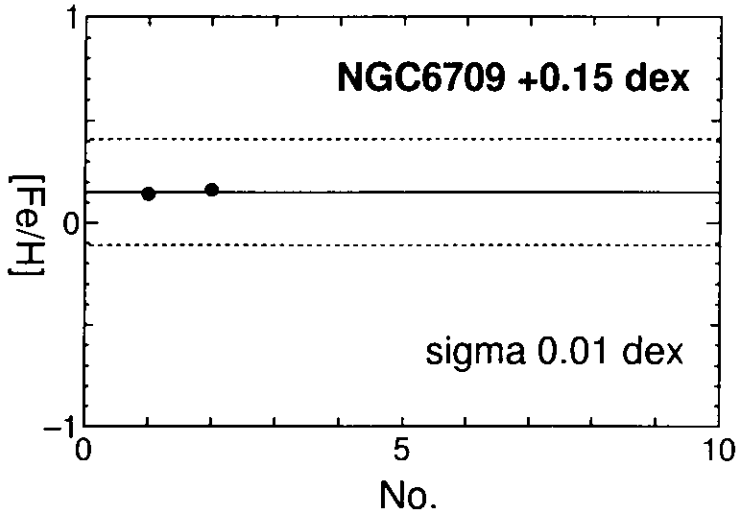

Figure 5.2: obtained metallicity of the stars in cluster

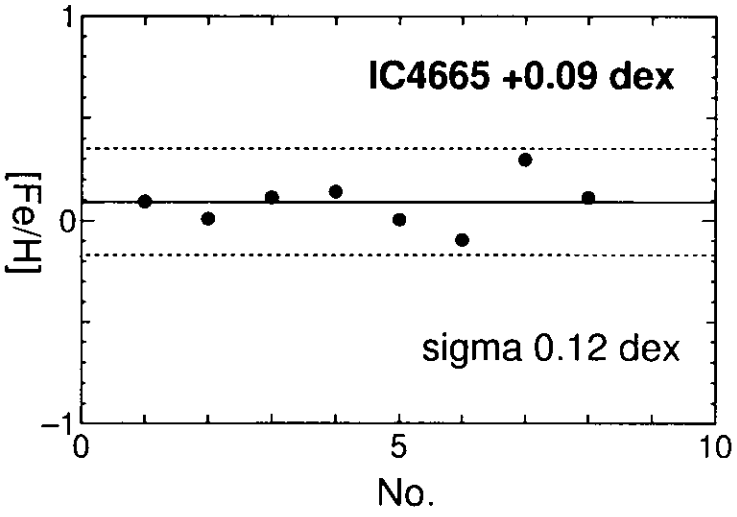

Figure 5.3: continued

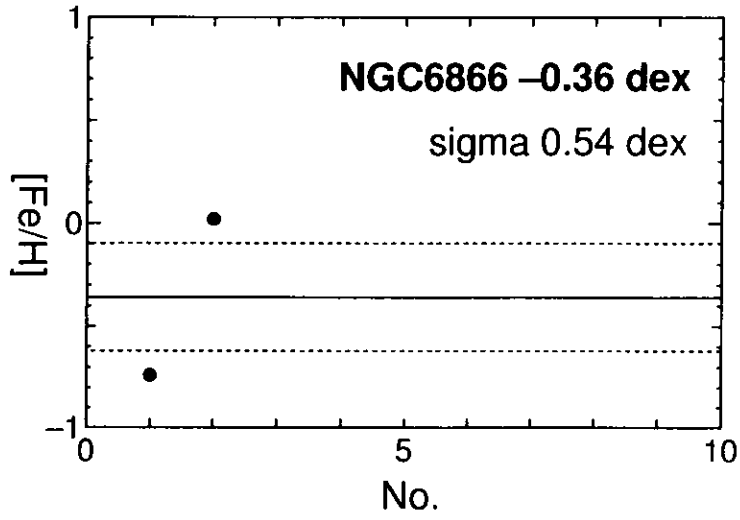

Figure 5.4: continued

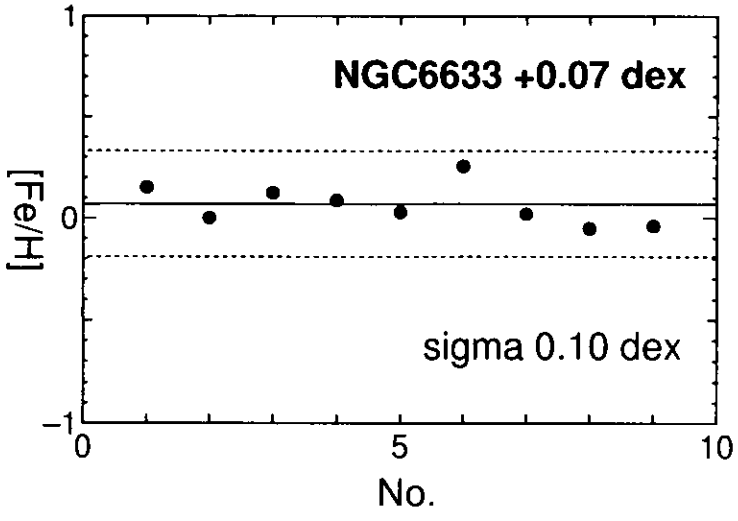

Figure 5.5: continued

Metallicity unknown		Metallicity known	
NGC6709(2)	$+0.15 \pm 0.01$ dex	NGC6633(9)	$+0.07 \pm 0.10$ dex
IC4665(8)	$+0.09 \pm 0.12$ dex		
NGC6866(2)	-0.36 ± 0.54 dex		

Table 5.1: metallicity of open clusters

5.3 Metallicity Distribution of Our Galaxy

Figure 5.6 shows the metallicity gradient of our Galaxy by Carraro et al.(1998) added to our data. The age of these clusters is 0.45 - 9.00 Gyr. Three our data in a group at above left attract considerable interest, although we can not indicate a new point of view on the dispersion of the metallicity gradient because of a few data. Figure 5.7 shows the metallicity distribution of the open clusters with age $<$ 1Gyr and $7.5 < R < 9.5$(R : galactocentricradius, $R_{\odot} = 8.5$). Five black thin marks is by Carraro et al.(1998). Four gray thick marks is by our observation. When we limit the age and position of the clusters, the dispersion of the metallicity seems to small.

Figure 5.8 and 5.9 shows metallicity distribution with open clusters near the Sun. These data was mainly obtained by photometric observations. Four clusters observed by us were added. Metallicities of the nearest two clusters, IC4665 and NGC6633, shown with black triangles in the figure, are comparable to those of nearby other clusters. We will accurately measure metallicities of other clusters by spectroscopic observations, and make metallicity distribution of the clusters clear.

We spent three nights in obtaining these data. If we observe for a few weeks, we will indicate a new point of view on the metallicity dispersion of Galaxy.

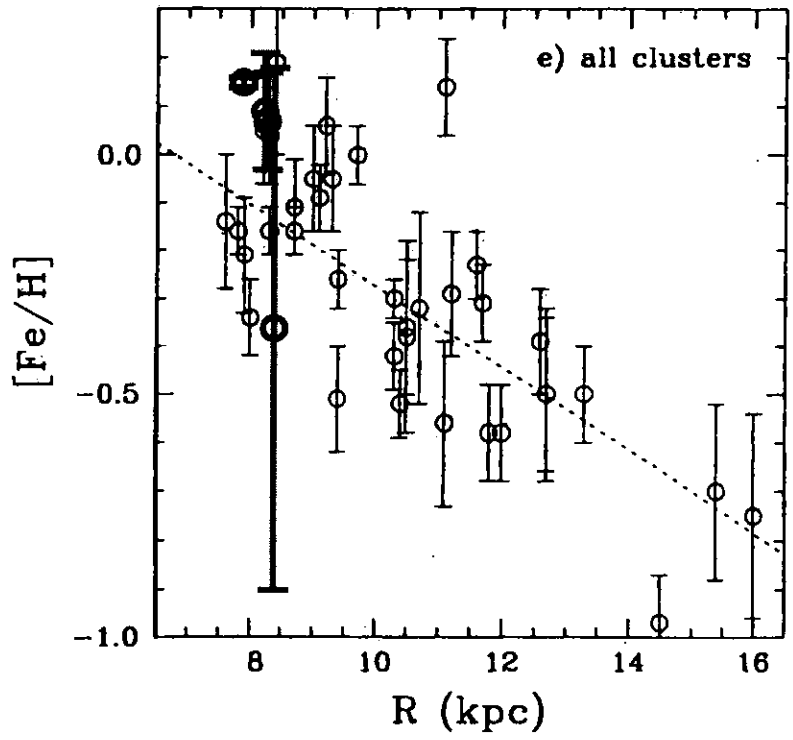

Figure 5.6: metallicity gradient of our Galaxy (Carraro et al. 1998); Four gray thick marks show our observation.

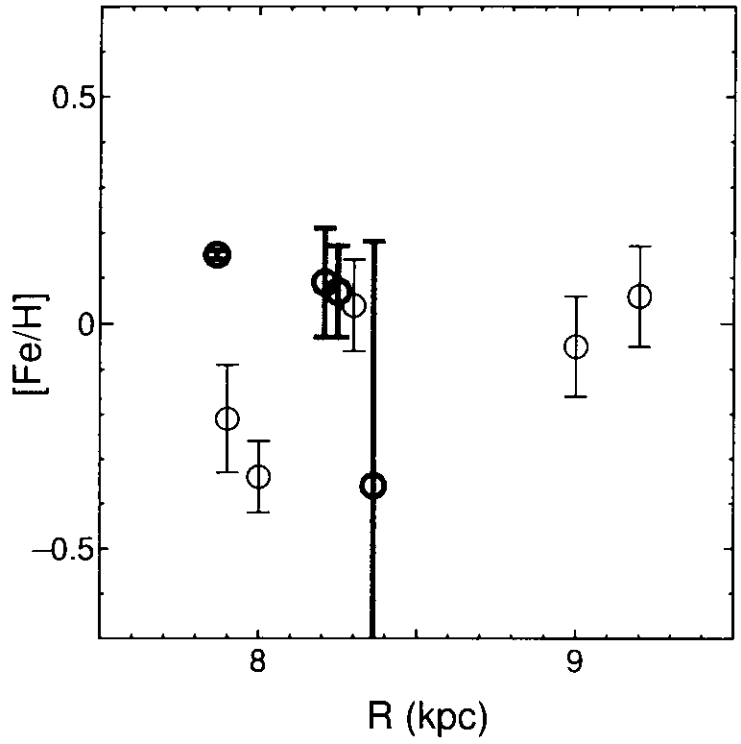

Figure 5.7: This figure shows the metallicity distribution of the open clusters with age < 1Gyr and 7.5 < R < 9.5($R_\odot = 8.5$). Thin five black marks is by Carraro et al.(1998). Thick four gray marks is by our observation.

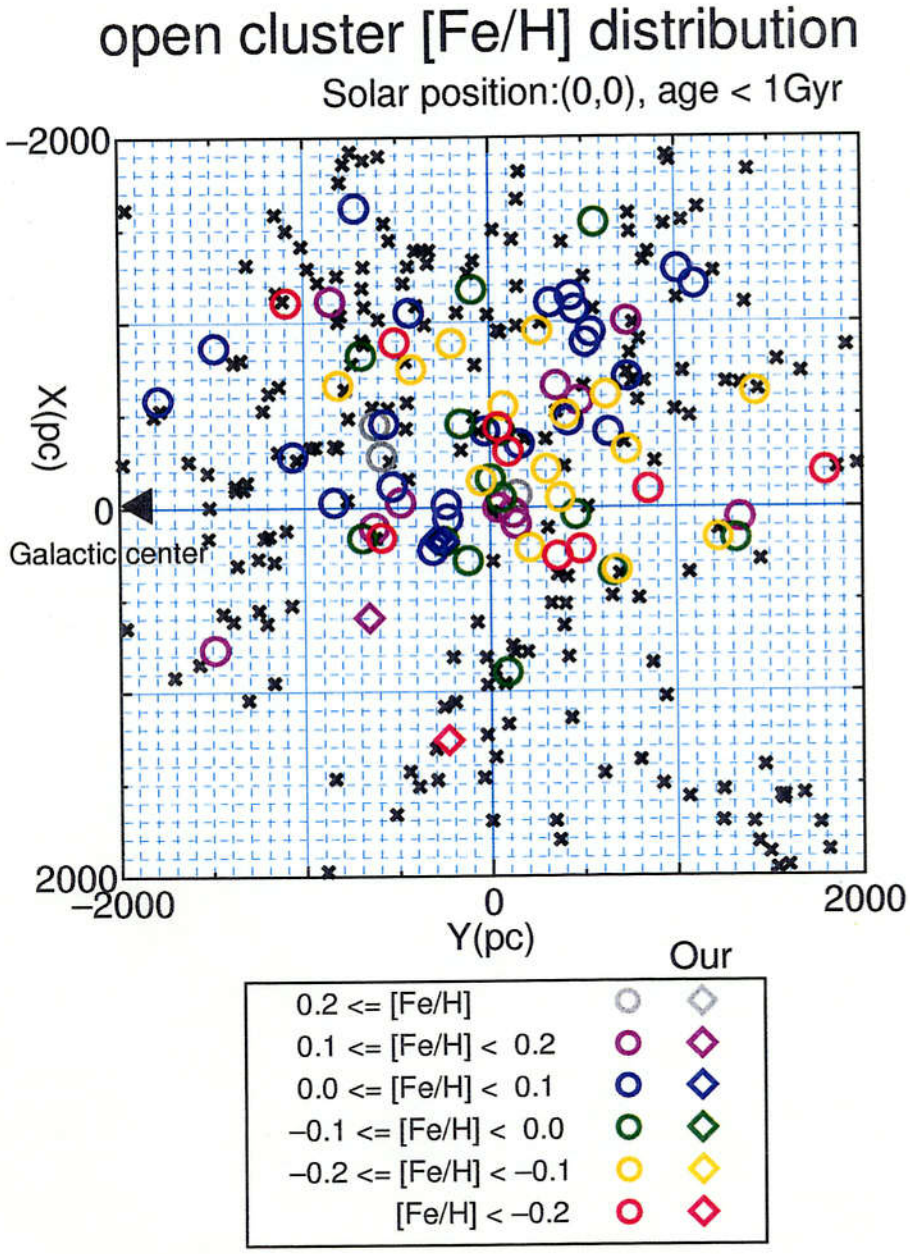

Figure 5.8: Metallicity distribution with open clusters near the Sun (face on). Four clusters observed by us are added ([Y,X]; NGC6709:[−657, 595], IC4665:[−294, 174], NGC6866:[−233, 1263], NGC6633:[−252, 183]). Crosses show the clusters unmeasured metallicity.

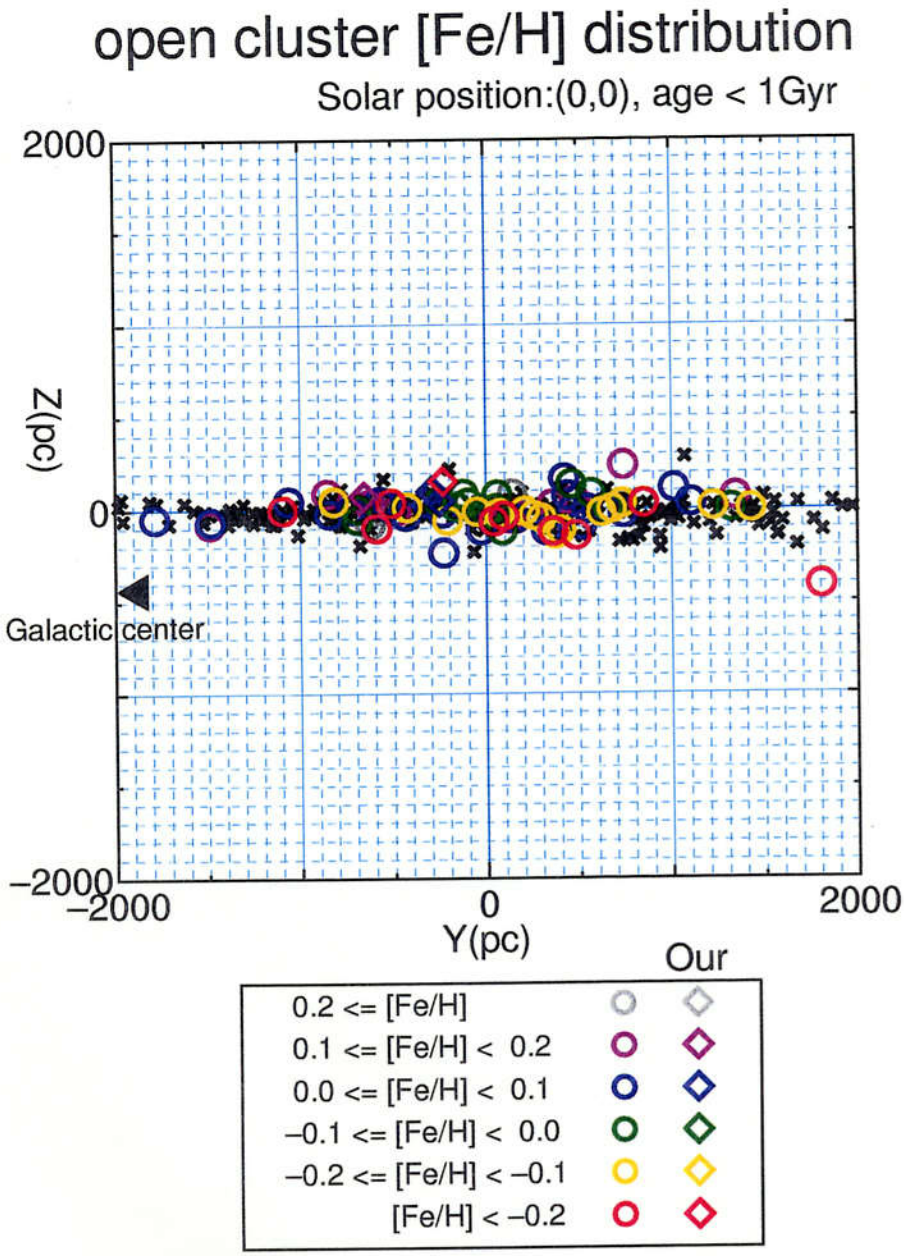

Figure 5.9: (edge on) ([Y,Z]; NGC6709:$[-657, 72]$, IC4665:$[-294, 100]$, NGC6866:$[-233, 153]$, NGC6633:$[-252, 44]$).

5.4 Difference of $[Fe/H]_{Mg}$ with $[Fe/H]_{Fe}$

In obtaining metallicities of clusters, we avoided the Mg index. Table 5.2 and 5.3 show metallicities of members derived from Mg index, $[Fe/H]_{Mg}$, and that from Fe indices, $[Fe/H]_{Fe}$. It is clear that $[Fe/H]_{Mg}$ are less than $[Fe/H]_{Fe}$. This results are consistent with other studies. Figure 5.14 indicates the correlation between the age of the clusters and the difference between $[Fe/H]_{Mg}$ and $[Fe/H]_{Fe}$, $[Fe/H]_{Mg-Fe}$, of Thogersen et al.(1993) results and ours. The ages of clusters we observed were derived from the Catalog of Open Cluster Data (Lynga 1987). Friel & Janes (1993) and Thogersen et al.(1993) suggest that the youngest clusters seem to rapidly decrease $[Fe/H]_{Mg-Fe}$. Our results are consistent with these suggestions.

Name	$[Fe/H]_{Mg}$	$[Fe/H]_{Fe}$	$[Fe/H]_{Mg-Fe}$
NGC 6709 HSS 208	−0.434	0.142	−0.576
NGC 6709 HSS 303	0.000	0.162	−0.162
IC 4665 42	0.092	0.060	0.032
IC 4665 54	−0.205	−0.068	−0.137
IC 4665 MM 2	−0.447	0.034	−0.481
IC 4665 MM 4	−0.447	−0.098	−0.349
GEN +3.46650024	0.312	0.194	0.118
GEN +3.46650026	−0.240	0.114	−0.354
NGC 6866 5	−0.600	−0.738	0.138
NGC 6866 26	−1.058	0.019	−1.077
NGC 6633 42	−1.264	0.152	−1.416
NGC 6633 121	0.094	0.001	0.093
NGC 6633 124	−1.124	0.125	−1.249
NGC 6633 HILT 14	−0.400	0.089	−0.489
NGC 6633 HILT 56	0.300	0.029	0.271
NGC 6633 HILT 67	−0.321	0.256	−0.577
NGC 6633 HILT 116	−0.100	0.020	−0.120
NGC 6633 HILT 140	−0.200	−0.052	−0.148
NGC 6633 SAN 456	−0.200	−0.039	−0.161

Table 5.2: each and total metallicities of the stars in cluster

Name	$[Fe/H]_{Mg}$	$[Fe/H]_{Fe}$	$[Fe/H]_{Mg-Fe}$
IC 4665 42	−0.336	0.126	−0.462
IC 4665 54	−0.540	0.086	−0.626
IC 4665 74	−0.947	0.113	−1.060
IC 4665 MM 2	−0.997	0.249	−1.246
IC 4665 MM 4	−1.117	0.108	−1.225
IC 4665 V 119	−0.768	−0.095	−0.673
GEN +3.46650024	−0.230	0.398	−0.628
GEN +3.46650026	−0.935	0.108	−1.043

Table 5.3: continued

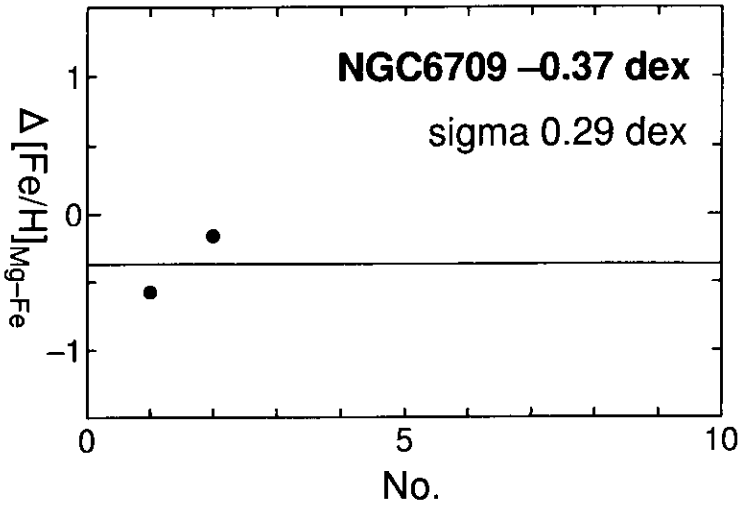

Figure 5.10: $[Fe/H]_{Mg-Fe}$ about the stars in open clusters

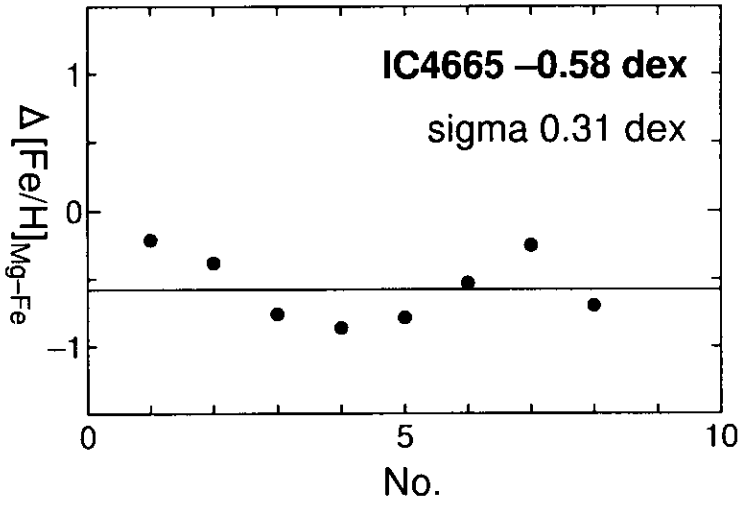

Figure 5.11: continued

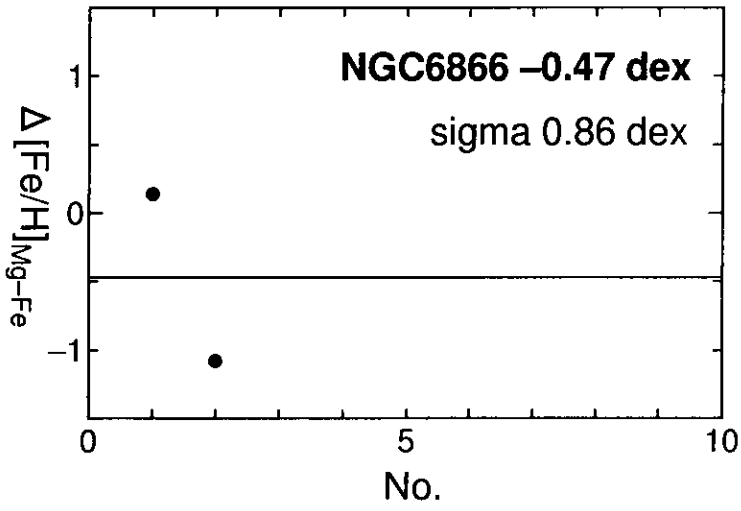

Figure 5.12: continued

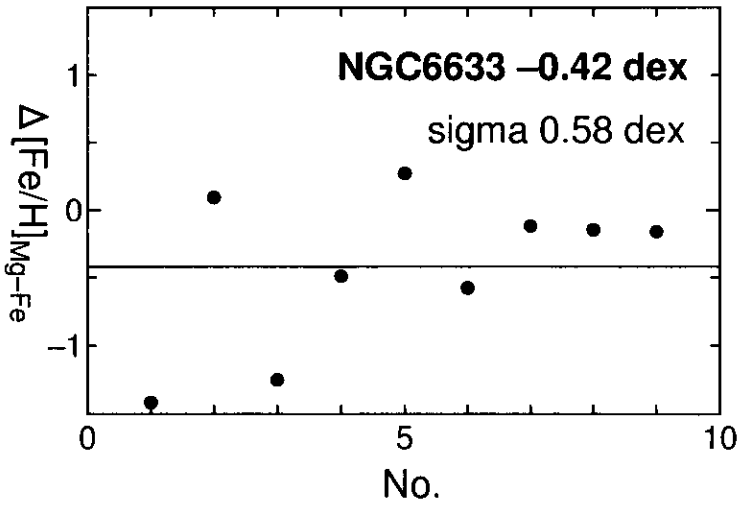

Figure 5.13: continued

Name	Age[Gyr]	$\overline{[Fe/H]_{Mg}}$	$\overline{[Fe/H]_{Fe}}$	$\overline{[Fe/H]_{Mg-Fe}}$
NGC6709	0.07	−0.217	+0.152	−0.369
IC4665	0.04	−0.486	+0.095	−0.581
NGC6866	0.23	−0.829	−0.360	−0.470
NGC6633	0.66	−0.357	+0.065	−0.422

Table 5.4:

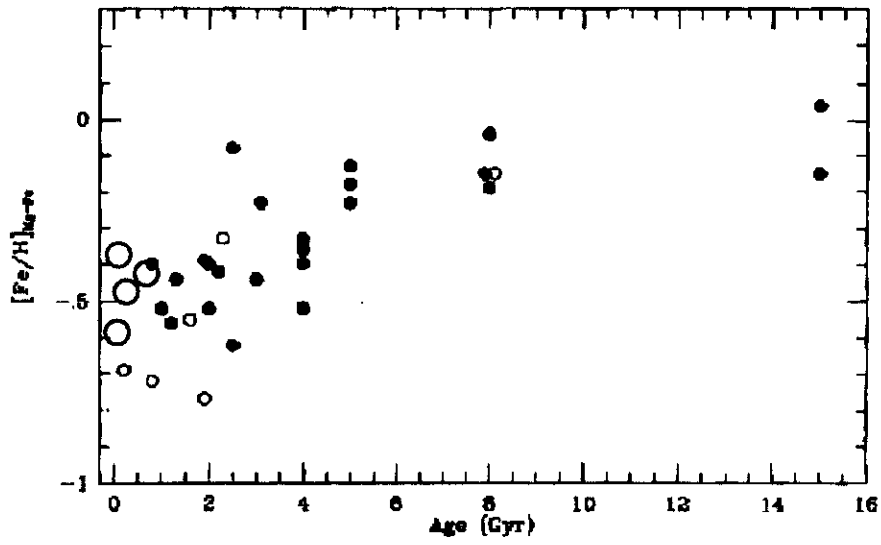

Figure 5.14: Age - $[Fe/H]_{Mg-Fe}$ relation of open clusters (Thogersen 1993). Four large gray circles show our data.

Chapter 6

ACKNOWLEDGEMENTS

This paper owes much to the thoughtful and helpful comments of many people. My special thanks are due to Prof. Hiroshi Karoji and Prof. Yoshikazu Nakada for valuable advice and helpful suggestions. I wish to thank Dr. Junichi Noumaru, who gave me fundamental knowledge of the Okayama Fiber Multi-Object Spectrograph. I also acknowledge helpful suggestion and assistance with Kiichi Okita, Yuji Norimoto, Yasushi Yadoumaru, Tomohiko Ozawa, Nobunari Itoh, Akito Tajitsu, Ken-ichi Tarusawa, Takao Soyano on several points of in the paper. I also thank Shigeomi Yoshida, Takeo Minezaki, Tsutomu Aoki, Hideo Maehara, Kenshi Yanagisawa, Shin-ichiro Okumura, Michitoshi Yoshida, Masanori Iye, Takuya Yamashita, Nobunari Kashikawa, Satoshi Miyazaki, Hirokazu Kataza, Yukiyasu Kobayashi, Masatoshi Taga, Yoichi Itoh, Noboru Ebizuka, Masashi Ootsubo, Taku Takeuchi, Yoshio Mikami, Kyoko Tanaka, Tetsuo Nishino, Syuji Sato, Kenihci Wakamatsu, Katsuo Ogura, Hiroshi Ohtani, Kazuhiro Sekiguchi, Shin-ichi Ichikawa, Naruhisa Takato, Hideki Takami, Maki Sekiguhci, Toshihisa Hibarino, Takahiro Fujii, Jin Koda, Yoshifusa Ita, and Quentin A. Parker for valuable comments, criticisms, and assistance. I am grateful to Fumie Oouchi, Mitsuyoshi Kubota, Tsuyoshi Yamada, Takahiro Nakamura, and Wakana Saito for encour-

aging and supporting this study.

Bibliography

[1] Giovanni Carraro, Yuen Keong Ng, and Laura Portinari. On the galactic disk age-metallicity relation. *Monthly Notices of The Royal Astronomical Society*, 296(4):1045, June 1998.

[2] Juan J. Claria, Andréss E. Piatti, and Wayne Osborn. DDO metal abundances of high-luminosity late-type stars in galactic open clusters. *Publications of the Astronomical Society of the Pacific*, 108:672, August 1996.

[3] Philip Massey et al. Spectrophotometric standards. *The Astrophysical Journal*, 328:315, May 1988.

[4] E. D. Friel. The old open clusters of the milky way. *Annual Review of Astronomy and Astrophysics*, 33:381, 1995.

[5] E. D. Friel and K. A. Janes. Metallicities and radial velocities of old open clusters. *Astronomy and Astrophysics*, 267:75, 1993.

[6] Eileen D. Friel. A spectroscopic survey of high-latitude fields and comparison to galaxy models. *The Astrophysical Journal*, 93(6):1388, June 1987.

[7] Lynga G. Catalogue of open cluster data 5th edition. February 1987. computer readable catalogue of open cluster data.

[8] G. H. Jacoby, D. A. Hunter, and C. A. Christian. A library of stellar spectra. *The Astrophysical Journal Supplement Series*, 56:257, 1984.

[9] K. A. Janes. 1988. In *Calibration of Stellar Ages*, ed. AGD Philip, p.59. Schenectady: Davis.

[10] K. A. Janes. Evidence for an abundance gradient in the galactic disk. *The Astrophysical Journal Supplement Series*, 39:135, February 1979.

[11] Arlo U. Landolt. UBVRI photometric standard stars in the magnitude range $11.5 < V < 16.0$ around the cerestial equatror. *The Astronomical Journal*, 104(1):340, July 1992.

[12] Junichi Noumaru, Hiroshi Karoji, Kiichi Okita, and Yuji Norimoto. Development of fibertransit-fiber linked multi-object spectroscopy system. *Publications of the National Astronomical Observatory of Japan*, 3(2):107, 1993.

[13] Ian R. Parry and Peter M. Gray. An automated multiobject fibre optic coupler for the anglo-australian telescope. In *Instrumentation Astronomy VI*, volume 627, page 118. SPIE, 1986.

[14] Ian R. Parry and Ian J. Lewis. automated fibre optic instrumentation for the william herschel telescope. In *Instrumentation Astronomy VII*, volume 1235, page 681. SPIE, 1990.

[15] Andress E. Piatti, Juan J. Claria, and Mario G. Abadi. Chemical evolution of the galactic disk: evidence for a gradient perpendicular to the galactic plane. *The Astronomical Journal*, 110(6):2813, December 1995.

[16] Andréss E. Piatti, Juan J. Clariá, and Eduardo Bica. Composite M_v versus $(V-I)_0$ diagram for template open clusters. *The Astrophysical Journal Supplement Series*, 116:265, June 1998.

[17] Stephen J. Smartt and William Robert J. Rolleston. The galactic oxygen abundance gradient. *The Astrophysical Journal*, 481(1), May 1997.

[18] E. N. Thogersen, E. D. Friel, and B. V. Fallon. Metallicities and velocities of old open clusters. *Publications of the Astronomical Society of the Pacific*, 105:1253, November 1993.